DEVELOPMENT OF COMBINED RAMAN SPECTROSCOPY - OPTICAL COHERENCE TOMOGRAPHY FOR THE DETECTION OF SKIN CANCER

By

Chetan Appasaheb Patil

Dissertation

Submitted to the Faculty of the

Graduate School of Vanderbilt University

in partial fulfillment of the requirements

for the degree of

DOCTOR OF PHILOSOPHY

in

Biomedical Engineering

December, 2009

Nashville, Tennessee

Approved:

Professor Anita Mahadevan-Jansen

Professor E. Duco Jansen

Professor Darrel L. Ellis

Professor Robert L. Galloway Jr.

Professor Ton G. van Leeuwen (University of Amsterdam, NL)

Professor David L. Dickensheets (Montana State University)

To Jiya

ACKNOWLEDGEMENTS

This work would not have been possible without the assistance, guidance, and expertise of many people. First and foremost, I would like to thank my dissertation advisor, Dr. Anita Mahadevan-Jansen, for her patience, guidance, personal support, ability to obtain funding, and expertise in Raman spectroscopy. I'd like to thank my committee members, Dr. E. Duco Jansen, Dr. Darrel Ellis, Dr. Ton van Leeuwen, Dr. David Dickensheets, and Dr. Bob Galloway for their expertise and time. I'd particularly like to thank Dr. Jansen for his helpful suggestions and insight during lab meetings and patience with me over the years, Dr. van Leeuwen for his guidance in OCT and Dr. Ellis for his clinical expertise, and time and effort spent reading pathology.

Along the way, I received significant technical contributions from many people, whose names belong on this dissertation as much as mine. Neinke Bosschaart's assistance was very helpful in the preparation of the first manuscript. The assistance of Dr. Jeroen Kalkman and Dr. Dirk Faber was instrumental in the development of the SD-OCT system. I owe a debt of gratitude to Jeroen in particular for his assistance in developing the SD-OCT software and insightful discussions on sensitivity in OCT. I'd like to thank Dr. John Penn, whose collaboration was essential to the completion of the common detector RS-SDOCT manuscript, and Evelyn Okedije's efforts performing retinal histology. Translating the work from the lab to the clinic would not have been a reality if it weren't for the efforts of Harish Krishnamoorthi and the skill and craftsmanship of John Fellenstein and Bob Patchin in the physics machine shop. I am particularly appreciative to Mohs surgeons Dr. Thomas Stasko and Dr. Anna Clayton, Mohs fellow Dr. Allison Hanlon, Cindy Craft for allowing me to perform the clinical studies despite the inconvenience it surely caused them. Making measurements with the clinical RS-OCT system is certainly not a one person job, and wouldn't have been possible without help from Dr. Xiaohong Bi and Dr. Mark Mackanos. I'd also like to specifically thank those in the Raman Spectroscopy group, including Dr. Chad Lieber, Matthijs Grimbergen, Dr. Elizabeth Kanter, Dr. Matthew Keller, and Elizabeth Vargis for providing me with many insightful discussions over the years.

I was lucky enough to collaborate and share office space with some exceptionally good natured people here at Vanderbilt. In particular, I'd like to thank Dr. Jeffry Nyman and Chris Arrasmith for allowing me to expand my scientific horizons beyond the work of my dissertation. I can't say enough about the great friends I've made in the lab along the way, particularly Dr. Jonathon Wells and Dr. Jerry Wilmink, who welcomed me to Vanderbilt like only "Jon and Jerry" could. My office and labmates Jonathon Cayce, Jonathon Malphrus, Austin Duke, Dean Paras, Bart Masters, and Alex Makowski have all been great sources of humor in the last few trying months. Of course, I would be remiss if I left out my roommates from my bachelor days, Prashanth Dumpuri and Logan Clements.

Finally I'd like to thank the love of my life, my wonderful wife, Meenal. Your constant love and unwavering faith in me are the basis of this work. I'd like to thank my far smarter brother Rohan, who has easily learned more about life these last few years than I ever could have in graduate school. Your perseverance has served as a constant source of motivation for me this past year. Most of all, however, I'd like to thank my father and mother for instilling in me the value education. This work is as much my family's accomplishment as it is mine. I love you all.

TABLE OF CONTENTS

LIST OF FIGURES

Page

LIST OF TABLES

Page

CHAPTER I

Introduction

Some of the earliest optical instruments -- simple tubes with a single lens in one end, appropriately known as “flea tubes” -- were applied to viewing magnified images of biological specimens such as insects and fleas. As early as the late 17th century, Anton van Leeuwenhoek, the Dutch scientist widely considered the father of microscopy, was applying his carefully constructed microscope to examine the human body, and discovering previously invisible details of micro-anatomy such as erythrocytes in blood[1]. Over the last three centuries, optical microscopy has played a critical role in the development of our current understanding of cellular physiology and molecular biology. Currently, the modern field of pathology relies almost exclusively on microscopic evaluation of stained tissue samples as the gold standard for crucial medical diagnoses of diseases such as cancer. However, our current understanding of the nature of cancer and optimal treatment strategies has made it clear that screening and early detection, accurate diagnosis, and appropriate staging are all critical in directing treatment to obtain the best outcomes. In the case of epithelial cancers, particularly those of the skin, screening and early detection can be particularly challenging. Physicians are forced to examine a large area containing a number of non-malignant lesions and isolate those that are cancerous for biopsy and pathology. This paradigm can be subjective, painful for the patient, time-consuming, and costly. Fortunately, techniques for optical analysis have developed significantly since the days of van Leeuwenhoek. An improved understanding of the nature of light and it’s interaction with tissues, the development of methods such as spectroscopy and interferometry, and technological developments such as fiber optics and the charge-coupled-device (CCD), have facilitated the development of optical techniques far beyond simple microscopic evaluation. Identification of the sub-optimal nature of biopsy and histology and an appreciation of enhanced capabilities of novel optical methods has spurred the challenge of performing non-invasive direction of treatment with modern optical methods – an approach broadly dubbed “optical biopsy”. In the last 20 years, the enthusiastic application of a number of optical imaging and spectroscopy

techniques has identified the strong potential – and practical limitations – of these approaches to performing true optical biopsy. To date, no single method has demonstrated the ability to perform screening, diagnosis, and staging of cancers sufficiently well that cancer therapies can be directed without the need for physical biopsy. The current task we are now faced with is how to best apply these techniques to the challenge of performing true optical biopsy.

Motivation

Prior to the initiation of this dissertation, our group here at Vanderbilt had established itself as one of the leading groups in the field of *in vivo* Raman spectroscopy (RS), a technique that is capable of characterizing the specific biochemical composition of tissues based on the in-elastic scattering of light[2]. The ability of fiber-optic probe based RS to detect cervical dysplasia in the demanding clinical environment had been demonstrated with excellent results[3]. In the context of skin cancer diagnosis, *in vitro* and *in vivo* studies using confocal RS had demonstrated the potential for multi-class diagnosis of skin lesions with excellent overall classification accuracies[4, 5]. This body of work identified two issues with RS in the context of performing optical biopsy of skin cancers.

The most direct issue is the question of whether a confocal collection geometry is necessary for accurate classification of skin cancers with RS. The motivation behind using a confocal approach was to isolate the spectral features of cancerous cells from those originating in the surrounding epidermis and dermis, thus improving the diagnostic accuracy of the technique. However, a compelling finding from the *in vitro* and *in vivo* studies was that regardless of whether the instrument specifically focused on cancerous cells or the non-involved dermis, confocal RS was able to classify cancerous tissues with overall accuracy > 90%. Results from the *in vivo* study indicated that confocal RS could identify the presence of cancers when the collection volume was as far as 900 μm away from the tumor margins. These findings are supported by observations from other groups, which have reported that peri-tumoral changes in the collagen and dermis surrounding a skin cancers can be detected by Raman spectroscopy[6, 7]. The natural question that arises is, "Does accurate spectral classification of skin cancers with RS require a confocal collection geometry?" The relevance of this question is related to the primary clinical limitation of confocal RS – the collection geometry necessitates integration times on the

order of 30 sec in comparison to fiber optic probe acquisition times of only 3 seconds. Understanding whether or not a confocal collection geometry is necessary would thus significantly impact the development of future Raman studies and instrumentation.

The primary limitation of both fiber optic probe and confocal RS, however, is the fact that the inherently weak nature of in-elastic scattering limits *in vivo* RS to a few point-based measurements in a clinically relevant time-frame and precludes the generation of Raman maps that could identify the spatial aspects of pathological tissues. This can be problematic for two reasons; 1.) Because lesions are identified based on their visual appearance alone, site selection for RS can be just as susceptible to sampling error as biopsy, and 2.) Understanding the morphology and spatial extent of cancers is critical to pursuing the appropriate course of treatment. Based on these criteria, a complimentary optical technique to RS was sought out in order to create a dual-modal device capable of rapid non-invasive characterization of the morphological features of cancer.

Optical coherence tomography (OCT) is a novel optical imaging modality capable of generating cross-sectional images in highly scattering tissues with micron-scale resolution that well fits this bill[8]. In contrast to other non-invasive optical imaging techniques such as confocal reflectance microscopy, axial resolution in OCT is defined by spectral bandwidth of the laser source as opposed to the numerical aperture of the focusing optics. This permits OCT to rapidly collect high resolution images over a large transverse area, which is advantageous for identifying tumor margins and gross morphology. In addition, OCT had been demonstrated capable of visualizing the microstructural features of a wide range of skin cancers[9-11]. The limitation of OCT, however, is that it simply detects backscattered light, and therefore has no direct ability to ascertain the molecular or biochemical composition of tissues, which is critical for high specificity detection of disease. In this context, the combination of OCT with RS can also provide significant benefit to the application of OCT for the diagnosis of cancers. The two techniques are ideally complimentary and well suited for integration into a common instrument designed for screening, diagnosis, and staging of cancers.

Specific Aims

The goal of this dissertation is to develop the method of combined Raman spectroscopy – Optical Coherence Tomography (RS-OCT) and construct a clinical system for the in vivo measurement of questionable skin lesions. The significance of a combined RS-OCT instrument would lie in its ability to address each of the critical charges required of optical biopsy. The ability of OCT to perform high speed imaging would allow high sensitivity, rapid, screening of the large areas for the morphological features of disease. Raman spectra could then be acquired from the lesion sites, and the biochemical composition of the lesion could be used to perform accurate diagnosis. Closer examination of the lesion morphology with OCT could then provide an estimation of lesion margins and depth of invasion, which is critical for appropriate staging. The successful realization of such a device would present a significant step towards the goal of optical biopsy.

Specific Aim #1

Aim #1 of this dissertation is to perform a pilot study assessing the ability of fiber optic probe based RS to classify skin cancers. A pilot study was conducted in which spectra from 34 lesions from cancerous and non-cancerous lesions, along with matched spectra from similar normal skin, were measured with fiber optic probe based RS. Difference (lesion – matched normal) spectra were calculated to account for the inherent variation in skin. Difference spectra were classified using Sparse Multinomial Logistic Regression (SMLR). Spectra were classified with an overall accuracy of 85%, with a sensitivity of 78% and a specificity of 94%. These results suggest the potential utility of non-confocal RS for accurate classification of skin cancers, however a more extensive research is necessary.

Specific Aim #2

Aim #2 of this dissertation is to develop a benchtop combined RS-OCT system utilizing separate OCT and Raman system backbones. A dual-modal device capable of sequential acquisition of Raman Spectroscopy (RS) and optical coherence tomography (OCT) along a common optical axis was constructed. The system performance was characterized, and capability of the device to identify structurally

ambiguous features within an OCT image with RS in a scattering phantom, guide acquisition of RS from a localized malignancy in ex vivo breast tissue, and perform in vivo tissue analysis of a scab. The device enhances application of both RS and OCT by precisely guiding RS acquisition with OCT images while also compensating for the lack of molecular specificity in OCT with the biochemical specificity of RS. The results indicate the potential capability of RS-OCT for *in-vivo* morphological and biochemical analysis of the skin.

Specific Aim #3

Aim #3 of this dissertation is to develop a benchtop combined RS-OCT using a common detection arm. Previous implementations of RS-OCT have employed separate system backbones for OCT and RS. Here, we present the design and application of a common detector combined RS-OCT instrument for evaluating the morphological and biochemical differences in tissue. The instrument is applied to evaluating a rat model for oxygen induced retinopathy. Rat pups that have undergone a variable oxygen treatment are compared to rats raised in room air. Images and spectra collected at an age of 26 days postnatal demonstrate differences in the thickness of the inner and outer nuclear layers, with OCT as well differences in the Raman spectral bands attributed to DNA and RNA nucleotides, amino acids, and proteins. The results from this study demonstrate the first implementation of common detector RS-OCT, however they suggest that the independent detection of the RS and OCT signals is the optimal approach for *in vivo* analysis of skin lesions.

Specific Aim #4

Aim #4 of this dissertation is to develop a clinical system for combined RS-OCT for analysis of the morphological and biochemical features of skin cancer. The portable instrument utilizes independent RS and OCT system backbones, and is integrated in a common clinical probe. The potential of the probe for cancer detection of the morphological and biochemical features of malignant and non-malignant lesions is demonstrated. The results from this aim indicate the potential of RS-OCT for evaluating skin cancers, and warrant more extensive work.

Background

Skin Microstructure, Skin Cancer, and Skin Cancer Management

Normal Skin Microstructure

Normal human skin is composed of two main layers, the epidermis and the dermis, which lie above a layer of subcutaneous fat that separates the skin from the underlying fascia and muscle (figure 1).

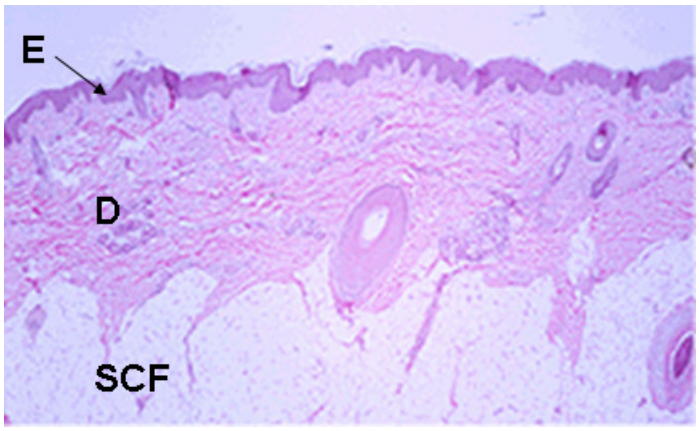

Fig. 1: Normal Human Skin Histology. The main layers of the skin can be clearly visualized, from top to bottom, as the epidermis (E), the dermis (D), and the subcutaneous fat (SCF)[12].

The topmost layer of skin is the epidermis, which varies in thickness from 50 μm in the eyelids to 1.5 mm in the palms and soles of the feet [13]. The epidermis is a stratified squamous epithelium whose principal cell type is the keratinocyte. Keratinocytes are produced by cell division in the bottommost layer of the epidermis, known as the stratum basale (basal layer), and migrate upward as they undergo keratinization. The stratum basale is also the layer of the epidermis in which the pigment producing melanocytes reside. As keratinocytes differentiate, they progressively accumulate keratin (a family of intracellular skeletal protein filaments), flatten, lose their nuclei, and finally die and are reduced to strains of keratin filaments. As the cells migrate, they pass through the following layers of the epidermis (from bottom to top) [14]: the stratum spinosum, which is the predominant keratinocyte layer, the stratum granulosum, which consists of flattened, anuclear, cells with large amounts of keratin, and the stratum corneum, which is primarily the remaining keratin filaments left over after the keratinocyte has died (fig. 2).

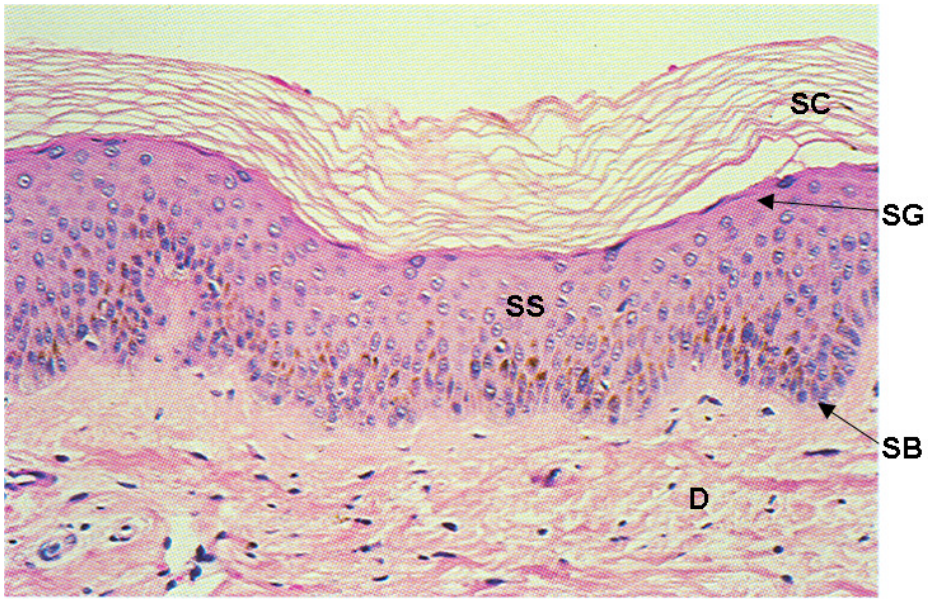

Fig. 2: Histology of Normal Epidermis and Dermis. Here the layers of the epidermis can be clearly seen. The stratum corneum (SC), the stratum granulosum (SG), the stratum spinosum (SS), the stratum basale (SB). Beneath the epidermis is the dermis (D). [15]

The dermoepidermal interface is formed by a thin basement membrane that consists of the lamina lucida and the lamina densa. The lamina lucida is in contact with the epidermis, while the lamina densa is in contact with the dermis. The dermis is a dense layer primarily composed of collagen along with lesser amounts of elastin. These structures give the dermis great elasticity and strength. The dermis also contains sensory cells and vascular networks.

Skin Cancer

Skin cancer is the most commonly occurring of all cancers, accounting for more than a million incidences (about half of the total number of cancer incidences) in the United States annually [16]. Fortunately, the two most commonly occurring skin cancers (basal cell carcinoma and squamous cell carcinoma), have survival rates of better than 98%, with mortalities coming mostly from immuno-compromised patients or elderly patients with advanced disease. The American Cancer Society estimates 800,000 to 900,000 new cases of basal cell carcinoma in 2006 along with 200,000 to 300,000 new cases of squamous cell carcinoma [16]. The most dangerous of skin cancers is malignant

melanoma, which accounts for only 4% (approx. 62,000 cases) of all skin cancer occurances but nearly 80% of skin cancer related deaths [17].

Although basal cell carcinomas (BCC's) are the most commonly occurring types of skin cancers, they are also one of the least dangerous due to their slow growth rate and the extreme rarity with which metastases occur. BCC's arise from transformed epidermal stem cells in the basal layer, such that upon pathological analysis, the tumor cells have a characteristically columnar appearance (fig. 3).

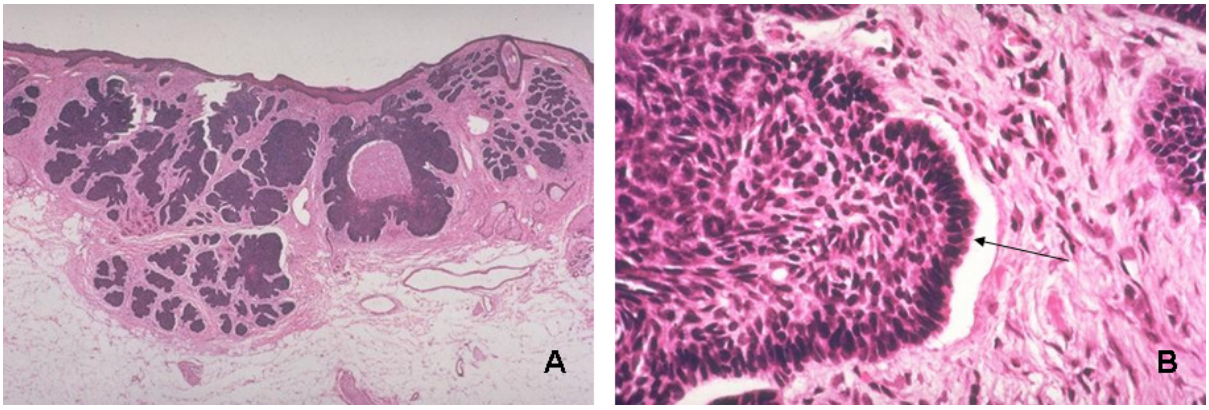

Fig. 3: Histology of basal cell carcinoma. In the low magnification image (A) you can clearly see the nests of cancerous cells. High magnification (B) shows peripheral pallisading (arrow) [15].

BCC's tend to form nests of tumor cells whose peripheral borders appear as an orderly line of basal cells (termed "peripheral pallisading") and whose centers possess similar cell types with low amounts of cytoplasm. Clinically, BCC's present in 4 variants: superficial, nodular, pigmented, and sclerosing (fig. B.4) [18]. Superficial BCC's occur most commonly on the trunk and extremeties and present as red to pink scaling plaques, with occasional shallow erosions. Nodular BCC's occur on the face and ears, and begin as small, firm, dome-shaped translucent papules. Pigmented BCC's are often confused with melanomas. Sclerosing BCC's occur most often on the face and appear as an indurated, white plaque with a atrophic surface. Clinical recognition of BCC's can be difficult because of their resemblance to other clinical entries such as sebaceous hyperplasia and molluscum contagiosum (similar to nodular BCC) or eczema and psoriasis (similar to superficial BCC). Risk factors for the development of BCC include fair skin and Celtic ancestry, cumulative over-exposure to UV light, ionizing radiation, or arsenic, and patients who are on immunosuppressive medications [18].

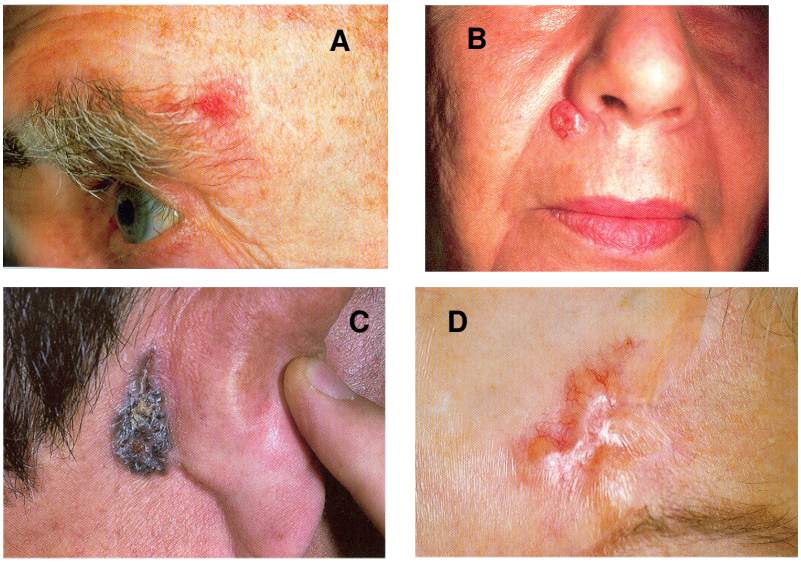

Fig. 4 Common clinical presentations of basal cell carcinoma: BCC presenting as a pink patch with pearly borders (A), Nodular BCC on the nose (B), Superficial Pigmented BCC behind the ear. Note the similarity to melanoma (C), and recurrent sclerosing BCC (D) [18].

.

Squamous cell carcinoma (SCC) is the second most commonly occurring type of skin cancer, however it is more aggressive in comparison to BCC. The metastatic rate of SCC is 2% to 6% in sun-damaged skin, 10% in SCC's involving the lip, and 30% in SCC's involving scars [18]. SCC's originate from transformed cells in the stratum spinosum, and have the potential to develop downwards and invade into underlying structures. SCC's appear pathologically different than BCC's. The tumor nests are bordered by polygonal cells with larger degrees of cytoplasm than BCC's. SCC tumor cells also differentiate towards the center of the nests such that the nest centers often have sections of keratinized epidermal cells which appear as "keratinized pearls" (fig. 5) [19].

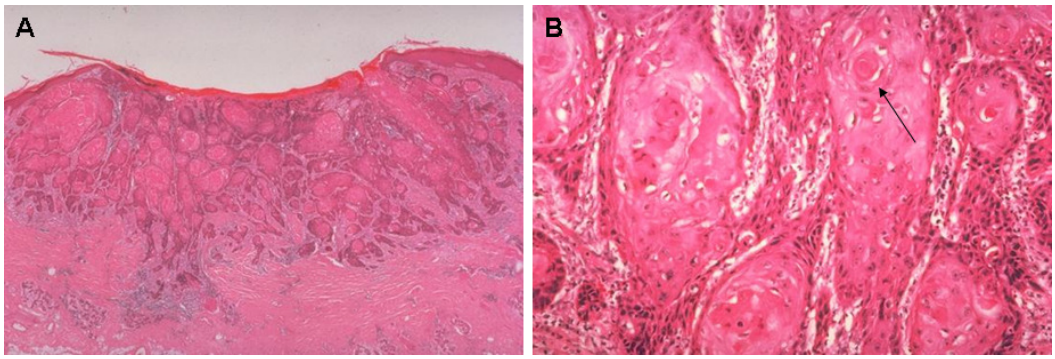

Fig. 5: Histology of squamous cell carcinoma. A low magnification view shows the keratinized tumor cell nests(A), which are more clear in the high magnification view (B). Arrow points to keratinized pearl [15].

The degree to which a SCC has differentiated is the basis for their grading (called Broder's classification), with poorly differentiated SCC's presenting a higher risk for invasion and metastases. Clinically, SCC's present with the most prevalence on the face, ears, scalp, and dorsum of the hands. SCC's normally begin as small erythematous, scaly, crusted patches (fig. 6).

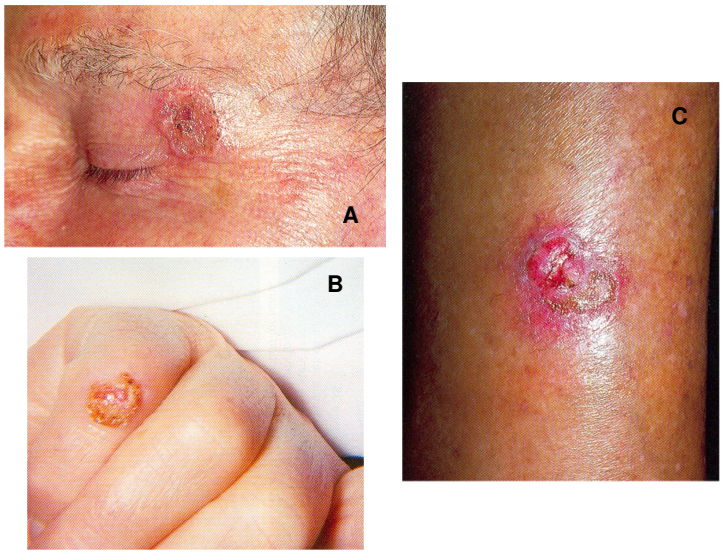

Fig. 6: Common clinical presentations of squamous cell carcinoma. In addition to the head, as shown by the SCC above the eye (A), SCC's also present on places such as the hand (B) and leg (C) [18].

Clinical differentiation of SCC's from other skin lesions also normally requires histo-pathological analysis as they can often be confused with non-cancerous lesions. Risk factors for SCC include cumulative exposure to both UV-A and UV-B light, Celtic ancestry, poor tanning ability, severe sunburns during childhood, exposure to ionizing radiation, thermal burns and scars, and the use of artificial tanning booths [18].

Malignant melanomas are the rarest, but most deadly form of the common skin cancer. Melanomas arise from transformed melanocytes in the basal layer of the epidermis. The cancerous cells then spread upwards into the epidermis as well as downwards into the dermis and underlying tissues (fig. 7).

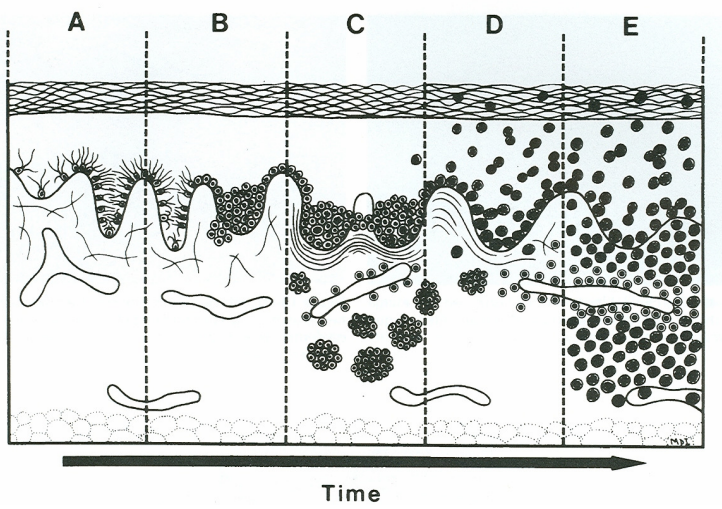

Fig. 7: Tumor Progression to Melanoma. Normal melanocytes in the basal layer (A) undergo transformation (B), and progress to form tumor nests (C). This progression results in the emergence of clone malignant cells which proliferate in close proximity to the epidermal layer (D) in the radial growth phase. Eventually, these cells gain the ability to invade the tissue (E) in the vertical growth phase [15].

Malignant melanomas are graded on Clark's scale, which examines the anatomic level of tumor cell invasion ranging from level I (tumor cells all above the basement membrane) to level V (tumor cells have broken the basement membrane, invaded the through the full depth of the dermis and into the subcutaneous layers) [18]. Clinically, melanomas appear as dark pigmented lesions with 4 subtypes: Lentigo maligna, superficial spreading melanoma, acral lentiginous melanoma, and nodular melanoma (fig. 8).

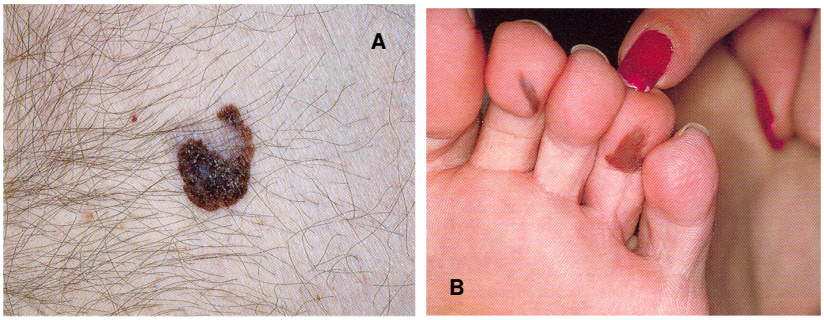

Fig. 8: Clinical presentations of melanoma. Two clinical presentations of malignant melanoma include nodular (A) and acral lentiginous (B) melanoma [18].

The first 3 initially spread horizontally before vertical invasion, and therefore have an excellent prognosis if diagnosed early enough. Nodular melanoma, however, almost immediately begins a vertical growth phase and is therefore associated with a much worse prognosis. Risk factors for melanoma include intense, intermittent, exposure to UV

radiation at an early age, Celtic ancestry, and individuals with genetic predisposition. Cumulative UV exposure and melanoma risk are not linearly correlated, thus partially explaining the increased occurrence of melanomas on the back of men and the legs of women when compared to BCC or SCC [18].

Skin Cancer Management

Currently, the gold standard for skin cancer diagnosis is histopathological evaluation of tissue biopsies. Depending on the nature of the skin lesion, different types of biopsies are performed. For raised skin lesions not believed to be melanocytic, a shave biopsy is performed. For flat lesions and lesions where it is imperative that a full-thickness specimen is taken, a punch biopsy may be advantageous. Almost all lesions suspected to be melanocytic that are small enough, however, are removed via excisional biopsy. Excisional biopsy removes the entire lesion including a margin of normal skin at a depth that extends into the subcutaneous tissue. This is to ensure proper analysis of the depth profile of the lesion as well as a precautionary method. In suspicious lesions that are potentially non-melanomas, incisional biopsies can be taken where only a portion of the lesion is removed for histological analysis. All of these techniques for biopsy are invasive, time-consuming, and painful for the patient. Additionally, in patients who present with multiple similarly appearing lesions, the selection of the site for biopsy is subjective and could result in misdiagnosis [18].

In the event that pathological evaluation determines the lesion to be cancerous, the treatment options again depend on the type of cancer and its stage. The most common for almost all small lesions is simple surgical excision. For BCC's and SCC's that remain in the epidermis and are in not in cosmetically sensitive areas, electrodesiccation and curettage is a cost-effective, quick, and safe method. Cryosurgery with liquid nitrogen is another viable alternative for superficial cancers in which the tumor is essentially frozen off. Alternatively, topical treatments such as 5-fluorouracil or Imiquimod can be effective tools for *in situ* disease, however these treatments still require close monitoring[20].

Mohs micrographic surgery is the technique with the highest cure rate, and is the treatment of choice for removal of sclerosing and recurrent BCC's in addition to large BCC's and SCC's. In this surgery, the tumor is excised in thin layers which are mapped to their relative location on the patient and pathologically evaluated. If tumor cells appear

in a section, then additional tissue sections are removed until the entire tumor and its margins are removed. Mohs surgery is a significant improvement over the previously mentioned techniques in that it ensures complete removal of the tumor and thus minimizes recurrence, along with minimizing the amount of extraneous tissue removed. Because of the chance for recurrence, patients are monitored after surgery, and in the case of invasive disease, additional treatment options including radiation and chemotherapy can be administered [18].

Although the current gold standard for evaluation of potentially cancerous skin lesions is effective, it is far from perfect. Biopsy is an invasive and painful procedure that is often unnecessary when the lesions are benign. The procedure is also time-consuming and expensive. In addition, a number of elderly patients at the highest risk for skin cancers often present with a large number of suspicious skin lesions, making selection of biopsy locations subjective and laden with the potential for missed diagnoses. Thus, there remains a need for a non-invasive technique that can reliably analyze suspicious lesions *in situ* in real-time and serve as a method to initially guide biopsy and eventually potentially serve as a replacement for histo-pathological analysis. Such a method would enable a significant cost-savings by reducing patient visits and facilitating the diagnostic and therapeutic procedures to be performed in a single visit. Additionally, such an approach would allow for the thorough screening of patients with a large number of suspicious lesions and potentially even reduce the likelihood of undiagnosed disease. Two complimentary optical modalities have recently emerged as promising diagnostic techniques for the skin; Raman spectroscopy and optical coherence tomography.

Raman Spectroscopy

Raman spectroscopy is an optical technique that probes the specific molecular content of a sample by collecting in-elastically scattered light. Raman spectroscopy is a regularly used tool in analytical chemistry to determine the presence of specific molecules in mixed samples, however recent studies have shown it's utility for investigating cancerous human tissues. *In vitro* examples include the analysis of tissues from the breast [21-23], cervix [24], bladder and prostate [25], lung [26], and GI tract [27]. Examples of recent *in vivo* applications include the cervix [28], GI tract [27], and the breast [29].

Raman Spectroscopy Theory

Raman spectroscopy is based on the in-elastic (or Raman) scattering of light. As photons propagate through a medium, they undergo both absorptive and scattering events. In absorption, the energy of the photon is completely transferred to the material, allowing either heat generation (internal conversion) or a re-emission phenomena, such as fluorescence or phosphorescence, to occur. Scattering, however, is normally an elastic process, in which the energy state of the incident photon and the molecule it collides with remain unchanged (Rayleigh/Mie scattering). In Raman scattering, the interaction between the photon and molecule results in an instantaneous transfer of energy between the incident photon and the molecule. The range of energy shifts is quantized and limited to the energy band-gap between the molecule's current vibrational mode and the other possible vibrational modes of the molecule. In cases where the photon is red-shifted due to a transfer of energy to the molecule, the in-elastic scattering is referred to as Stokes scattering. When the photon is blue-shifted due to a transfer of energy from the molecule to the photon, the in-elastic scattering is referred to as anti-Stokes scattering. (fig. 9). Because the scattering interaction is based on the specific allowed vibrational modes of a molecule, every molecule has a unique Raman signature.

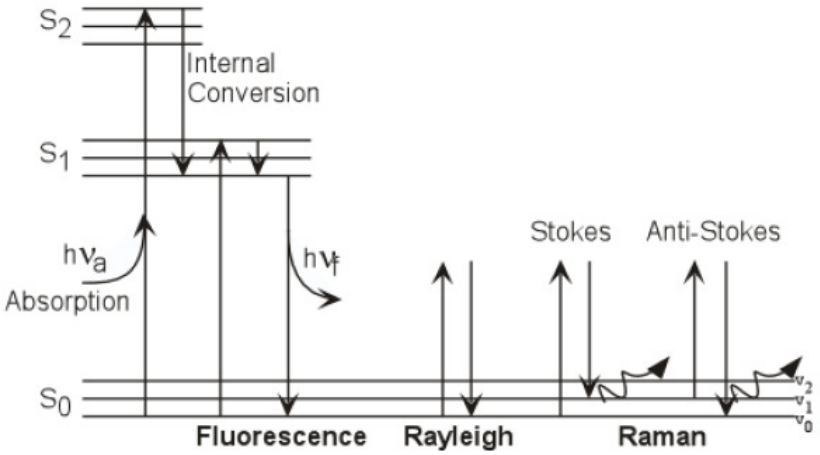

Fig. 9: Jablonski diagram of Raman scattering. In comparison to fluorescence, which involves energy transfers on the order of electronic states, and elastic (Rayleigh) scattering, which involves no energy transfer, Raman scattering involves energy transfers on the order of the vibrational modes of a molecule.

Unfortunately, Raman scattering is a very weak phenomena. For every 10 million elastically scattered photons, approximately 1 is Stokes scattered. Practical measurement

of Raman spectra thus requires extremely sensitive detection hardware, and often high power excitation laser sources. Even with these components, intense tissue auto-fluorescence masks the Raman signal. After detection, post processing techniques are required to subtract the fluorescent background and enable accurate visualization of the Raman spectra. Raman spectra are plots of scattered light intensity as a function of frequency shift in units of wavenumber (cm^{-1}). The region of the Raman spectra where most biological molecules have Raman peaks is from 500 to 2000 cm^{-1}. In contrast to fluorescence spectra, Raman spectra have a number of sharp spectral features that enable easier identification of the contributing molecules. In the context of detecting cancerous tissues, a wide variety of differences are seen in the Raman spectrum. For example, Raman spectra of cancerous tissues exhibit an increased contribution from spectral features that are associated with nucleic acids, corresponding with the known increase in nuclei-to-cytoplasm ratios associated with malignancy [30].

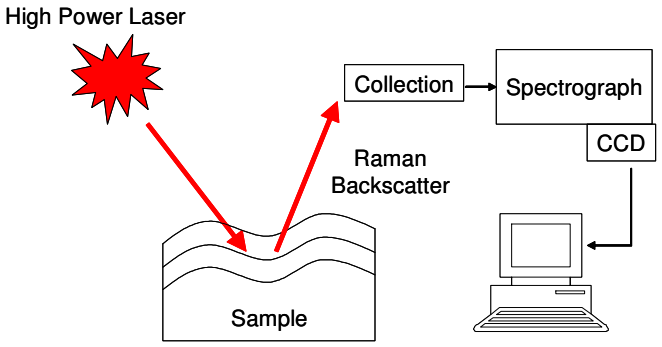

Fig. 10: *Diagram of Typical Raman Spectroscopy System.*

A block diagram of a typical NIR-Raman spectroscopy system is shown in figure10. Raman excitation is provided by a high power mode-locked laser. The Raman scattered light is then collected and spectrally separated by a spectrograph before being detected by a high-sensitivity CCD detector and sent to computer for digitization and processing.

Raman Spectroscopy of Skin Cancer

In the human skin, a number of studies have been performed to examine the biochemical composition of normal and pathological samples both *in vitro* and *in vivo*. Initial experiments using Fourier Transform (FT) Raman on *in vitro* skin samples determined Raman spectroscopy to be a promising technique for the diagnosis of

pathological skin lesions, including BCC, SCC, and malignant melanoma [31]. An extensive *in vitro* FT-Raman study followed, which demonstrated the ability of RS to perform differential diagnosis of malignant melanoma, pigmented nevi, BCC, seborrhoeic keratosis, and normal skin and using neural networks, a machine learning framework [32,33]. Additional *in vitro* studies have demonstrated the sensitivity of confocal RS to pilomatrixoma, a benign tumor of the hair follicles[34], and demonstrated the ability of confocal RS to differentiate BCC and SCC[4]. Fiber optic probe based RS has been demonstrated capable of discriminating BCC from peri-lesional skin in the high-wavenumber (2800 – 3125 cm^{-1}). *In vivo* applications of RS for the detection of skin cancer has been limited to a study using a handheld confocal RS probe to evaluate differences between BCC, SCC, inflammation, and normal skin[35]. The results demonstrate the capability of Raman spectroscopy to perform differential diagnosis of cancerous skin pathologies *in vivo*.

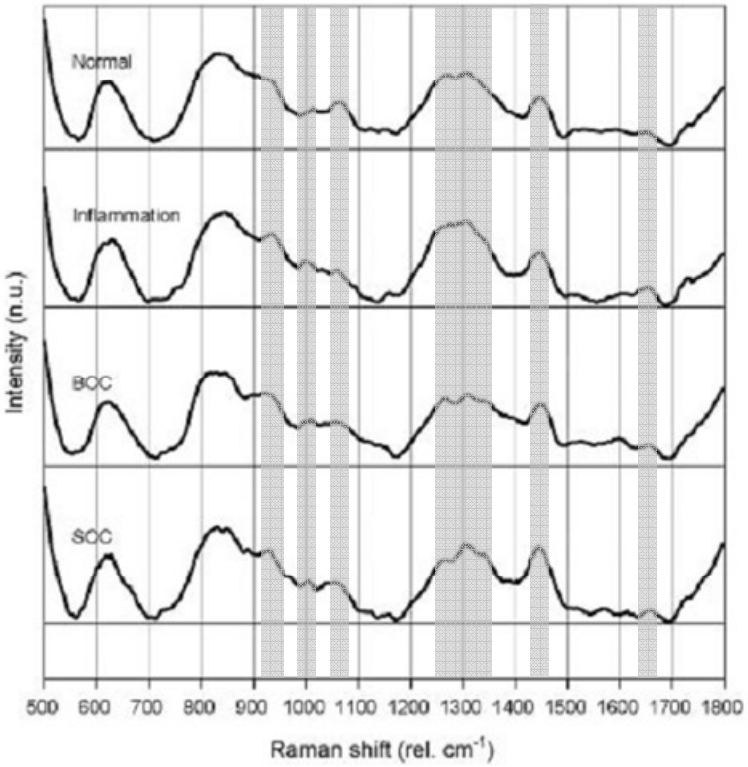

Fig. 11: ***In Vivo confocal Raman spectra.*** *Grey bars indicate regions where spectral differences exist.*[35]

Qualitative differences in confocal Raman spectra acquired from 40 μm below the tissue surface indicate spectral differences between pathological samples at 920-940, 1000-

1010, 1060-1070, 1250-1330, 1445, and 1650 cm^{-1}. The data was classified with an algorithm using a non-linear machine learning algorithm to perform classification of tissue types with a 95% overall accuracy. Taken as a whole, the body of work in RS for skin cancer classification indicates the strength of the technique to perform highly specific classification of multiple cancerous and norn-cancerous tissue types with high accuracy.

Optical Coherence Tomography

Optical Coherence Tomography (OCT) is a recently developed imaging modality capable of generating cross-sectional images of tissue micro-structure [36], function [37], and optical properties [38-40]. The scale of conventional OCT images is on the order of low-magnification histology with imaging resolutions generally better than 25 μm's. *In vivo* applications of OCT are extensive, and include imaging of the eye [41-43], GI tract [44], and coronary vasculature [45].

OCT –Theory

In principle, OCT can be considered analogous to an optical version of ultrasound. While ultrasound images are formed by a transducer emitting ultrasonic pulses and then time gating detection of the tissue echoes, OCT images are formed by using an interferometer to correlate continuous wave light reflected from a reference mirror at a known distance with light reflected from a highly scattering tissue sample at an equivalent distance[36]. Both techniques essentially time gate a signal backscattered from the tissue, only OCT utilizes low-coherence interferometry rather than pulse-echo delay measurements due to the extremely high speed of light.

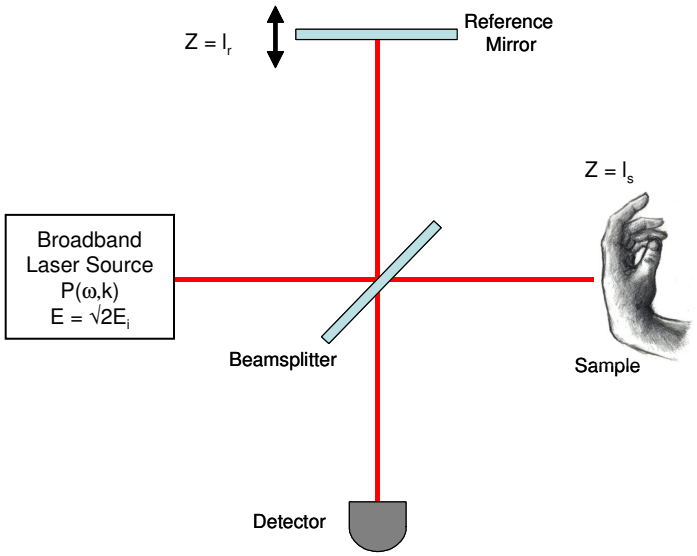

Fig. 12: Low-coherence Michelson interferometer as used in time-domain OCT

A low-coherence Michelson interferometer forms the backbone of the conventional OCT system (fig. 12). Light originating from the source can be represented as the electric field $\sqrt{2}\ E_i$ (with the $\sqrt{2}$ term existing for convenience, as will be seen later), where;

$$E_i = A_i(\omega,k)\ e^{-j(\omega t - kz)} \qquad (1)$$

Here, $A_i(\omega,k)$ is the amplitude of the electric field (E_i) of the broadband laser source, ω (rad/sec) is the angular frequency ($\omega = 2\pi c/\lambda$, where c is the speed of light and λ = wavelength), k (m^{-1}) is the propagation constant ($k = 2\pi/\lambda$), and z (m) is the distance along the optical axis. The electric field incident on the detector (E_d) can be related to the interference generated from the recombination of the electric fields from the reference (E_r) and sample (E_s) arm as;

$$E_d = E_r + E_s$$

$$= \frac{A_i(\omega,k)}{\sqrt{2}}\exp[-j(\omega t - 2kl_r)] + \frac{A_i(\omega,k)\sqrt{R_s(\omega,k,z)}}{\sqrt{2}}\exp[-j(\omega t - 2kl_s)] \qquad (2)$$

With $R_s(\omega,k,z)$ being the wavelength and depth-dependent reflectivity of the biological sample, and l_r and l_s being the positions of the reference mirror and scattering element within the sample, respectively, with respect to the beamsplitter. The electric field is generally detected by an optical power photodetector such that the signal observed out of

the detector is proportional to the square of the electric field. Since the response times of photodiode detectors are far slower than the temporal oscillations in the electric field, the photodetector current output, i_d (A), is averaged in time (indicated below by brackets) and can be given as;

$$i_d = \left\langle \rho \left| E_d{}^2 \right| \right\rangle$$

$$= \int_{-\infty}^{\infty} \frac{\rho A_i(k)^2}{2} \left[1 + R_s(k,z) + 2\sqrt{R_s(k,z)} \cos(2k\Delta l) \right] dk \tag{3}$$

Where ρ represents the detector responsivity (A/W) (with the inherent wavelength dependence implied) and Δl indicates the pathlength difference between the reference and sample arms (l_r-l_s). It is important to note that the signal has both a DC component (the first two additive terms of eq. 3), which is proportional to the incident laser power $A_i(k)^2$, and the sample reflectivity, $R_s(k,z)$, as well as an AC component (the last term in eq. 3), whose amplitude is also proportional to the incident laser power and sample reflectivity, but whose phase is strictly a function of the optical pathlength difference between the two arms of the interferometer. This AC term;

$$i_{d,\,AC} = \int_{-\infty}^{\infty} \rho P(k) \sqrt{R_s(k,z)} \cos(2k\Delta l) dk \tag{4}$$

(where the laser power spectrum $P(k) = A_i(k)^2$), is the interference signal expected from a single scattering element at a specific depth in the sample. The solution to eq. 4 has been previously evaluated for a Gaussian source spectrum of the form;

$$P(k) = \frac{2\sqrt{\ln 2}}{\Delta k \sqrt{\pi}} \exp\left[-\left(\frac{2\sqrt{\ln 2}(k - k_o)}{\Delta k} \right)^2 \right] \tag{5}$$

where k_o is the source center wavenumber and the full-width, half-max (FWHM) of the source spectrum is $\Delta k = 2\pi\Delta\lambda/\lambda_o{}^2$. The resulting expression as a function of pathlength mismatch is[46];

$$i_{d,AC}(\Delta l) = \rho A_i^2(k) \sqrt{R_s(k,z)} \exp\left[-\left(\frac{2\sqrt{\ln 2}\Delta l}{l_c} \right)^2 \right] \cos(2k_o \Delta l) \tag{6}$$

where l_c is the coherence length of the laser source, and is defined as;

$$l_c = \frac{4\ln 2}{\Delta k} = \frac{2\ln 2}{\pi}\frac{\lambda_o^2}{\Delta\lambda} \tag{7}$$

In time-domain OCT, the reference mirror is scanned through a range of distances such that an interference pattern can be acquired as a function of Δl. This interference pattern in equation 6 is an oscillator whose fringe spacing is related to the center wavenumber of the laser source and whose envelope is defined by the convolution of the sample reflectivity profile with the laser source spectrum. When the object in the sample arm is a single reflector, such as a mirror, the interference function acquired from scanning the reference mirror can be considered the one-dimensional impulse response function of the OCT system, known as an interferogram. It is important to note that the width of the Gaussian envelope for a single scattering element in the sample arm is defined by the coherence length of the laser source, l_c. From equations 6 and 7, it can be seen that as the FWHM of the laser source spectrum (Δk or alternatively Δλ) increases, the coherence length decreases and the spread of the one dimensional impulse response function narrows. This is illustrated in figure 13, where the AC component of the photodetector current output (eq. 6) has been simulated for two laser sources; one with an infinite coherence length (top) and one with a short coherence length (bottom). This illustration demonstrates that the broader the bandwidth of the laser source used to illuminate the Michelson interferometer in OCT, the greater the depth resolution. Inconsistencies in dispersion between the reference and sample arm can degrade the depth resolution of an OCT imaging system.

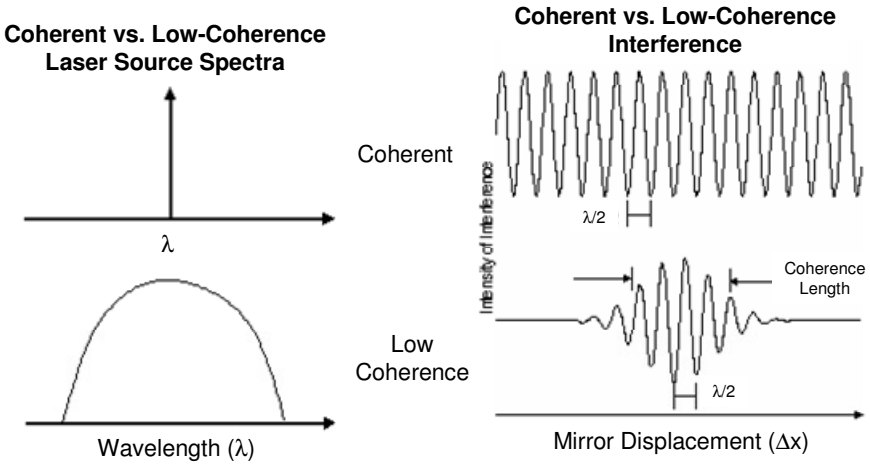

Fig. 13: Coherent vs. Low-Coherence Interference. The interference pattern generated by a perfectly coherent (monochromatic) laser source (top) in a Michelson interferometer setup has no fall-off in intensity as the pathlength mismatch between the two arms is varied because constructive interference between the two beams of light will always occur at λ/2 intervals. The interference pattern generated by a low-coherence (broadband) laser source still demonstrates constructive and destructive interference, with fringe spacing of λ/2. However, because the laser source is not monochromatic, the amplitude of the interference falls of as the pathlength mismatch increases as per equation 6.

Regardless, the key difference between OCT and other optical imaging methods such as confocal microscopy or multi-photon microscopy, is that the depth resolution is dependent on the characteristics of the laser source and independent of the focusing geometry of the sample objective lens. This enables imaging with micron scale axial resolution without the need for high-NA focusing optics.

In Fourier-domain OCT, the reference mirror is held fixed and the photodiode in the detection arm is replaced with a spectrometer that disperses the light as a function of k. A CCD detector then detects the interference spectrum as;

$$I(k) = \left\langle \left| E_d(k) \right|^2 \right\rangle = P(k)R_r + P(k)R_s(k,z) + 2P(k)\sqrt{R_r R_s(k,z)}\cos(2\Delta kl) \qquad (8)$$

The amplitude of the interference signal can then simply be calculated by taking the inverse Fourier transform of I(k), and discarding the excess data that results from the conjugate symmetry of the operation.

Two-dimensional OCT images are built up by transverse scanning the sample beam across the sample and false-color coding the amplitude of the backscattered interference (fig. 14).

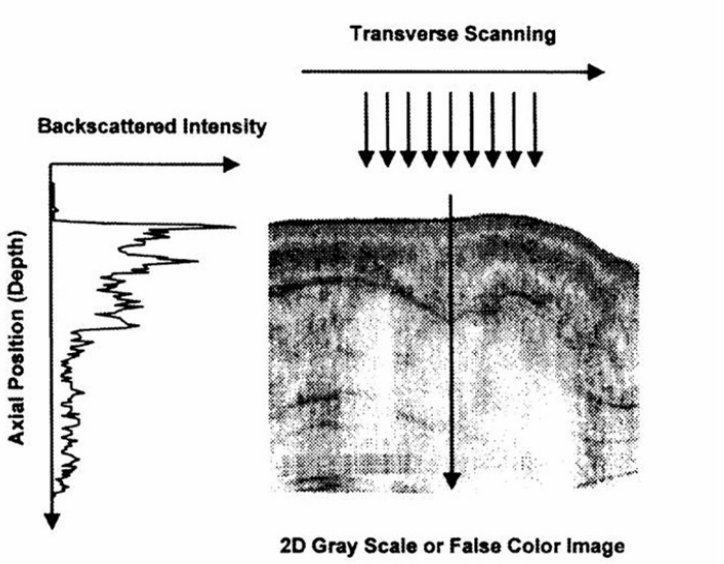

Fig. 14: OCT image construction. Axial profiles of backscattered intensity vs. depth are generated by scanning the mirror in the reference arm, while 2-D image construction is performed by transverse scanning of the sample beam [8].

OCT of Skin Cancer

OCT has extensively been applied to the *in vivo* imaging of the skin to examine dermatitis, psoriasis, as well as the effect of varies ointments, water, tape stripping, and UV radiation on normal skin [47-51]. A number of papers have demonstrated the potential utility of OCT for imaging skin cancers. A number of studies have reported the appearance of various types of skin cancer in OCT, including BCC and melanoma (fig. 15). Tumor cell nests appear as dark, hypo-reflective regions. In melanoma, it is possible to identify the elongated rete ridges. Polarization sensitive - OCT (PS-OCT) imaging of BCC has been reported, and the results indicate that tumors alter phase retardation as function of depth[52]. Histomorphometric correlation between OCT and histology in BCC and malignant melanomas has been verified[9], indicating the suitability of OCT to quantitatively assess Breslow thickness in melanomas, an important parameter for staging.

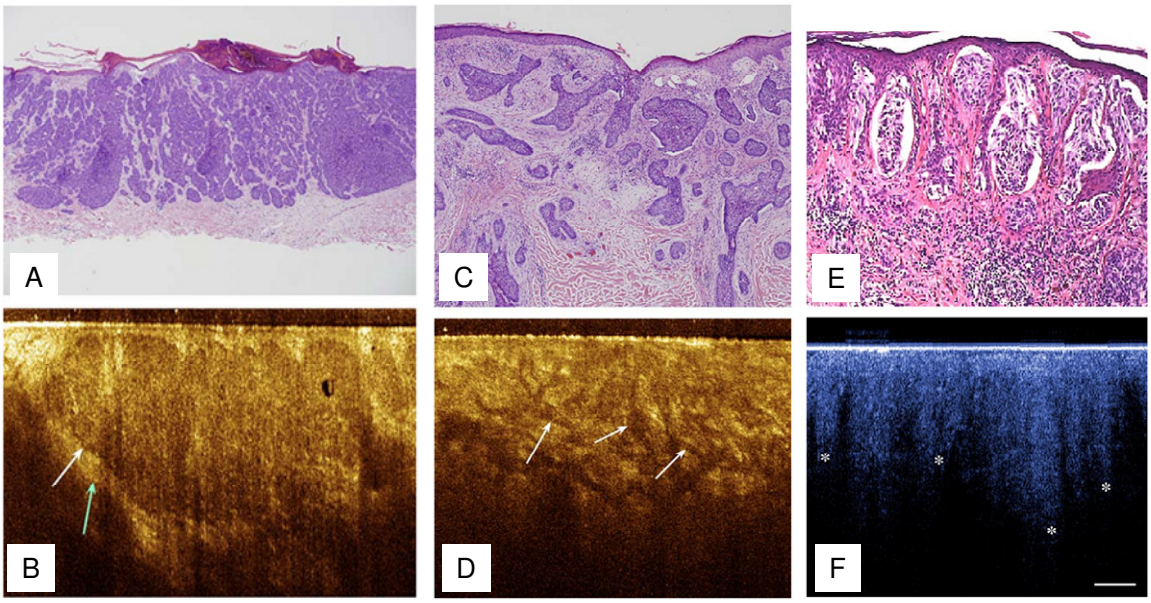

Fig. 15: OCT of BCC and malignant melanoma. The histology (A) and OCT (B) of a nodular BCC[11]. Histology (C) and OCT (D) of an infiltrating BCC[11]. Histology (E) and OCT (F) of malignant melanoma[53].

Despite the high-resolution of OCT images, they remain difficult to evaluate to the untrained eye. Recently, a Danish groups has undertaken the task of interpreting and classifying OCT images of BCC and actinic keratoses (AK). Jorgensen et. al. identified a number of image features related of BCC and AK, labeled a set of 78 lesions from 34 patients according to these features, and attempted to perform classification of the images

with support vector machine learning algorithm. The study reported a classification accuracy of 81% for BCC and 73% for AK. Mogensen et. al. undertook the task of training a group of pathologists and dermatologists to visualize the morphological features of OCT and PS-OCT images of BCC, AK, and normal skin on a training set of 50 images, and then asked the physicians to classify > 200 images, with nearly half normal and the remaining half split approximately 60:40 BCC:AK. The results indicated that the best, most experienced observers could distinguish BCC from normal skin quite well, with a sensitivity of ≈ 80% and a specificity of ≈ 95%. AK and BCC, however, were virtually indistinguishable due to their similar morphological appearance in OCT. These results indicate the strength of OCT in visualizing features of disease with high sensitivity, but the inability to distinguish AK from BCC indicate the low specificity to disease class.

References

1. B. J. Ford, "First Steps in Experimental Microscopy, Leeuwenhoek as Practical Scientist," The Microscope **43**(2), 47-57 (1995).
2. A. Mahadevan-Jansen, "Raman Spectroscopy: From Benchtop to Bedside," in *Biomedical Photonics Handbook*, T. Vo Dinh, ed. (CRC Press, Boca Raton, FL, 2003), pp. 30:31-27.
3. A. Robichaux-Viehoever, E. M. Kanter, H. Shappell, D. Billheimer, H. Jones III, and A. Mahadevan-Jansen, "Characterization of Raman Spectra Measured in Vivo for the Detection of Cervical Dysplasia," Applied Spectroscopy **61**(9), 986-993 (2007).
4. C. A. Lieber, S. K. Majumder, D. Billheimer, D. L. Ellis, and A. Mahadevan-Jansen, "Raman microspectroscopy for skin cancer detection in vitro," J Biomed Opt **13**(2), 024013 (2008).
5. C. A. Lieber, S. K. Majumder, D. L. Ellis, D. D. Billheimer, and A. Mahadevan-Jansen, "In vivo nonmelanoma skin cancer diagnosis using Raman microspectroscopy," Lasers in Surgery and Medicine **40**(7), 461-467 (2008).
6. A. Nijssen, T. C. B. Schut, F. Heule, P. J. Caspers, D. P. Hayes, M. H. A. Neumann, and G. J. Puppels, "Discriminating basal cell carcinoma from its surrounding tissue by Raman spectroscopy," Journal of Investigative Dermatology **119**(1), 64-69 (2002).
7. M. A. Short, H. Lui, D. McLean, H. Zeng, A. Alajlan, and X. K. Chen, "Changes in nuclei and peritumoral collagen within nodular basal cell carcinomas via confocal micro-Raman spectroscopy," J Biomed Opt **11**(3), 34004 (2006).
8. J. G. Fujimoto, *Handbook of Optical Coherence Tomography,* 1st ed. (Marcel Dekker, Inc., New York, 2002).
9. F. G. Bechara, T. Gambichler, M. Stucker, A. Orlikov, S. Rotterdam, P. Altmeyer, and K. Hoffmann, "Histomorphologic correlation with routine histology and optical coherence tomography," Skin Res Technol **10**(3), 169-173 (2004).
10. V. de Giorgi, M. Stante, D. Massi, L. Mavilia, P. Cappugi, and P. Carli, "Possible histopathologic correlates of dermoscopic features in pigmented melanocytic lesions identified by means of optical coherence tomography," Exp Dermatol **14**(1), 56-59 (2005).
11. J. M. Olmedo, K. E. Warschaw, J. M. Schmitt, and D. L. Swanson, "Optical coherence tomography for the characterization of basal cell carcinoma in vivo: a pilot study," J Am Acad Dermatol **55**(3), 408-412 (2006).
12. , retrieved http://www.usuhs.mil/pat/surg_path/nlhist/pictures/nlthskin.gif.
13. T. P. Habif, "Clinical Dermatology: A color guide to diagnosis and therapy," (Mosby, St. Louis, 1996).
14. R. Graham-Brown and T. Burns, *Lecture notes on Dermatology,* 8th ed. (Blackwell Science, Oxford, 2002).

15. G. F. Murphy and A. J. Herzberg, *Atlas of Dermatopathology,* 1st ed. (W.B. Saunders Co., Philadelphia, 1996).
16. "Cancer Reference Information: Skin Cancer" (American Cancer Society, 2006), retrieved http://www.cancer.org/docroot/cri/cri_0.asp.
17. "Cancer Facts and Figures: 2006" (American Cancer Society, 2006), retrieved http://www.cancer.org/downloads/STT/CAFF2006PWSecured.pdf.
18. R. L. Moy, D. P. Taheri, and A. Ostad, *Practical Management of Skin Cancer* (Lippincott-Raven Publishers, Philadelphia, 1999).
19. A. Mehregan, K. Hashimoto, D. Mehregan, and D. Mehregan, *Pinkus' Guide to Dermatohistopathology,* 6th ed. (Appleton & Lange, East Norwalk, CT, 1995).
20. J. A. Neville, E. Welch, and D. J. Leffell, "Management of nonmelanoma skin cancer in 2007," Nat Clin Pract Oncol **4**(8), 462-469 (2007).
21. A. S. Haka, K. E. Shafer-Peltier, M. Fitzmaurice, J. Crowe, R. R. Dasari, and M. S. Feld, "Identifying microcalcifications in benign and malignant breast lesions by probing differences in their chemical composition using Raman spectroscopy," Cancer Res **62**(18), 5375-5380 (2002).
22. C. J. Frank, R. L. McCreery, and D. C. Redd, "Raman spectroscopy of normal and diseased human breast tissues," Anal Chem **67**(5), 777-783 (1995).
23. N. Stone, C. Kendall, J. Smith, P. Crow, and H. Barr, "Raman spectroscopy for identification of epithelial cancers," Faraday Discuss **126**, 141-157; discussion 169-183 (2004).
24. A. Mahadevan-Jansen, M. F. Mitchell, N. Ramanujam, A. Malpica, S. Thomsen, U. Utzinger, and R. Richards-Kortum, "Near-infrared Raman spectroscopy for in vitro detection of cervical precancers," Photochem Photobiol **68**(1), 123-132 (1998).
25. P. Crow, A. Molckovsky, N. Stone, J. Uff, B. Wilson, and L. M. WongKeeSong, "Assessment of fiberoptic near-infrared raman spectroscopy for diagnosis of bladder and prostate cancer," Urology **65**(6), 1126-1130 (2005).
26. Z. Huang, A. McWilliams, H. Lui, D. I. McLean, S. Lam, and H. Zeng, "Near-infrared Raman spectroscopy for optical diagnosis of lung cancer," Int J Cancer **107**(6), 1047-1052 (2003).
27. A. Molckovsky, L. M. Song, M. G. Shim, N. E. Marcon, and B. C. Wilson, "Diagnostic potential of near-infrared Raman spectroscopy in the colon: differentiating adenomatous from hyperplastic polyps," Gastrointest Endosc **57**(3), 396-402 (2003).
28. A. Mahadevan-Jansen, M. F. Mitchell, N. Ramanujam, U. Utzinger, and R. Richards-Kortum, "Development of a fiber optic probe to measure NIR Raman spectra of cervical tissue in vivo," Photochem Photobiol **68**(3), 427-431 (1998).
29. A. S. Haka, Z. Volynskaya, J. A. Gardecki, J. Nazemi, J. Lyons, D. Hicks, M. Fitzmaurice, R. R. Dasari, J. P. Crowe, and M. S. Feld, "In vivo margin assessment during partial mastectomy breast surgery using raman spectroscopy," Cancer Res **66**(6), 3317-3322 (2006).
30. A. Mahadevan-Jansen and R. Richards-Kortum, "Raman Spectrscopy for the Detection of Cancers and Precancers," Journal of Biomedical Optics **1**(1), 31-70 (1996).

31. M. Gniadecka, H. C. Wulf, O. F. Nielsen, D. H. Christensen, and J. Hercogova, "Distinctive molecular abnormalities in benign and malignant skin lesions: studies by Raman spectroscopy," Photochem Photobiol **66**(4), 418-423 (1997).
32. S. Sigurdsson, P. A. Philipsen, L. K. Hansen, J. Larsen, M. Gniadecka, and H. C. Wulf, "Detection of skin cancer by classification of Raman spectra," IEEE Trans Biomed Eng **51**(10), 1784-1793 (2004).
33. M. Gniadecka, P. A. Philipsen, S. Sigurdsson, S. Wessel, O. F. Nielsen, D. H. Christensen, J. Hercogova, K. Rossen, H. K. Thomsen, R. Gniadecki, L. K. Hansen, and H. C. Wulf, "Melanoma diagnosis by Raman spectroscopy and neural networks: structure alterations in proteins and lipids in intact cancer tissue," J Invest Dermatol **122**(2), 443-449 (2004).
34. W. T. Cheng, M. T. Liu, H. N. Liu, and S. Y. Lin, "Micro-Raman spectroscopy used to identify and grade human skin pilomatrixoma," Microsc Res Tech **68**(2), 75-79 (2005).
35. C. A. Lieber, S. K. Majumder, D. L. Ellis, D. D. Billheimer, and A. Mahadevan-Jansen, "In vivo nonmelanoma skin cancer diagnosis using Raman microspectroscopy," Lasers Surg Med **40**(7), 461-467 (2008).
36. D. Huang, E. A. Swanson, C. P. Lin, J. S. Schuman, W. G. Stinson, W. Chang, M. R. Hee, T. Flotte, K. Gregory, C. A. Puliafito, and J. G. Fujimoto, "Optical Coherence Tomography," Science **254**(5035), 1178-1181 (1991).
37. J. A. Izatt, M. D. Kulkarni, S. Yazdanfar, J. K. Barton, and A. J. Welch, "In vivo bidirectional color Doppler flow imaging of picoliter blood volumes using optical coherence tomograghy," Optics Letters **22**(18), 1439-1441 (1997).
38. J. F. deBoer, T. E. Milner, M. J. C. vanGemert, and J. S. Nelson, "Two-dimensional birefringence imaging in biological tissue by polarization-sensitive optical coherence tomography," Optics Letters **22**(12), 934-936 (1997).
39. U. Morgner, W. Drexler, F. X. Kartner, X. D. Li, C. Pitris, E. P. Ippen, and J. G. Fujimoto, "Spectroscopic optical coherence tomography," Optics Letters **25**(2), 111-113 (2000).
40. D. J. Faber, E. G. Mik, M. C. Aalders, and T. G. van Leeuwen, "Light absorption of (oxy-)hemoglobin assessed by spectroscopic optical coherence tomography," Opt Lett **28**(16), 1436-1438 (2003).
41. C. A. Puliafito, M. R. Hee, C. P. Lin, E. Reichel, J. S. Schuman, J. S. Duker, J. A. Izatt, E. A. Swanson, and J. G. Fujimoto, "Imaging of Macular Diseases with Optical Coherence Tomography," Ophthalmology **102**(2), 217-229 (1995).
42. E. A. Swanson, J. A. Izatt, M. R. Hee, D. Huang, C. P. Lin, J. S. Schuman, C. A. Puliafito, and J. G. Fujimoto, "In-Vivo Retinal Imaging by Optical Coherence Tomography," Optics Letters **18**(21), 1864-1866 (1993).
43. M. R. Hee, J. A. Izatt, E. A. Swanson, D. Huang, J. S. Schuman, C. P. Lin, C. A. Puliafito, and J. G. Fujimoto, "Optical Coherence Tomography of the Human Retina," Archives of Ophthalmology **113**(3), 325-332 (1995).
44. M. V. Sivak, Jr., K. Kobayashi, J. A. Izatt, A. M. Rollins, R. Ung-Runyawee, A. Chak, R. C. Wong, G. A. Isenberg, and J. Willis, "High-resolution endoscopic imaging of the GI tract using optical coherence tomography," Gastrointest Endosc **51**(4 Pt 1), 474-479 (2000).

45. I. K. Jang, G. Tearney, and B. Bouma, "Visualization of tissue prolapse between coronary stent struts by optical coherence tomography: comparison with intravascular ultrasound," Circulation **104**(22), 2754 (2001).
46. J. A. Izatt, M. D. Kulkarni, H. W. Wang, K. Kobayashi, and M. V. Sivak, "Optical coherence tomography and microscopy in gastrointestinal tissues," Ieee Journal of Selected Topics in Quantum Electronics **2**(4), 1017-1028 (1996).
47. J. Welzel, E. Lankenau, R. Birngruber, and R. Engelhardt, "Optical coherence tomography of the skin," Curr Probl Dermatol **26**, 27-37 (1998).
48. G. Vargas, E. K. Chan, J. K. Barton, H. G. Rylander, 3rd, and A. J. Welch, "Use of an agent to reduce scattering in skin," Lasers Surg Med **24**(2), 133-141 (1999).
49. J. Welzel, "Optical coherence tomography in dermatology: a review," Skin Res Technol **7**(1), 1-9 (2001).
50. J. Welzel, M. Bruhns, and H. H. Wolff, "Optical coherence tomography in contact dermatitis and psoriasis," Arch Dermatol Res **295**(2), 50-55 (2003).
51. J. Welzel, C. Reinhardt, E. Lankenau, C. Winter, and H. H. Wolff, "Changes in function and morphology of normal human skin: evaluation using optical coherence tomography," Br J Dermatol **150**(2), 220-225 (2004).
52. J. Strasswimmer, M. C. Pierce, B. H. Park, V. Neel, and J. F. de Boer, "Polarization-sensitive optical coherence tomography of invasive basal cell carcinoma," J Biomed Opt **9**(2), 292-298 (2004).
53. T. Gambichler, P. Regeniter, F. G. Bechara, A. Orlikov, R. Vasa, G. Moussa, M. Stucker, P. Altmeyer, and K. Hoffmann, "Characterization of benign and malignant melanocytic skin lesions using optical coherence tomography in vivo," J Am Acad Dermatol **57**(4), 629-637 (2007).

CHAPTER II

MANUSCRIPT 1

Fiber Optic Probe Based Raman Spectroscopy for *in vivo* Non-melanoma Skin Cancer Detection

Chetan A. Patil[1], Darrel L. Ellis[2,3], and Anita Mahadevan-Jansen[1]

[1]Department of Biomedical Engineering, Vanderbilt University, Nashville TN
[2]Division of Dermatology, Department of Medicine, Vanderbilt University, Nashville TN
[3]Dermatology Service, Veterans Affairs Tennessee Valley Healthcare System, Nashville TN

Prepared for Submission to Lasers in Surgery and Medicine or Journal of Investigative Dermatology

Abstract

Skin cancer is the most commonly occurring of all cancers, and its incidence is growing. Realizing favorable outcomes requires early diagnosis, for which the current gold standard is biopsy followed by histopathology. This process can be invasive, subjective, time consuming, and costly. Raman spectroscopy is a non-invasive optical technique capable of characterizing the biochemical composition of skin and performing disease classification based on statistical methods. Here, we demonstrate the potential utility of fiber optic probe based Raman spectroscopy for the *in vivo* diagnosis of non-melanoma skin cancers. Patients scheduled to undergo routine removal of skin lesions were enrolled in the study. Measurements were made from the lesion center and perilesional normal skin of 34 lesions (18 BCC/SCC, 16 non-cancerous inflammation/scar). Difference spectra (lesion – perilesional normal) were calculated to account for the natural variation of Raman skin spectra. A spectral classification algorithm was developed with Sparse Multinomial Logistic Regression (SMLR). Using leave-one-patient out cross validation, Raman spectroscopy was able to perform non-invasive diagnosis of disease with a sensitivity of 78 % and a specificity of 94%, indicating the potential utility of the technique for skin cancer diagnosis.

Introduction

Skin cancer is the most commonly occurring of all cancers, accounting for more than a 1.7 million incidences in the United States annually[1]. In addition, the incidence rate for skin cancer is growing, particularly among young Caucasian women aged 15-34 (3.8% annually) and Caucasian men aged over 65 (8.8% annually)[1]. Realizing good outcomes for patients with skin cancer relies on early detection. The two most common types of skin cancer, basal cell carcinoma (BCC) and squamous cell carcinoma (SCC), are highly curable if detected at an early stage. Although the most dangerous skin cancer, malignant melanoma, can have a 5 year survival rate of only 16% at its most advanced stage, cases detected *in situ* have survival rates of 99%[1]. The current gold standard for screening and detection is visual inspection followed by biopsy and histopathology.

Visual inspection can be difficult and it is often easy to overlook disease. In many cases, biopsy or preemptive removal of a large number of lesions can serve as a simple solution; however this approach is subjective, invasive, time-consuming, and costly. Based on a 2005 estimate, the total negative skin cancer biopsies outnumber non-melanoma and melanoma diagnoses by approximately 40:1[2]. Assuming the average direct cost of biopsy and histology to be $500 in the US, the cost of negative biopsies can be roughly estimated at $30 billion. Despite the fact that morbidity due to skin cancer is low, it is clear that the benefit of accurate, non-invasive diagnosis of skin cancer have a significant impact on patient comfort and the overall cost of skin cancer management.

Optical techniques are one approach for non-invasive skin cancer diagnosis. A number of imaging-based techniques including optical coherence tomography[3] and confocal microscopy[4] are capable of visualizing the microstructural features of disease, however the qualitative nature of image analysis and the lack of molecular specificity can make accurate disease classification difficult. Spectroscopic techniques can be considered advantageous due to their inherent molecular specificity and the quantitative nature of spectral analysis. Fluorescence spectroscopy has shown promise for non-invasive detection of skin cancer[5], however intrinsic fluorophores in the UV-visible spectrum are limited to NaDH, FAD, and porphyrins, which can constrain tissue classification. Novel approaches utilizing near-infrared two-photon excitation to isolate melanin fluorescence from the tissue background[6] are beneficial specifically for the challenge of melanoma detection, however they cannot be generalized for the detection of all skin cancers.

Raman spectroscopy is a technique that probes molecules on the vibrational level. The relative shift of the in-elastically scattered light contains information related to the specific molecular composition of the sample. In particular, the Raman fingerprint region from 500 to 2000 cm^{-1} contains features characteristic of wide range of biomolecules, including nucleic acids, lipids, collagen and other proteins. In comparison with fluorescence or diffuse reflectance spectroscopy, Raman spectroscopy has been demonstrated to perform detection of cancer with superior specificity and overall classification accuracy[7]. *In vivo*, Raman spectroscopy has been demonstrated capable of detecting cancers in tissues such as the cervix[8] and gastrointestinal (GI) tract[9].

In the skin, a number of *in vitro* studies have demonstrated the diagnostic potential of confocal Raman spectroscopy or Raman micro spectroscopy. Nijssen et. al. demonstrated the ability of Raman spectroscopy to differentiate BCC from the surrounding dermis and epidermis, as well as detect subtle changes within the peritumoral dermis associated with inflammation and changes in collagen content[10]. The molecular specificity of Raman was highlighted in a study by Lieber et. al. which reported direct multi-class separation of normal skin, BCC, SCC, and melanoma with a non-linear Bayesian classification algorithm[11]. Fourier-Transform Raman spectroscopy in combination with neural networks further demonstrated the ability to perform classification of skin cancers from non-malignant lesions such as benign pigmented nevi and seborrheic keratosis[12, 13]. Confocal micro-spectroscopy with spatial resolution of 1 μm has detected differences between the nuclei of BCC cells and normal epidermal cells, further underscoring the biochemical specificity of Raman spectroscopy[14]. Recently, the diagnostic potential of Raman micro-spectroscopy was validated by a study that performed *in vivo* measurement of skin lesions with a handheld device and was able to separate normal skin, BCC, SCC, and inflamed scar tissue with a 95% overall classification accuracy[15].

The motivation behind previous work utilizing confocal Raman spectroscopy has been to isolate signal arising from cancerous cells by rejecting contributions from the epidermis and focusing directly on the cancer cells of interest. Theoretically this is ideal, however there are a number of reasons to believe such an approach may not be necessary. First, previous studies using contact fiber-optic probes with non-confocal collection geometries have been demonstrated effective for the detection of cancer in the cervix and GI tract, both of which are epithelial tissues that follow a pathological progression to cancer similar to the skin. Secondly, there are a number of reports that demonstrate the sensitivity of Raman spectroscopy to peritumoral changes in the dermis[10, 14, 16]. In the clinical study performed by Lieber et. al., all measurements were acquired from a depth of 40 μm below the tissue surface due to the impracticality of performing a full-depth scan on each lesion. Follow up histopathology indicated the depth of tumor cell nests varied significantly and in most cases was far below the depth probed. The excellent classification accuracy reported in the study suggests that going to great lengths to

acquire light scattered from tumor cells may not be necessary for the purposes of diagnosis. In particular, non-contact confocal collection geometries require much longer integration times (approx. 30 sec) due to rejection of out-of-plane light and less efficient light transmission through the optical system in the absence of index matching. Fiber optic probes, on the other hand are much more efficient and capable of collecting spectra in approximately 3 sec, which greatly simplifies clinical collection of spectra. Classification of BCC from normal tissue using a non-confocal fiber-optic has recently been demonstrated *in vitro*[17]. This study only collected the high-wavenumber (2800-3125 cm^{-1}) Raman shift band, a region that can be dominated by contributions from collagen and contain less distinctive features than the fingerprint region[17]. This goal of this study is to assess the performance of fiber-optic probe based Raman spectroscopy for *in vivo* skin cancer diagnosis.

Materials and Methods

Raman Instrumentation

A schematic diagram of the fiber optic probe Raman system is illustrated in figure 2.1. A 785 nm multi-mode laser diode (Innovative Photonics Solutions, Inc.) is coupled into a 7 collection-around-1 illumination fiber optic probe (Visonex). The illumination fiber is a 400 μm low-OH fiber. Within the probe is a 785 nm in-line filter that reduces Raman scatter generated within the fiber. For each measurement, the laser power at the sample was set to 80 mW. The 7 300 μm collection fibers are angle polished and thus steer the collection geometry towards the optical axis of the illumination fiber for more efficient collection in the near-field. The fiber probe contains in-line 785 nm notch filters in each of the collection fiber optical paths to reduce elastic scatter and thus further minimize Raman signal generated in the fiber optic probe. The collection fibers are re-arranged into a vertical line at the entrance to the spectrograph in order to best fill the 100 μm slit. Within the spectrograph the light is again notch filtered. A back-illuminated, deep-depletion, thermo-electrically cooled CCD camera detects the light and relays the

data to a laptop computer for processing. The spectral resolution of the detection is 7.7 cm^{-1}.

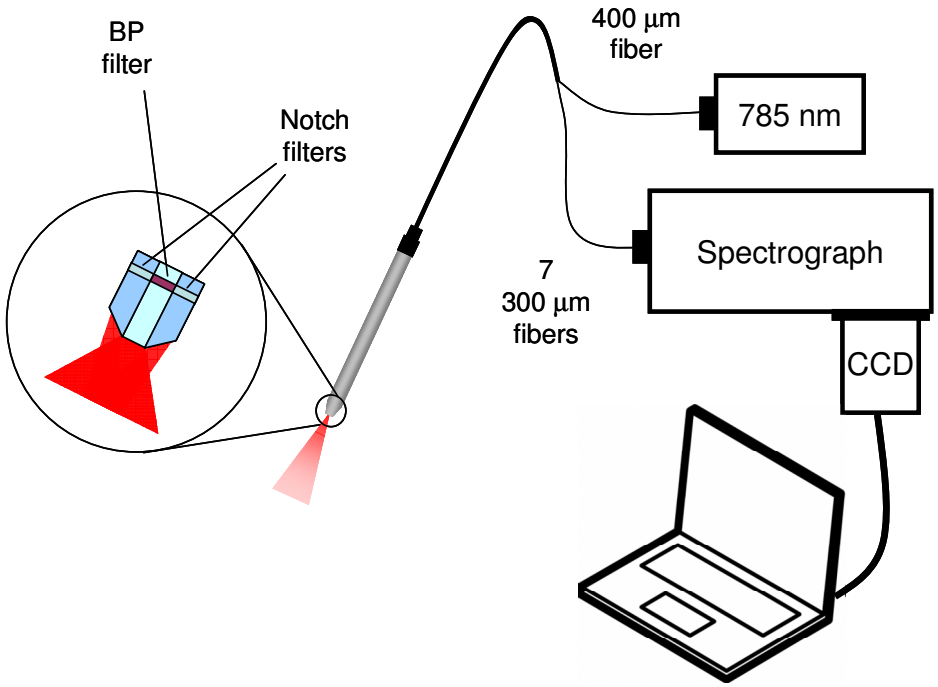

Fig. 2.1: Fiber Optic Probe based Raman Spectroscopy System. A 785nm source is fiber coupled to a fiber optic probe that delivers 80 mW of light to the sample. The 7-around-1 fiber probe contains in line notch and band pass (BP) filtering to minimize Raman resulting from the fiber, and minimize collection of elastic scatter.

Study Protocol

All procedures for patient enrollment, informed consent, experimental protocol, and specimen collection / retention were approved by the Vanderbilt University Institutional Review Board.

All patients presenting at the Vanderbilt dermatology clinic scheduled for routine resection of skin lesions previously identified as cancerous via pathology were eligible for enrollment. Fiber probe and lesion surface were swabbed with alcohol prior to measurement. Three (3) Raman spectra were acquired from within the visible clinical margins of the lesion (as determined by the physician performing the resection), and 3 spectra were acquired from adjacent normal skin within the planned excision boundary. After each measurement, the position of the probe tip was marked with ink, and a 2mm

punch biopsy was taken from both the lesion and normal skin measurement sites for correlation with Raman measurement. All spectra were acquired in < 5 seconds per acquisition. In total, 42 patients were enrolled in the study, with 45 lesions measured.

Spectral Pre-processing

Prior to each day's data collection, the spectral dispersion of the detection system was calibrated using the atomic emission lines of a neon-argon lamp, and variations in spectral throughput of the system were calibrated using a NIST-certified quartz-tungsten-halogen lamp. Relative Raman wavenumber shift was calibrated with acetaminophen and naphthalene standards. Data was binned to ½ the spectral resolution, high frequency noise was removed with a 2^{nd} order Savitzky-Golay filter with a window size twice the spectral resolution. Finally, background tissue autofluorescence was subtracted with a modified polynomial fitting algorithm[18], and the resulting spectra were area normalized in order to maintain potentially relevant information from all peaks. The 3 spectra from each measurement location were averaged to produce a single spectrum per position.

Data Analysis

Due to the high heterogeneity of skin, all analysis was performed on difference spectra, calculated as; lesion mean spectrum – adjacent normal mean spectrum. Despite the fact that each patient had a pathologically confirmed skin cancer prior to enrollment, in some cases the initial biopsy used for diagnosis actually removed the entire cancer, leaving behind normal scar tissue. Thus, our data set included 3 classes; inflammation / scar (non-cancerous), BCC, and SCC. In order to qualitatively determine spectral ranges where differences between all classes of lesion (defined as scar/inflammation, BCC, and SCC) spectra and normal spectra were present, the pooled standard error of all the data was calculated as a function of wavenumber[15]. Spectral bands falling outside the normal standard error were deemed to be significant. Analysis was performed on the data stratified into simply 2 classes; inflammation / scar (non-cancerous) and cancerous (BCC and SCC) due to the limited sample size. Here, the standard error of just the normal data was calculated to determine significantly different spectral bands.

Quantitative analysis was performed with Sparse Multinomial Logistic Regression (SMLR), an algorithm based on the sparse Bayesian machine-learning

framework of statistical pattern recognition[19]. The algorithm operates on weighted basis functions with sparsity promoting prior terms that drive basis functions to significance or zero. The algorithm then uses a multinomial logistic regression model to construct decision boundaries that optimally separate data classes. The output of SMLR is a set of predicted posterior probabilities of class membership for each input spectrum. The probability of membership to class, ***i***, of each basis function, ***x***, is given in equation 2.1.

$$P\left(y^{(i)} = 1 | \boldsymbol{x}, w\right) = \frac{\exp\left(\boldsymbol{w}^{(i)^T}\boldsymbol{x}\right)}{\sum_{j=1}^{m} \exp\left(\boldsymbol{w}^{(j)^T}\boldsymbol{x}\right)}$$

Equation 2.1: Probability of Class Membership in SMLR[19].

Optimization and sparsity promotion of the weight vector, ***w***, is the primary advantage of SMLR. The promotion of sparsity is a critical feature for generalizability, based on machine learning theory. Spectral classification is assigned to the class with the highest posterior probability.

Results

Representative pathology sections used for the assignment of tissue class are shown in figure 2.2. In total, 34 lesions from 32 patients were retained of the 45 measured lesions, with 14 from BCC, 4 from SCC, and 16 from scar/inflammation. Lesions were excluded due to instrumentation variations that introduced systemic bias in the data (5), errors in pathological processing that resulted in unclassifiable tissue specimens (2), spectra with large, non-Raman features (i.e. fluorescent lighting, cosmic rays) that could not be removed without skewing the data(3), and a lesion in which the operating physician was unable to perform a biopsy of the peri-lesional normal measurement site due to a change the resection plan(1).

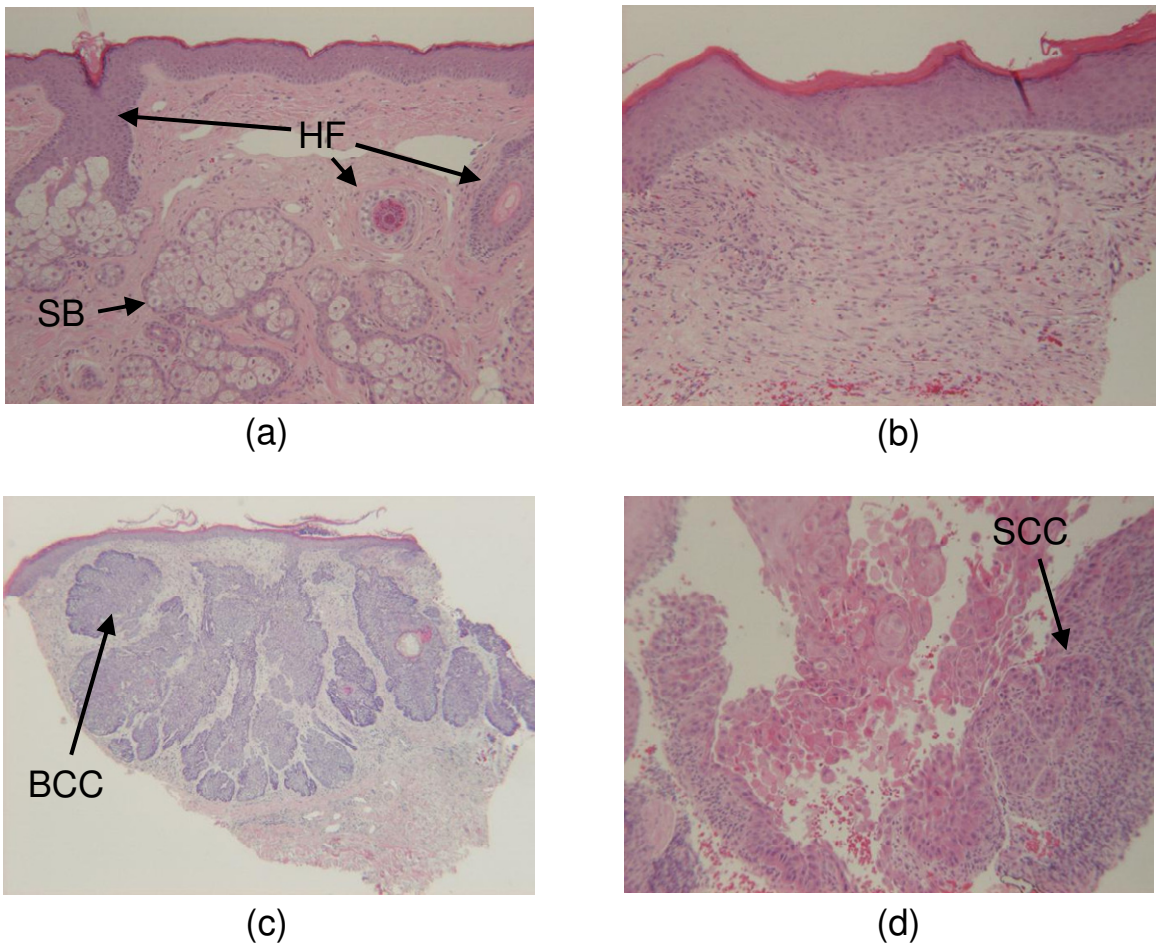

Fig. 2.2: Representation Histopathology of tissue samples acquired at Raman spectroscopy measurement sites. The heterogeneity of normal skin (a) is seen in the presence of sebaceous glands (SB) and hair follicle (HF) cross sections (10x). Scar tissue and inflammation has distinct features, including a relatively flat epidermal-dermal junction, predominantly horizontal arrangement of the collagen network, and the presence of dark staining inflammatory cells dispersed throughout the dermis (10x). BCC (c, 4x) features include the presence of clear basophilic tumor cells nests with nuclear atypia. SCC tumor cells, in contrast, are typically eosinophillic, but also contain atypical nuclei as identified (d, 10x).

The mean spectra from the lesions retained for analysis are shown in figure 2.2. The grey region indicates the variance of normal skin spectra. The spectral features observed in the data as a whole are generally similar to those reported in literature of Raman spectroscopy in the skin. The spectral feature near 849 cm^{-1} has been attributed to the amino acid tyrosine[20]. The peak at 940 cm^{-1} is attributed to the C-C stretch in hydroxyproline and collagen[21]. The 1003 cm^{-1} peak is commonly assigned to phenylalanine ring breathing[10, 20, 22]. The 1076 cm^{-1} peak is attributed to PO_2 symmetric

stretching present in both lipids and nucleic acids[10, 20, 22]. The 1265 cm^{-1} peak is attributed to C-N stretching in amide III[20, 22]. The 1304 and 1444 cm^{-1} peaks are assigned to CH_2 modes that are common in a number of molecules including lipids, proteins, adenine, and cytosine[10, 20, 22]. The 1667 cm^{-1} peak is attributed to the C=O stretch in amide I[10, 20, 22]. Note that in large part, all lesion types lie within the normal spectra variance, indicating that direct classification will likely be difficult.

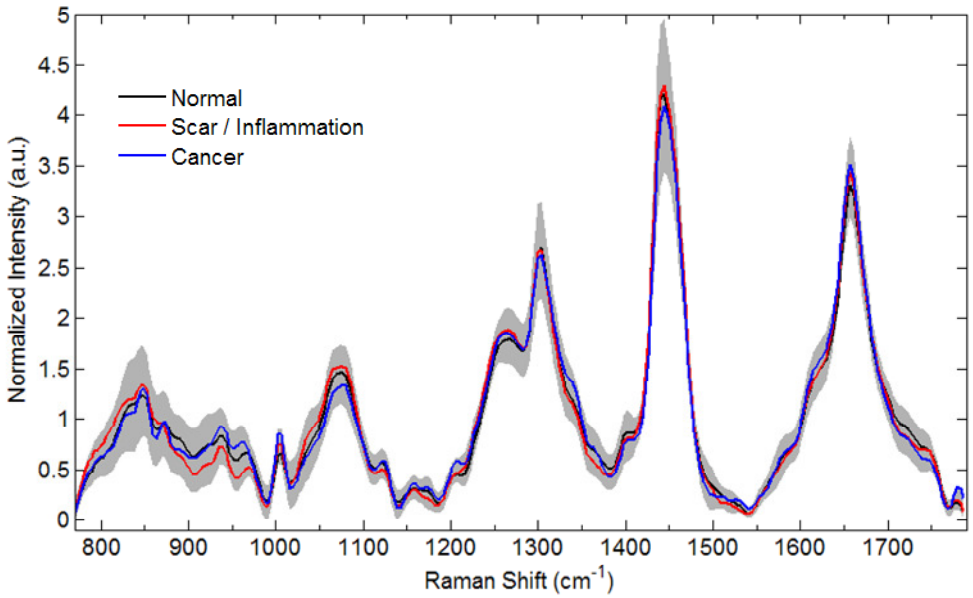

Fig. 2.3: Mean spectra from measured tissue classes. Grey area indicates the 95 % confidence intervals based on calculation of the standard error the normal spectra. Note that all lesion types predominantly lie within the variance bounds of normal skin spectra, making direct classification of spectral differences difficult.

The lack of clear visible distinction between lesion spectral classes is expected because skin is a very heterogeneic tissue, and can have varying epithelial thickness, dermal structure, glandular content, that can contribute as sources of variance in the spectra. This heterogeneity can be accounted for by subtracting the lesion spectra from the normal spectra. The mean difference spectra for cancerous lesions and scar/inflammation are shown in figure 2.4. The grey area indicates the 95% confidence intervals, which are calculated from the variance in normal skin spectra. The plots are shown to provide some indication of what features are likely to contribute to the

classification. The difference spectra for scar/inflammation tissue does not stray outside the confidence intervals in any wavenumber region. The cancer difference spectra, however, are distinctly different at a number of spectral areas. There is a significant increase in the bands from 999 to 1010 cm^{-1}, 1203 – 1215 cm^{-1}, 1639-1647 cm^{-1}, and 1785-1789 cm^{-1}. Although the mean difference spectra for the two lesion types still mostly fall within the variable range of normal skin spectra, there are clearly some features that the classification algorithm may utilize.

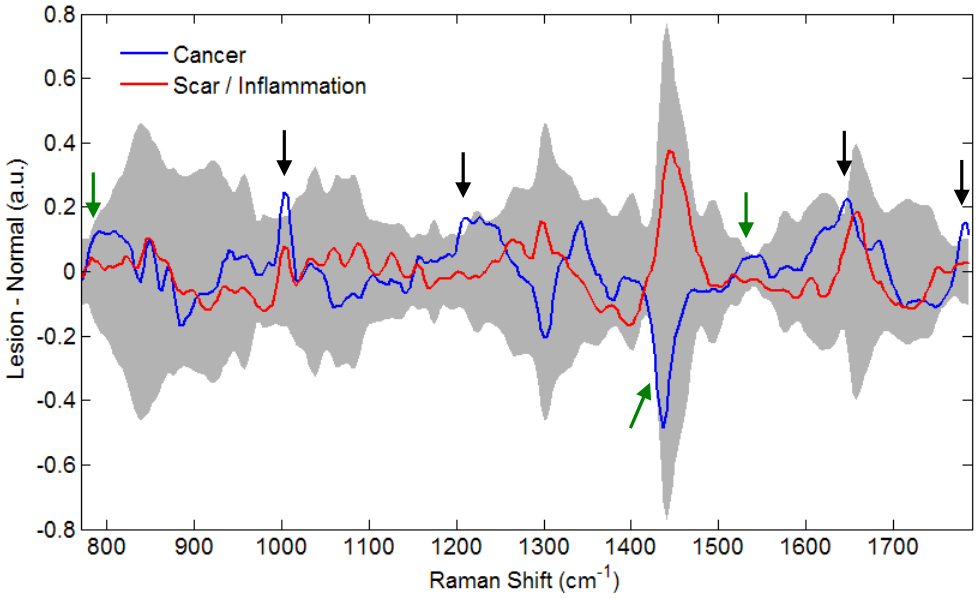

Fig. 2.4: Mean difference (lesion – normal) spectra. Grey area indicates the 95% confidence intervals for normal skin plotted about 0. Black arrows indicate locations where spectra is outside the confidence intervals. Green arrows indicate that are nearly beyond the confidence interval bounds and utilized by SMLR for classification.

The SMLR algorithm generated a sparse set of basis functions to represent the difference spectra and provide optimal classification accuracy using the wavenumber points shown in table 2.1. The results of the leave one patient out cross validation of the learned classification algorithm are shown in table 2.2. The sensitivity and specificity are 78% and 94%, respectively. The overall classification accuracy is 85%. The receiver operating curve is shown in figure 2.5a. The area under the curve is 0.85. Figure 2.5b shows a map of the calculated posterior probabilities of the correct class membership for each sample. A probability of 0.5 was set as the decision threshold. Misclassified

cancerous lesions were; 1.) a 66 year old male with a BCC of the nose, 2.) a 49 year old female with a BCC of the forehead, 3.) an 83 year old female with a BCC of the scalp, and 4.) a 48 year old female with a BCC of the mandible. The lone scar/inflammation lesion that was misclassified was taken from the shoulder of a 61 year old female at a location that was previously SCC.

Wavenumber (cm^{-1})	Significance	Involved Peak Assignment
786	Nearly Significant	PO_2 symmetric stretching (DNA, RNA)
1006	Significant	Slope of Phenylalanine ring breathing peak (DNA, Proteins)
1010	Significant	Slope of Phenylalanine ring breathing peak (DNA, Proteins)
1129		Slope of C-C stretching, *trans peak* (Lipids)
1297		Slope of Amide III peak (Lipids, various proteins)
1391		
1430	Nearly Significant	Slope of CH_x peak (Protiens, Lipids)
1535	Nearly Significant	
1776	Significant	

Table 2.1: Spectral Features Utilized by SMLR classification algorithm. The 2nd column indicates if the feature falls outside the 95% confidence intervals of normal spectra as shown in figure 4. The 3rd column indicates if the data point is involved in any prominent peaks of skin spectra.

	Cancer	**Scar / Inflammation**
Cancer	14	4
Scar / Inflammation	1	15

Table 2.2: Classification Results.

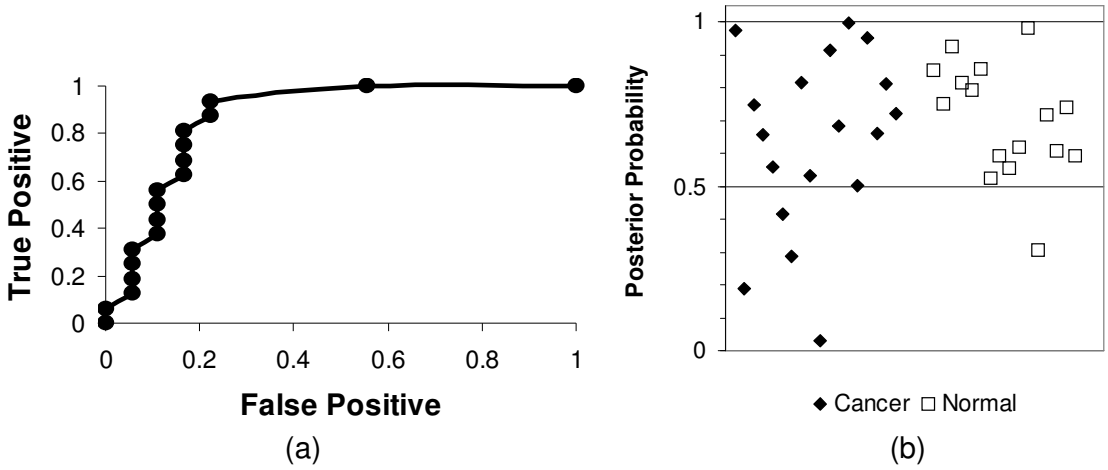

Fig. 2.5: Classification Results. (a) Receiver Operating Curve. Area under the curve = 0.85. (b) is a map of each samples posterior probabilities membership to the correct class. Probability of 0.5 was the decision threshold.

Discussion

The results indicate the potential of fiber probe based Raman spectroscopy for *in vivo* skin cancer diagnosis. There is a significant difference in the band from 999 to 1010 cm^{-1}, which corresponds to the phenylalanine peak and indicates increased contribution from proteins/nuclei. This band is also identified by the SMLR learning algorithm as containing 2 of the 9 points used for classification, further indicating its diagnostic relevance. Although the spectral features at 786 and 1430 cm^{-1} do not lie beyond the 95% confidence intervals of normal spectral variance, they are near the boundary and identified by SMLR as diagnostically relevant. The 786 cm^{-1} spectral feature appears as the shoulder of the larger 849 cm^{-1} protein peak, however in the difference spectrum is more distinct. Njissen et. al. have observed this peak in previous work identifying BCC with Raman spectroscopy and attributed it to DNA and RNA[10], making it a likely band to be identified for diagnostic relevance. The 1430 cm^{-1} feature can be indicative of the width of the CH_2 peak at 1444 cm^{-1}. This region has been previously implicated as diagnostically relevant in skin cancers[10, 15], however the fact that it contains contributions from a wide number of lipid and protein subgroups makes commenting on the biological relevance difficult. On the whole these spectral features identified by the SMLR machine

learning classifier point towards increased protein, DNA, and RNA content driving classification performance.

The 1203 – 1215 cm^{-1} and 1639-1647 cm^{-1} bands, on the other hand, contain significant differences, however, they are not identified as critical in classification. This does not necessarily indicate these bands will not be relevant in future classification algorithms that would likely seek to classify between cancer subclasses. The SMLR algorithm is designed to seek out the sparsest basis functions possible for classification performance, and it is possible these features may have been redundant to other features identified.

Overall, the diagnostic accuracy achieved from the data in this study is not up to the standards reported in the Raman skin cancer literature. The lone reported *in vivo* study by Lieber et al. achieved an overall classification accuracy of 95% (n = 21) in which 4-way classification of normal skin, BCC, SCC, and inflammation/scar was performed. A number of *in vitro* studies of non-melanoma skin cancer detection with Raman spectroscopy have all demonstrated overall classification accuracies in excess of 90% [10, 12, 16]. The critical factor all these studies utilized was a confocal collection geometry that allowed isolation of Raman scattered light originating in the dermis from the epidermis. Lieber et. al. were able to achieve high classification accuracy by summing spectra from depths ranging from the surface down through 100 μm, implying that a confocal collection geometry was not necessary, however this sum is evenly weighted across all depths. The fiber-optic probe utilized here is bound to collect a spectrum that is surface biased for two reasons. The first is the beam-steered angle polish of the collection fibers will observe light scattered from the tissue surface directly infront of the probe preferentially to the underlying dermis. A more appropriate probe to use for a skin cancer detection study may be one without beam steered collection fibers that collect from a wider range of depths. Nevertheless, these results seem to warrant a direct side-by-side test of the classification accuracy of a fiber-probe based Raman system with a confocal collection system to determine which performs superior classification.

Alternatively, the inferior classification accuracy seen in the current study may be strictly due to an insufficient sample size. The appropriate manner in which sample size should be calculated is with respect to the statistical test being performed for

classification. If the test being performed is a simple t-test of the 1003 cm^{-1} peak, the appropriate sample size for this study is n = 56 (sample mean and standard deviation calculated from data in this study, $\alpha = 0.05$, power = .95). With 34 patients currently enrolled, and an α of 0.05, the power of the study (probability of correctly rejecting the hypothesis that the mean values of the phenylalanine peaks are the same) can be calculated as 0.8[23]. Clearly, this approach is not appropriate given the approach we are taking for classification is SMLR. Ultimately, the appropriate sample size for the SMLR test needs to be performed. However, given the fact that the SMLR test is likely more sensitive, these figures should provide a conservative estimation for the necessary enrollment figures.

Previous work using fiber-probe based Raman spectroscopy in the cervix has identified the technique's sensitivity to biological phenomena that are not readily visible in histology[8]. Hormonal factors related to a woman's ovulatory status were determined to significantly affect the classification performance of a Bayesian classifier similar to the SMLR algorithm used in this study. Based on these results, it is possible that stratifying the data appropriately may assist classification performance. Analysis of available data related to the patients enrolled in this study (age, gender, lesion location) did not bring any obvious patterns to light. The misclassified lesions were from male and female patients of a wide range of ages, and from a wide range of locations, none of which were exclusive to misclassification. In the case of skin cancer, however, one confounding factor worth investigating is the patient's organ transplant history. It is known that organ transplant recipients have greatly increased (approx 65-fold) incidence of skin cancer due to their immuno-compromised status[24]. In Vanderbilt Mohs Surgery, where a majority of the patients for this study were recruited, roughly 1/3 of the patients are organ transplant recipients. It is possible that stratifying the patients according to this patient history factor may improve classification performance.

Ultimately, the sources of variability in normal skin are many, and the appropriate application of a technique with the biochemical sensitivity of Raman spectroscopy requires further investigation. Here, we have demonstrated that fiber probe based Raman spectroscopy shows promise for non-invasive detection of cancer from non-cancerous lesions. In contrast to a previous *in vivo* study utilizing a confocal collection geometry,

the shorter spectral integration times and the physical ease of handling a fiber-probe are definite advantages for practical clinical implementation. The future directions for this work include recruiting more patients and assessing the patient history for possible sources of variation.

Acknowledgements

The authors wish to acknowledge the assistance of Dr. Thomas Stasko and Dr. Anna Clayton for their assistance in performing clinical measurements, and the Vanderbilt University Skin Disease Research Center (NIH 5P30 AR041943) for their assistance in preparing the slides.

References

1. "Cancer Facts and Figures: 2009" (American Cancer Society, 2009), retrieved http://www.cancer.org/downloads/STT/500809web.pdf.
2. H. G. Welch, S. Woloshin, and L. M. Schwartz, "Skin biopsy rates and incidence of melanoma: population based ecological study," Bmj **331**(7515), 481 (2005).
3. M. Mogensen, L. Thrane, T. M. Jorgensen, P. E. Andersen, and G. B. E. Jemec, "OCT imaging of skin cancer and other dermatological diseases," Journal of Biophotonics **2**(6-7), 442-451 (2009).
4. M. Rajadhyaksha, G. Menaker, T. Flotte, P. J. Dwyer, and S. Gonzalez, "Confocal examination of nonmelanoma cancers in thick skin excisions to potentially guide mohs micrographic surgery without frozen histopathology," J Invest Dermatol **117**(5), 1137-1143 (2001).
5. L. Brancaleon, A. J. Durkin, J. H. Tu, G. Menaker, J. D. Fallon, and N. Kollias, "In vivo fluorescence spectroscopy of nonmelanoma skin cancer," Photochemistry and Photobiology **73**(2), 178-183 (2001).
6. R. Eichhorn, G. Wessler, M. Scholz, D. Leupold, G. Stankovic, S. Buder, M. Stucker, and K. Hoffmann, "Early diagnosis of melanotic melanoma based on laser-induced melanin fluorescence," J Biomed Opt **14**(3), 034033 (2009).
7. S. K. Majumder, M. D. Keller, M. C. Kelley, F. I. Boulos, and A. Mahadevan-Jansen, "Comparison of autofluorescence, diffuse reflectance, and Raman spectroscopy for breast tissue discrimination," Journal of Biomedical Optics (in press)(2008).
8. E. M. Kanter, E. Vargis, S. Majumder, M. D. Keller, E. Woeste, G. G. Rao, and A. Mahadevan-Jansen, "Application of Raman spectroscopy for cervical dysplasia diagnosis," J Biophotonics **2**(1-2), 81-90 (2009).
9. M. G. Shim, L. M. Song, N. E. Marcon, and B. C. Wilson, "In vivo near-infrared Raman spectroscopy: demonstration of feasibility during clinical gastrointestinal endoscopy," Photochem Photobiol **72**(1), 146-150 (2000).
10. A. Nijssen, T. C. B. Schut, F. Heule, P. J. Caspers, D. P. Hayes, M. H. A. Neumann, and G. J. Puppels, "Discriminating basal cell carcinoma from its surrounding tissue by Raman spectroscopy," Journal of Investigative Dermatology **119**(1), 64-69 (2002).
11. C. A. Lieber, S. K. Majumder, D. Billheimer, D. L. Ellis, and A. Mahadevan-Jansen, "Raman microspectroscopy for skin cancer detection in vitro," J Biomed Opt **13**(2), 024013 (2008).
12. S. Sigurdsson, P. A. Philipsen, L. K. Hansen, J. Larsen, M. Gniadecka, and H. C. Wulf, "Detection of skin cancer by classification of Raman spectra," IEEE Trans Biomed Eng **51**(10), 1784-1793 (2004).
13. M. Gniadecka, P. A. Philipsen, S. Sigurdsson, S. Wessel, O. F. Nielsen, D. H. Christensen, J. Hercogova, K. Rossen, H. K. Thomsen, R. Gniadecki, L. K. Hansen, and H. C. Wulf, "Melanoma diagnosis by Raman spectroscopy and

neural networks: structure alterations in proteins and lipids in intact cancer tissue," J Invest Dermatol **122**(2), 443-449 (2004).
14. M. A. Short, H. Lui, D. McLean, H. Zeng, A. Alajlan, and X. K. Chen, "Changes in nuclei and peritumoral collagen within nodular basal cell carcinomas via confocal micro-Raman spectroscopy," J Biomed Opt **11**(3), 34004 (2006).
15. C. A. Lieber, S. K. Majumder, D. L. Ellis, D. D. Billheimer, and A. Mahadevan-Jansen, "In vivo nonmelanoma skin cancer diagnosis using Raman microspectroscopy," Lasers Surg Med **40**(7), 461-467 (2008).
16. C. A. Lieber, S. K. Majumder, D. Billheimer, D. L. Ellis, and A. Mahadevan-Jansen, "Raman Microspectroscopy for Skin Cancer Detection In Vitro," Journal of Biomedical Optics **In Press**(2007).
17. A. Nijssen, K. Maquelin, L. F. Santos, P. J. Caspers, T. C. Bakker Schut, J. C. den Hollander, M. H. Neumann, and G. J. Puppels, "Discriminating basal cell carcinoma from perilesional skin using high wave-number Raman spectroscopy," J Biomed Opt **12**(3), 034004 (2007).
18. C. A. Lieber and A. Mahadevan-Jansen, "Automated method for subtraction of fluorescence from biological Raman spectra," Applied Spectroscopy **57**(11), 1363-1367 (2003).
19. B. Krishnapuram, L. Carin, M. A. T. Figueiredo, and A. J. Hartemink, "Sparse multinomial logistic regression: Fast algorithms and generalization bounds," Ieee Transactions on Pattern Analysis and Machine Intelligence **27**(6), 957-968 (2005).
20. A. Mahadevan-Jansen and R. Richards-Kortum, "Raman Spectrscopy for the Detection of Cancers and Precancers," Journal of Biomedical Optics **1**(1), 31-70 (1996).
21. M. Gniadecka, H. C. Wulf, N. N. Mortensen, O. F. Nielsen, and D. H. Christensen, "Diagnosis of basal cell carcinoma by Raman spectroscopy," Journal of Raman Spectroscopy **28**(2-3), 125-129 (1997).
22. N. Stone, C. Kendall, J. Smith, P. Crow, and H. Barr, "Raman spectroscopy for identification of epithelial cancers," Faraday Discuss **126**, 141-157; discussion 169-183 (2004).
23. W. D. Dupont and W. D. Plummer, Jr., "Power and sample size calculations. A review and computer program," Control Clin Trials **11**(2), 116-128 (1990).
24. B. T. Kovach and T. Stasko, "Skin cancer after transplantation," Transplantation Reviews **23**(3), 178-189 (2009).

CHAPTER III

MANUSCRIPT 2

A Combined Raman Spectroscopy – Optical Coherence Tomography Device for Tissue Characterization

Chetan A. Patil[1], Nienke Bosschaart[2,3], Matthew D. Keller[1], Ton G. van Leeuwen[2,3], and Anita Mahadevan-Jansen[1]

[1] Department of Biomedical Engineering, Vanderbilt University, Nashville TN, USA
[2] Biophysical Engineering Group, Faculty of Science and Technology, University of Twente, Enschede The Netherlands
[3] Laser Center, Academic Medical Center, University of Amsterdam, Amsterdam, The Netherlands

Published in *Optics Letters* **33** (10), 1135-1137, 2008

Abstract

We report a dual-modal device capable of sequential acquisition of Raman Spectroscopy (RS) and optical coherence tomography (OCT) along a common optical axis. The device enhances application of both RS and OCT by precisely guiding RS acquisition with OCT images while also compensating for the lack of molecular specificity in OCT with the biochemical specificity of RS. Here, we characterize the system performance and demonstrate the capability to identify structurally ambiguous features within an OCT image with RS in a scattering phantom, guide acquisition of RS from a localized malignancy in *ex vivo* breast tissue, and perform *in vivo* tissue analysis of a scab.

Letter

Optical imaging and spectroscopy have both been used to detect disease based on analysis of tissue microstructure and biochemical composition, yet neither method has demonstrated the spatial sensitivity and rapid data acquisition needed for screening in combination with the high specificity required for reliable multi-class discrimination. Spectroscopy excels at detecting molecular markers of disease with high specificity, while imaging excels in detecting tissue microstructure with high sensitivity. In particular, near infrared (NIR) Raman spectroscopy (RS) has been used for *in vivo* detection of cancers in various organs [1]. RS is sensitive to vibrational modes in tissue and produces fingerprint spectra characteristic of specific molecules and their environments, thus realizing unparalleled molecular specificity. A recent comparison of Raman, fluorescence, and diffuse reflectance spectroscopy for breast cancer detection demonstrated the superior specificity of RS in classifying disease [2]. The weak nature of RS requires integration times of 3-30 seconds, limiting the technique to point measurements and motivating the need for image guidance to improve sampling accuracy. A combined confocal microscopy (CM) – confocal RS device was developed to guide RS acquisition with images of tissue microstructure [3], but confocal imaging depth in epithelial tissues is limited to ≈ 250 μm and transverse field-of-view (FOV) is limited to ≈ 500 μm. Combining the molecular specificity of RS with an imaging method that has increased depth and larger FOV will yield a valuable tool for early detection of disease.

Optical coherence tomography (OCT) can image over larger transverse areas of tissue (> 5mm) with micron scale resolution, real-time speed, and sensitivity to microstructural features of disease [4]. The primary limitation of OCT is that the images are reflectivity maps of sample morphology but lack biochemical specificity. For instance, differentiating between a benign pigmented skin lesion and superficial spreading melanoma can be difficult due to similar irregular morphology of the epidermis in both cases [5]. Just as RS would benefit from image guidance, OCT would benefit from biochemical specificity for classifying irregular structures. A number of intrinsic and extrinsic approaches to add molecular contrast directly to OCT are being evaluated by many groups [6]. One of these is an OCT system capable of detecting coherent anti-stokes RS (CARS) [7]; however, CARS requires a much costlier laser source than NIR RS and currently has limited clinical translatability. Another approach is to combine complementary modalities of molecular contrast with OCT such as an OCT-fluorescence device [8]. However, the higher specificity of RS makes it a better choice for detecting disease. The complementary natures of RS and OCT were demonstrated in a study where two separate instruments were used to analyze the microstructural and biochemical features of dental carries [9]. This work suggests the benefit of a single device capable of RS and OCT for complete tissue characterization.

In this letter, we present a dual-modal RS-OCT device capable of sequentially acquiring NIR RS and OCT data through common sampling optics, while keeping the source and detection arms separate. This system allows each technique to compensate for the limitations of the other; OCT imaging can be performed in real-time and used to guide the measurement of a Raman spectrum from an area of 600 μm in depth by 75 μm across along the central axis of the OCT image. Raman spectra can be acquired to specifically characterize the biochemical fingerprint of ambiguous structures within an OCT image. Conversely, OCT can rapidly perform microstructural imaging of large areas and precisely guide the acquisition of RS from tissue. The capabilities of RS-OCT are demonstrated in scattering phantoms, *ex vivo* tissue, and *in vivo* skin.

The instrument setup is shown in figure 3.1. A 1310 nm ($\Delta\lambda_{FWHM}$ = 60 nm) OCT source is coupled into a fiber Michelson interferometer with a circulator in the source arm to enable balanced detection [10]. A 50/50 fiber coupler splits the light into the reference arm [11], and the sample arm, where an XY galvanometer pair scans the light across an achromatic doublet objective lens (f=35.0 mm, NA = 0.36) to generate B-scans. The detected interference signal is

band-pass filtered, amplified in hardware, and digitized at 1.25 Msamples/s. Demodulation and logarithmic compression are performed in software prior to live display of the grayscale image.

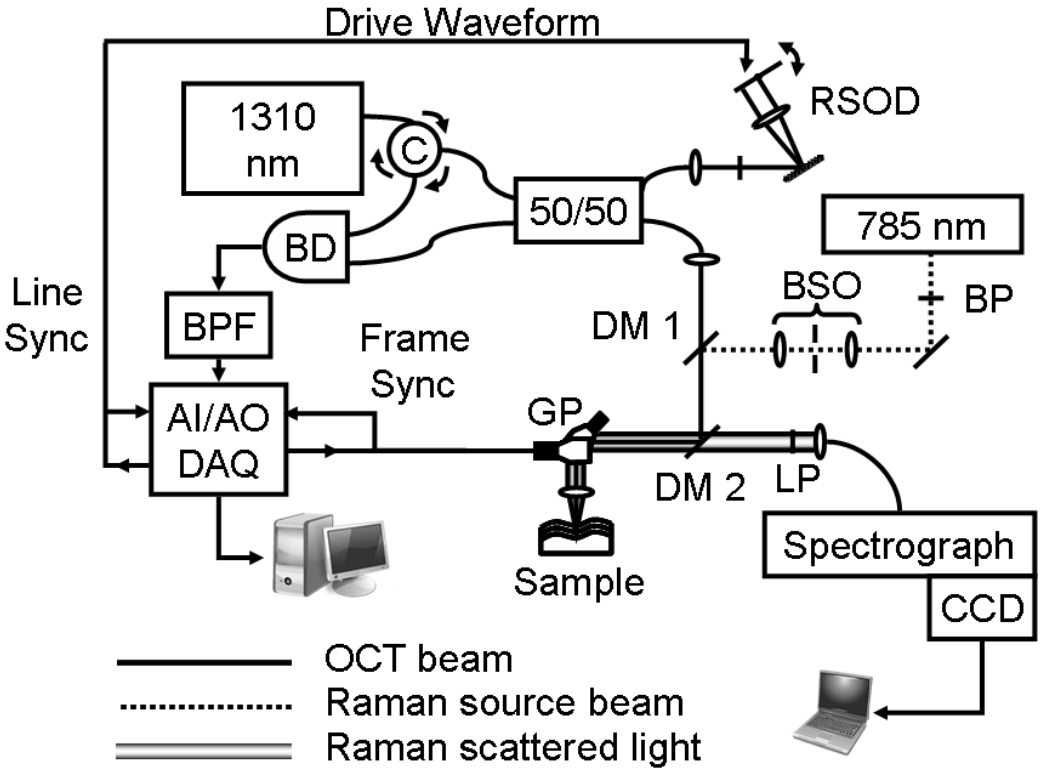

Fig. 3.1 Diagram of RS-OCT system. C–Circulator, RSOD-Rapid Scanning Optical Delay, BP–785 Band Pass, BSO–Beam Shaping Optics, DM1–Dichroic Mirror at 990 nm, DM2–Dichroic Mirror at 800-950 nm, LP–Long Pass at 808 nm, GP–Galvanometer Pair, BD–Balanced Detector, BPF–electronic Band Pass Filter, AI/AO DAQ–Analog Input/Output Data Acquisition.

The Raman source is a 785 nm diode laser that is directed through a magnifying lens pair that spatially filters and shapes the beam to produce a Gaussian profile. The OCT and Raman incident beams are co-aligned by a dichroic mirror (DM1), and then redirected to the sample by a second dichroic mirror (DM2) that reflects both source beams while transmitting the Raman stokes band. The XY galvanometers are fixed and RS is performed only along the central axis of the objective lens. The Raman laser power at the sample is fixed at 40 mW. For Raman detection, a long-pass filter reduces Rayleigh scatter and an achromat (f=19.0 mm, NA=0.33) couples the Raman scatter into a 100 μm core low-OH fiber which acts as a pinhole. An f/1.8 holographic imaging spectrograph with an integrated 785 nm notch filter disperses the light onto a back-illuminated, deep depletion thermo-electrically cooled CCD camera. The spectral

resolution of the system is 7.7 cm^{-1}. System calibration and processing are performed using a quartz tungsten halogen lamp, neon-argon lamp and Raman standards (described in [12]).

All OCT images were acquired with a line rate of 500 Hz and scan range of 2.4 mm at 1 frame/s. The OCT signal-to-noise (SNR) is 125 dB with a mirror as the sample. The measured axial and lateral resolutions are 21 μm in air (15 μm in tissue) by 25 μm, respectively. The average Raman SNR of an RS standard such as naphthalene was found to be 57 dB with 1 second integration. The RS point-spread function (PSF) was found to be 600 μm axially and 75 μm laterally at FWHM. This was obtained axially by measuring the 1308 cm^{-1} peak intensity of a 12.5 μm layer of polyethylene as a function of its axial position in the OCT image and transversely by measuring the falloff in Raman intensity while translating across a clean edge of the polyethylene placed at the focus of the axial PSF. To verify the co-alignment of the Raman and OCT beams, a gelatin phantom was placed at multiple depths in the OCT image, and a dehydrated indentation in the surface of the sample was created with the Raman laser at high power. An OCT image of the indentation verified the transverse position of the Raman beam. A vertical targeting line at this position was overlaid onto the OCT image to guide positioning of the area of interest for RS, and horizontal targeting lines corresponding to the FWHM of the axial PSF were overlaid for axial alignment (see fig. 3.2). All samples were placed on a translation stage and Raman spectra were obtained by positioning the area of interest in the sample within all three targeting lines. Figures 3.2-3.4 each display an overview OCT image of the sample; the vertical lines in these figures identify the transverse position where Raman spectra were acquired. The horizontal lines that guide the depth of RS acquisition are not shown.

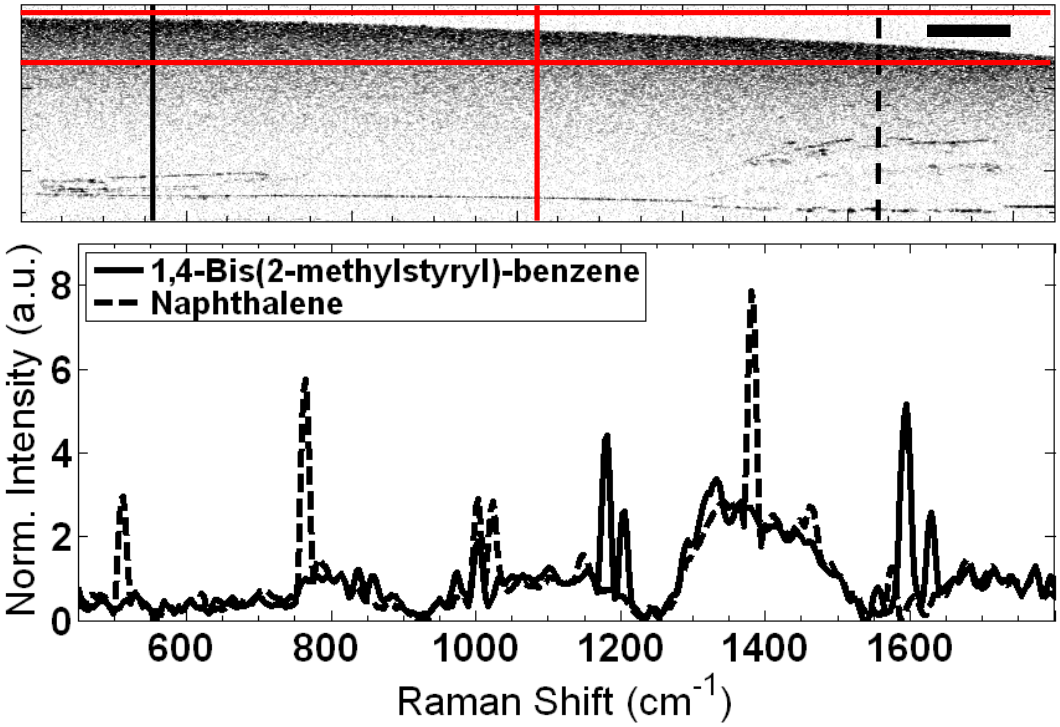

Fig. 3.2: RS-OCT from a scattering gel with BMSB (solid line) and naphthalene (dashed line) showing similarities in OCT but biochemical differences in RS. Scale bar is 0.8 mm. An example of the red Raman targeting lines are shown. Scattering in the sample is due to 1μm polystyrene microspheres, whose spectral contribution can be seen from the peak at 1001 cm^{-1}.

A scattering gelatin phantom containing two Raman active crystals (naphthalene and 1,4-Bis(2-methylstyryl)-benzene (BMSB)) with similar optical and structural properties was used to demonstrate the ability of RS to aid OCT (fig. 3.2). Although the two crystals appear similar in OCT, RS of the left crystal contains the BSMB peaks at 1181, 1206, 1594, and 1629 cm,$^{-1}$ while the right crystal shows naphthalene peaks at 513, 765, 1024, 1381, and 1577 cm^{-1}.

The ability of OCT to screen tissues and guide RS was demonstrated with an *ex vivo* malignant human breast tissue sample (Fig. 3.3). The tissue was scanned with OCT to locate highly scattering abnormal regions, one of which was surrounded by normal fatty tissue. The OCT display was used to guide collection of Raman spectra from both the abnormal and normal sites. The spectral lineshapes are characteristic of reported normal and malignant breast tissues [2], with the normal spectrum dominated by lipid signatures and the malignant spectrum demonstrating greater DNA and protein content, especially collagen. The size of the malignant region in Fig. 3.3 was only ≈ 500 μm, yet OCT allowed sample localization and confirmed that spectra were acquired from the correct transverse position.

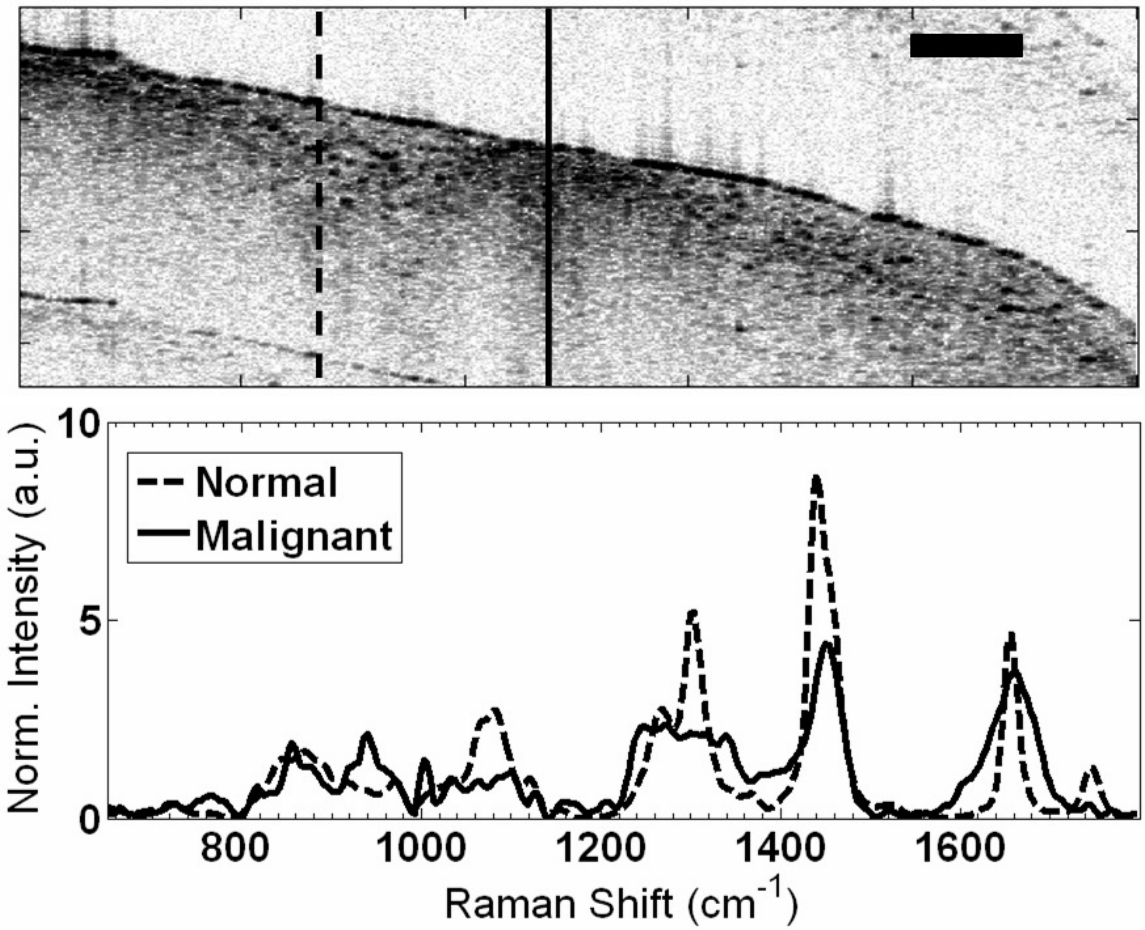

Fig. 3.3: RS-OCT of normal (dashed line) and malignant (solid line) *ex vivo* breast sample where structural anomaly in OCT is spectrally characterized by pronounced protein peaks indicative of malignancy while normal breast shows a strong lipid signature. Scale bar is 500 μm.

The applicability of RS-OCT for *in vivo* tissue characterization was demonstrated by evaluating a healing wound on the finger of a volunteer (fig. 3.4). The scab is visible in OCT as a hyper-reflective region in the center of the image. Immediately adjacent to the scab is a region with epidermal disruption that is likely due to remodeling. The finger was positioned with OCT such that RS could be acquired from the center of the scab and the peripheral wound. Three spectra from each position were averaged, yielding an *in vivo* SNR of 33 dB at the 1440 cm^{-1} peak. Subtle differences in the spectral line-shapes were observed, including the 856 and 940 cm^{-1} collagen peaks in the scab spectrum.

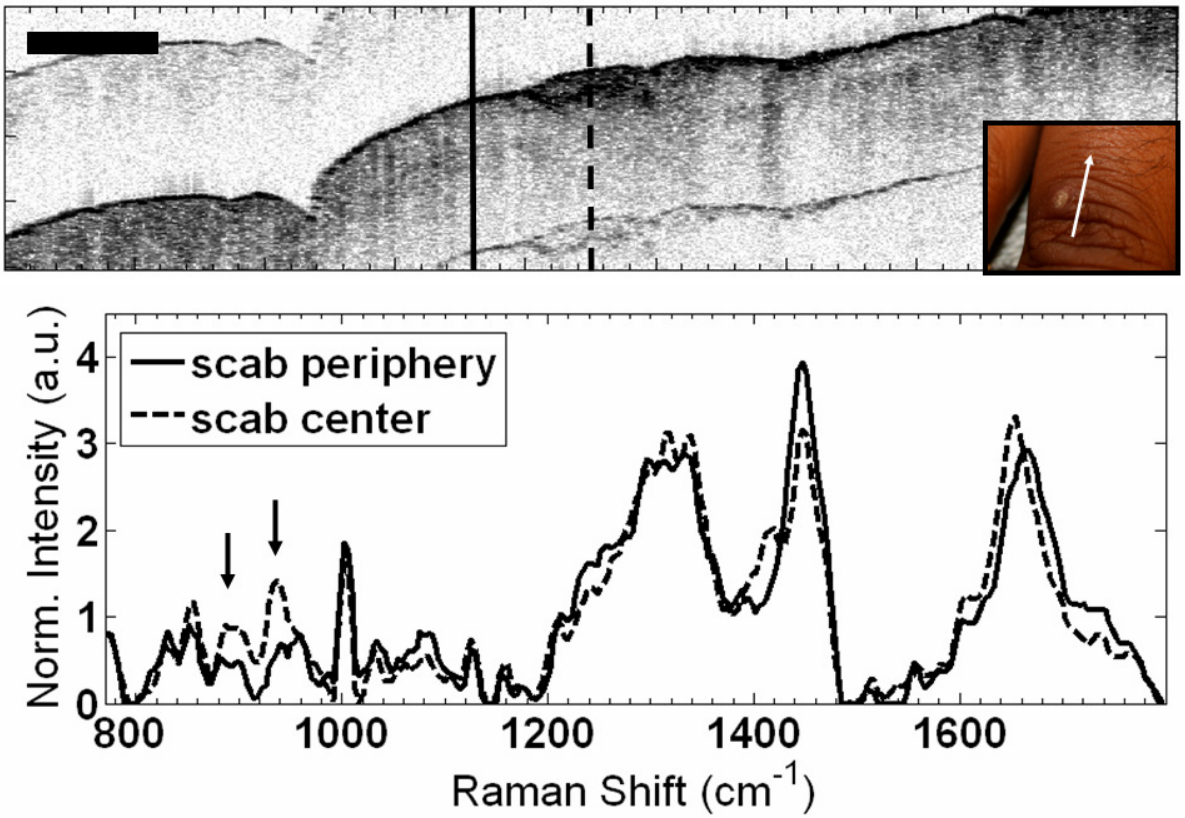

Fig. 3.4 *In vivo* RS-OCT of a scab (dashed line) and peripheral wound (solid line) on the back of the finger. Scale Bar is 1mm. Inset picture shows wound and direction of scan. Arrows identify increased collagen peaks in scab spectrum.

This Letter presents the 1st combined NIR RS-OCT device that demonstrates the potential advantages of morphological and biochemical evaluation of tissues. The goal of our work is the application of RS-OCT for diagnosis of epithelial cancers; however, thorough tissue characterization with RS-OCT could benefit other applications. The Raman collection throughput can be improved with filter and dichroic mirror redesign, reducing *in vivo* integration times to < 10 seconds. The axial resolution of RS could be improved to approach that of OCT with true confocal detection, but the sharp focus of the incident beam in such a system would degrade OCT transverse resolution away from the focus. Using a common wavelength for RS and OCT would further simplify the RS-OCT system, but attempting RS at wavelengths closer to 1310 would result in weaker scattering and thus longer integration times. Alternatively, OCT can be performed in the 800 nm band, but increased scattering would reduce imaging depth. This system therefore presents a compromise for optimal performance from both modalities.

Acknowledgements

The authors acknowledge contributions from E. Duco Jansen of Vanderbilt University and the Biomedical Technology Institute of the University of Twente.

References

1. A. Mahadevan-Jansen, "Raman Spectroscopy: From Benchtop to Bedside," in *Biomedical Photonics Handbook*, T. Vo Dinh, Editor.(CRC Press 2003) p. 30:1-27.
2. S. K. Majumder, M. D. Keller, M. C. Kelley, F. I. Boulos, and A. Mahadevan-Jansen, J Biomed Opt (2008).
3. P. J. Caspers, G. W. Lucassen, and G. J. Puppels, Biophys J **85,** 572-580 (2003).
4. J. G. Fujimoto, M. E. Brezinski, G. J. Tearney, S. A. Boppart, B. Bouma, M. R. Hee, J. F. Southern, and E. A. Swanson, Nat Med **1,** 970-972 (1995).
5. T. Gambichler, P. Regeniter, F. G. Bechara, A. Orlikov, R. Vasa, G. Moussa, M. Stucker, P. Altmeyer, and K. Hoffmann, J Am Acad Dermatol **57,** 629-637 (2007).
6. C. H. Yang, Photochemistry and Photobiology **81,** 215-237 (2005).
7. C. Vinegoni, J. S. Bredfeldt, D. L. Marks, and S. A. Boppart, Opt Express **12,** 331-341 (2004).
8. A. R. Tumlinson, L. P. Hariri, U. Utzinger, and J. K. Barton, Appl Opt **43,** 113-121 (2004).
9. A. C. Ko, L. P. Choo-Smith, M. Hewko, L. Leonardi, M. G. Sowa, C. C. Dong, P. Williams, and B. Cleghorn, J Biomed Opt **10,** 031118 (2005).
10. A. M. Rollins and J. A. Izatt, Opt Lett **24,** 1484-1486 (1999).
11. A. M. Rollins, M. D. Kulkarni, S. Yazdanfar, R. Ung-arunyawee, and J. A. Izatt, Opt Express **3,** 219-229 (1998).
12. A. Robichaux-Viehoever, E. M. Kanter, H. Shappell, D. Billheimer, H. Jones III, and A. Mahadevan-Jansen, Appl Spectrosc **61,** 986-993 (2007).

CHAPTER IV

MANUSCRIPT 3

Common Detector Raman Spectroscopy-Optical Coherence Tomography of the Rodent Retina

Chetan A. Patil[1], Jeroen Kolkman[2], Dirk Faber[2], John S. Penn[3], Ton G. van Leeuwen[2], and Anita Mahadevan Jansen[1]

[1]Department of Biomedical Engineering, Vanderbilt University, Nashville TN, USA
[2]Laser Center, Academic Medical Center, University of Amsterdam, Amsterdam, The Netherlands
[3]Vanderbilt Eye Institute, Vanderbilt University School of Medicine, Nashville, TN, USA

Prepared for submission to *Journal of Biomedical Optics*

Abstract

Raman spectroscopy (RS) and Optical Coherence Tomography (OCT) are powerful tools for optical analysis of tissues with complimentary strengths. OCT excels and visualizing tissue microstructure while RS can relay tissue biochemical composition. The strengths and limitations of RS and OCT complimentary, and thus their combination offers the potential to enhance both data sets. Previous implementations of RS-OCT have employed separate system backbones for OCT and RS. Here, we present the design and application of a common detector combined RS-OCT instrument for evaluating the morphological and biochemical differences in a rat model for oxygen induced retinopathy. Rat pups that have undergone a variable oxygen treatment are compared to rats raised in room air. Images and spectra collected at an age of 26 days postnatal demonstrate differences in the thickness of the inner and outer nuclear layers, with OCT as well differences in the Raman spectral bands attributed to DNA and RNA nucleotides, amino acids, and proteins.

Introduction

Near-Infrared Raman spectroscopy (RS) is a powerful optical technique capable of detecting subtle biochemical differences between tissues. The spectral shift undergone by in-elastically scattered photons carries information related to the vibrational bond structure of the molecules within the sample. This high level of specificity is basis for which RS has demonstrated the ability to detect cancerous and pre-cancerous tissues[1] and analyze the chemical composition of arterial plaques[2]. Despite the strength of RS for molecular characterization, the inherently week nature of in-elastic scattering limits the ability to relay information of tissue structure in a reasonable timeframe.

In order to augment the biochemical sensitivity of RS with information related to tissue morphology, instruments combing confocal reflectance microscopy (CRM)[3], wide-field tri-modal imaging (WTM)[4], and optical coherence tomography (OCT)[5, 6] with RS have all recently been reported. The ability of the RS-CRM device to visualize cellular morphology can be invaluable for disease diagnosis; however the fine detail comes at the

expense of penetration depth and field of view. The RS-WTM instrument demonstrates how wide field multi-modal imaging can improve the spatial precision with which Raman spectra are acquired. While the imaging technique selected for each device is certainly motivated by the intended application, optical coherence tomography (OCT) can be considered advantageous due to its ability to perform high speed, wide-field of view imaging with micron scale resolution. As a result, two instruments combining RS and OCT have recently been reported to date. The first is demonstrated in highly scattering tissues such as the breast and skin, and performs RS at 785 nm and OCT at 1310 nm with a time-domain detection scheme[5]. The second performs RS at 633 nm and OCT at 855 nm using spectral domain detection[6] to evaluate the retina. Both systems are implemented using independent RS and OCT system backbones while being integrated at the sample arm. Dual-modal combined RS-OCT instrumentation can be further simplified, however, because both methods are capable of utilizing a spectrograph and CCD in their respective detection arms[7, 8]. Until recently, the speed and noise performance of CCD detectors was insufficient to perform high sensitivity detection of the OCT interference signal in the spectral domain[9]. If designed appropriately, however, it could be possible to realize an RS-OCT system using a common spectrograph and camera for detection.

Non-invasive analysis of the retina is the most prominent application of OCT in clinical practice. The ability to clearly visualize retinal structure has allowed clinicians to better assess the pathological progression of diseases such as age –related macular degeneration, characterize structural defects such as macular holes, and improve treatment outcomes with early disease detection[10]. Recently, the utility of OCT as research using rodent models of retinal pathology has been explored, and found to serve as a useful biomarker for tumor progression in a rat model of retinoblastoma[11] and retinal degeneration in a transgenic mouse model[12]. Such work would be well complimented by Raman studies, which are capable of identifying the molecular progression of disease. For example, recent work has demonstrated the sensitivity of RS to advanced glycation endproducts, molecules that are widely believed to play an important role in the ill-defined pathogenesis of age-related macular degeneration[13]. Thus, the development of a combined RS-OCT instrument holds the potential to provide the unique tool for the

assessment of both the biochemical characteristics of retinal disease and the retinal structure with a single instrument.

Materials and Methods

Here, we present a combined RS-OCT system utilizing a common detector and demonstrate a potential application in evaluating the rodent retina. NIR Raman spectroscopy requires high sensitivity detection due to the inherently weak nature of Raman scattering. Cooled, back illuminated, deep-depletion CCD arrays with exceptionally low noise performance are necessary, along with spectrometers incorporating high throughput optics, and efficient gratings. This detection configuration can be adapted to perform spectral domain detection of the OCT signal, given the appropriate selection of the Raman and OCT sources and spectrograph dispersion.

Fig 4.1a depicts the illumination of the detector. A wavelength stabilized external cavity 785 nm diode laser (Sacher) was selected as the Raman source because the resulting biological fingerprint band of 815 – 930 nm (500–2000 cm^{-1}) best overlaps the range where OCT sources are available, along with the ready availability of high quality optics and filters for Raman detection. The selected OCT source (Exalos) is centered at 850 nm with a 3-dB bandwidth of 40 nm and a full spectral width ranging from approximately 800-900 nm. An f/1.8 imaging spectrograph with a 785 nm Raman holographic transmission grating (Kaiser Optical Systems) is paired with a back illuminated, deep-depletion, thermo-electrically cooled 1024x256 CCD camera (Andor Technology, full well capacity = 186,000 e^-/pixel) to perform detection of both signals. The spectrograph is configured to cover the wavelength range of 780 – 920 nm, which spans the full bandwidth of the OCT source and also largely covers the Raman fingerprint region. Separate 100 μm multimode and 6 μm single fibers couple the Raman and OCT signals, respectively, to the spectrometer. The spectral resolution is 0.123 nm for OCT, and 7 cm^{-1} for Raman. The resulting unaliased depth range of each OCT line-scan is 1.27 mm, which is sufficient for imaging the rodent retina. Calibration of the spectrograph is performed with the atomic emission lines of a Neon-Argon lamp.

(a)

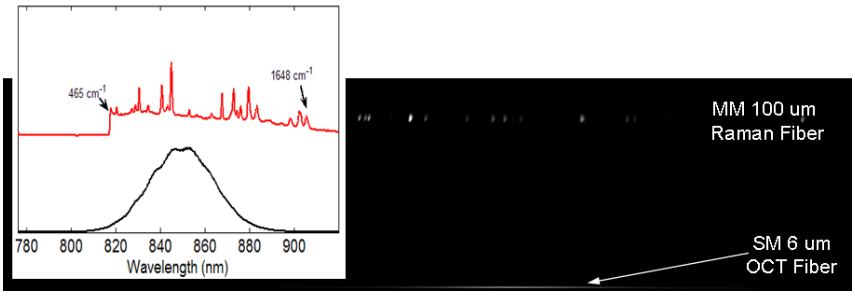

(b)

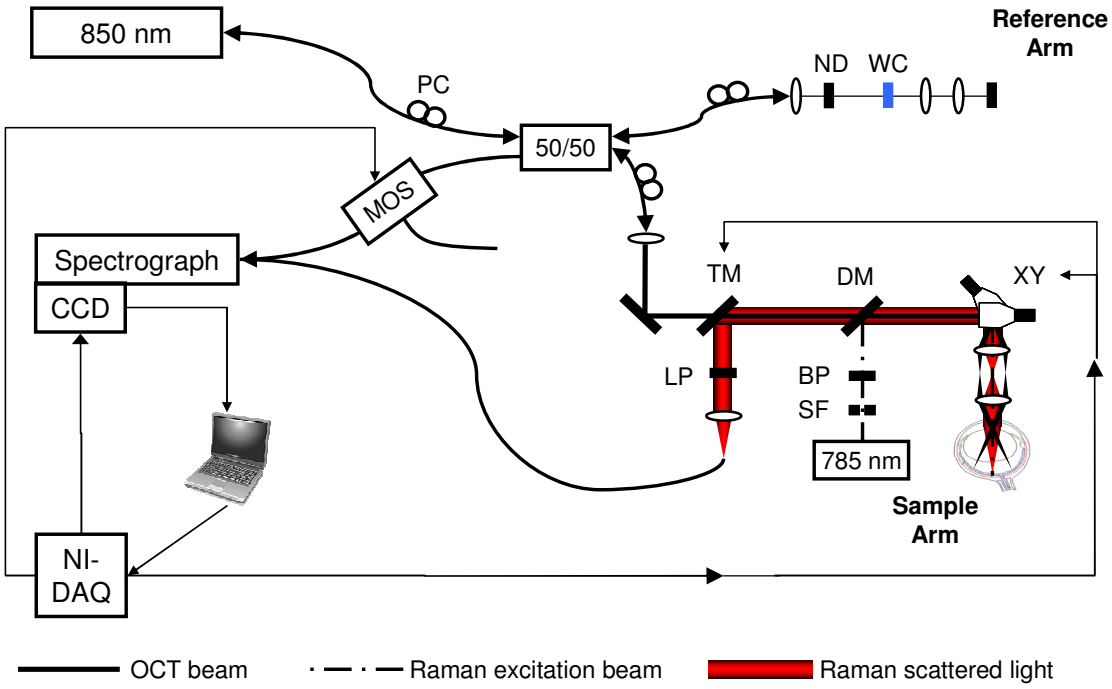

Fig. 4.1 (a) Illustrates the overlap between the Raman spectrum and the OCT source bandwidth along with a 2D image of the CCD illumination. (b) Overall RS-SDOCT System Schematic. PC – Polarization Control paddles, ND – Neutral Density filter, WC – Water filled Cuvette, TM – Translatable Mirror, LP – Long Pass filter, DM – Dichroic Mirror, BP – Band Pass filter, SF – Spatial Filter, XY – XY galvanometer pair, MOS – MEMS Optical Switch, NI-DAQ – National Instruments Multifunction DAQ.

The overall system schematic is shown in figure 4.1b. The OCT source is coupled to a 50/50 fiber splitter, which directs light to the sample and reference arms. Polarization control paddles are placed in the source, reference, and sample arms to fine tune the splitting ratio and optimize the detected interference signal. The sample arm includes an XY galvanometer pair and a set of achromats which produce a 14 μW collimated 2.1 mm beam that the eye then focuses onto the retina. This configuration results in a fan shaped scan pattern that allows maximum retinal coverage when the pupil of the scan is placed near the pupil of the eye. The reference arm consists of a set of achromats, a neutral density filter, and a 5 mm water filled cuvette. Insertion of the neutral density filter

allows the appropriate level of reference attenuation to optimize imaging sensitivity[9]. The optimized sensitivity of the system is measured at -86 dB. Care was taken to minimize degradation of the axial resolution due to dispersion mismatch. The dispersion from the physical optics of the system was compensated for by placing matching achromats in the reference and sample arms, resulting in a measured axial resolution of 11 μm in air (8 μm in tissue). The water filled cuvette compensated for dispersion arising from the eye itself. An optical MEMS switch (Thorlabs) is placed in the detection leg of the fiber interferometer. During acquisition of OCT images, the interference signal passes through to the spectrograph. During Raman acquisition, however, the OCT signal returning from the reference arm is directed away from the spectrograph so as not to overwhelm the Raman scatter.

The Raman illumination consists of free space optics integrated into the OCT sample arm. The multi-mode shaped source passes through a spatial filter and a 785 nm bandpass filter to produce a spectrally and spatially clean, collimated beam. A Raman dichroic mirror (Chroma) allows the beam to be co-aligned with the OCT beam and directed towards the sample. As with the OCT sample beam, the achromatic pair produces a collimated input beam with a power of 100 mW and a measured diameter of 2.4 mm (after the final achromat) that is then focused onto the retina by the eye. The Raman scattered light then returns back through the sampling optics and dichroic, and is redirected towards the Raman collection fiber by a mirror mounted to a translation stage. Before fiber coupling an 818 nm long pass filter further rejects elastic scatter. During OCT imaging, the translation stage is shifted aside to allow the OCT beam to freely pass.

The entire system is run off a single notebook computer with a LABView software interface. A multi-function DAQ device (National Instruments) allows software control of the optical MEMS switch, the translation stage mounted mirror in the sample arm, and the XY galvanometer pair. The instrument operates in either Raman or OCT mode. During OCT mode, the XY mirrors scan the beam across the retina to produce images while Raman scattered light is not detected. In Raman mode, OCT imaging is disabled and Raman spectra can be acquired from any XY galvo position, which correspond to the various depth scan axes of the previous OCT images and also noted in the OCT image display.

Data processing to produce OCT images and Raman spectra is performed in real-time. To create and OCT image, the reference arm signal is stored before each image acquisition, and then subtracted from subsequent depth scans to remove the DC component of the interference signal. After DC subtraction, the spectrum is inflated and remapped from wavelength space to linear k-space[14]. Fast Fourier transform then produces the depth scan. Multiple OCT images can be further averaged to improve signal to noise ratio of the system. Only the bottom rows of the CCD that are exposed to the OCT illumination are binned in order to acquire OCT spectra at a maximum line rate of 2.1 kHz. After factoring in data transfer and processing time, the frame rate of processed OCT images (512x512) is 2 frames/sec.

In order to process the Raman spectra, a number of calibrations are performed prior to sample analysis. Variations in system throughput are corrected for using a NIST calibrated quartz-tungsten-halogen white-light lamp. Relative wavenumber calibration is performed with conventional Raman standards such as acetaminophen and naphthalene. Laser induced fluorescence from the system optics and general background light is removed by subtracting background spectra. After a sample spectrum is white light corrected and background subtracted, the tissue autofluorescence is removed using a modified polynomial fitting algorithm[15].

Images and spectra were collected from a rodent model for retinopathy of prematurity (ROP), *ex vivo* to demonstrate the capabilities of the common detector RS-OCT instrument. ROP is generally considered a two-stage process arising from the variable oxygen tension preterm infants experience as a result of the therapeutic administration of supplemental oxygen and it's subsequent removal. The initial hyperoxia inhibits normal development of retinal vasculature, however upon return to norm-oxic conditions, hypoxia in the underperfused peripheral retina can prompt the sudden development of irregular vasculature and the subsequent retinal pathology. In the rodent model, rats are exposed to variable-oxygen (VO) environments that alternate between hyperoxic and normoxic conditions that simulate the exposure preterm infants are subjected to after birth[16]. Here, litters of Sprague-Dawley rats were randomly separated into groups placed in either VO or room air (RA) environments. The VO rats were placed with mothers in infant incubators within 4 hours of birth. The rats were cycled between

alternating periods of 24 hours at 50% oxygen followed by 24 hours at 10% oxygen, for 14 days. After the 14-day oxygen treatment protocol, the VO rats were moved to room air where 2nd stage of the pathological progression begins. Twelve days after removal from VO, denoted 14(12), distinct differences in the retina and retinal vasculature of the VO and age matched RA rats (denoted P26) are reduced, but still persist[17]. At this point, the rats were sacrificed, and the eyes were enucleated and placed in a small vessel atop a heating pad and half-submerged with phosphate buffered saline (PBS) (pH = 7.4, T = 35˚). The vessel was placed on a heating pad in order to maintain the temperate. The PBS bath and heating pad were fixed to 3-axis translation stage that allowed the sample to be appropriately positioned under the sampling optics for analysis with RS-OCT. PBS was also dripped over the eye periodically to prevent dehydration of the cornea. All OCT images and Raman spectra were acquired within 30 minutes of death. All experiments were conducted in the Vanderbilt University Biomedical Optics Laboratory with protocols approved by the Institutional Animal Care and Use Committee at Vanderbilt University and carried out in accordance with the National Institute of Health Guide for the Care and Use of Laboratory Animals (NIH Publications No. 80-23) revised 1996.

Results

The eyes from five 14(12) rats and four P26 were evaluated to demonstrated the morphological and biochemical differences detectable with common detector RS-OCT. Figure 4.2 shows representative OCT from the 14(12) and P26 rat eyes, along with the corresponding histology sections. OCT images for analysis were generated by averaging 20 successive frames. The images demonstrate the sufficient resolution and imaging range of the system to depict the retina. The clearest, most consistently visible layers include the hyper-reflective inner plexiform layer (IPL), a predominantly hypo-reflective band consisting of the inner nuclear layer (INL), outer plexiform layer (OPL), and outer nuclear layer (ONL), and outermost hyper-reflective regions of the eye which include the photoreceptor layers (PR) and choroid (C). Although less clear and consistent across the images, closer examination reveals the thin, hyper-reflective layer that corresponds to the nerve fiber layer at the innermost surface of the retina (NFL) proximal to a hypo-reflective band corresponding to the ganglion cell layer (GCL). Between the inner and

outer nuclear layers, a thin hyper-reflective band can be made out that corresponds to the OPL.

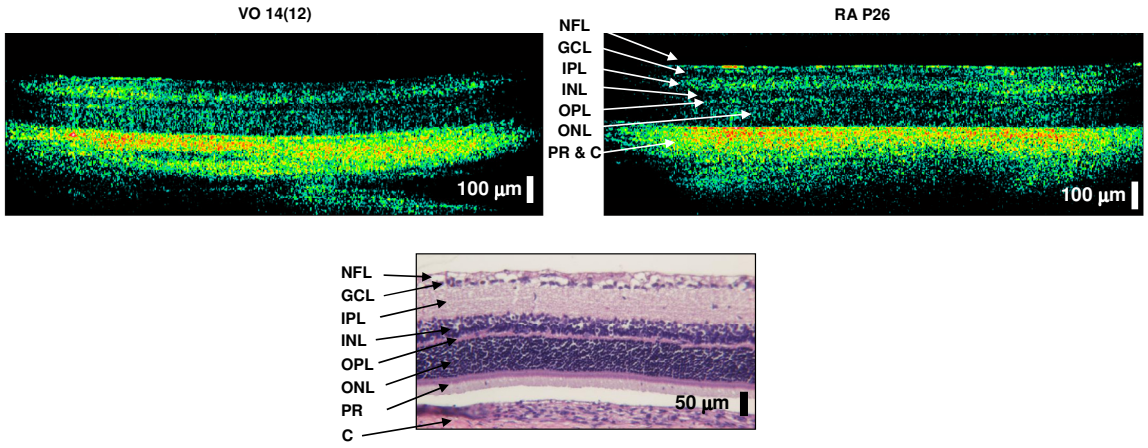

Fig. 4.2 Representative OCT and histology of VO 14(12) vs. RA P26 eyes. Images depict the ability of RS-OCT to resolve retinal structure in both the VO and RA rats. The layers of the retina visible, from inner layers to outer layers, include the thin, bright nerve fiber layer (NFL), hypo-reflective ganglion cell layer (GCL), thicker hyper-reflective inner plexiform layer (IPL), the hypo-reflective inner nuclear layer (INL), the thin, bright outer plexiform layer (OPL), the hypo-reflective outer nuclear layer (ONL), and the photoreceptor layer and choroid (PR & C), which are difficult to distinguish. In the representative histology section (20x magnification), the choroid has detached from the retina due to processing artifact and can be seen below the photoreceptor layers.

Although the images of the VO and RA retinas appear generally similar, the thickness of the hypo-reflective band consisting primarily of the nuclear layers (NL) of the retina (INL, OPL, and ONL) was measured to determine if any physical differences could be determined by RS-OCT. The NL band was selected because it is clearly defined across all the OCT images by the bright boundaries provided by the bottom of the IPL and the top of the PR layer. Figure 4.3a demonstrates how measurements of the layers were made. For each OCT image, a user defines 10 points along both the top and bottom boundaries of the NL. A 4^{th} order polynomial is then fit to the points to define the boundaries. The algorithm calculates the length of a vector that runs from the top of the PR layer to the bottom of the IPL, orthogonal to the surface of the PR layer, for 100 points evenly distributed across the retina. Thickness measurements were made on n=9 eyes from the VO 14(12) group and n=8 eyes from the RA P26 group. Images were not collected from one of the 14(12) eyes because temperature and corneal hydration conditions could not be maintained well enough to allow transmission of the light

through to the retina. The average NL thickness of the VO 14(12) group was 119 ± 9 µm, compared to 154 ± 15 µm for the RA P26 group (fig. 4.3b).

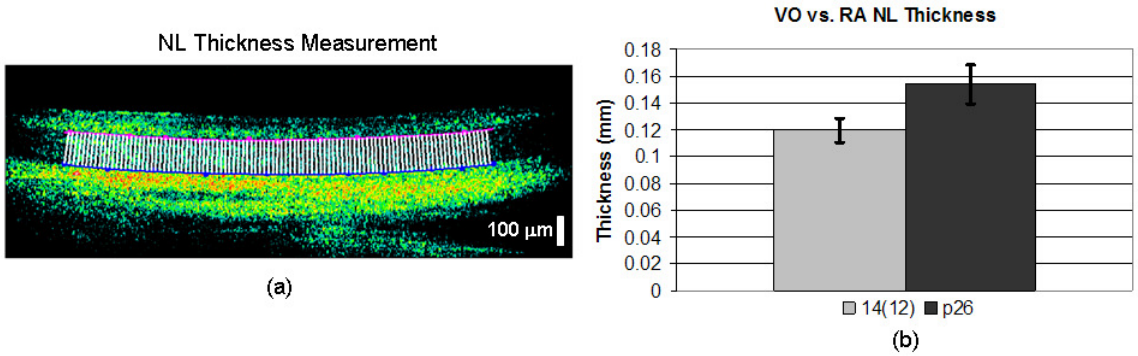

Fig. 4.3 Nuclear Layer Thickness Measurements in VO 14(12) vs. RA P26 retinas. (a)Thickness measurements of the hypo-reflective band that includes the INL, OPL, and ONL were made using an algorithm that fits a 4th order polynomial to user defined points along the upper and lower boundaries of the layers, and then calculates the mean distance between the fits. (b) Average thickness measurements of the VO 14(12) (n=9) vs. RA P26 (n=8) retinas. RA P26 thickness was greater ($p < 0.0001$).

Following imaging, Raman spectra were acquired ($t_{acquisition}$= 90 sec) from 9 positions evenly distributed across the surface of the retina for each eye. Spectra were collected from the 9 viable eyes from the 14(12) group (n=77 spectra) and the 7 viable eyes from the P26 group (n=56 spectra). The mean spectra from the two groups are shown in figure 4.4, along with reference spectra of dissected retina and lens from adult Sprague-Dawley rats. Individual spectra with either prohibitively low signal-to-noise or cosmic rays overlapping tissue Raman features were excluded from analysis. Low SNR was defined as the ratio of the 1003 cm^{-1} peak divided by the standard deviation of a region that lacked strong Raman intensity from 779 to 814 cm^{-1} being less than 7. The spectral features of the VO and RA retinas generally show similarities to those from the reference spectra, as well as those reported in the literature[18, 19]. The spectra show Raman peaks at 1003 cm^{-1} (phenylalanine), 1265 cm^{-1} (amide III), 1440 cm^{-1} (CH_x), 1660 cm^{-1} (amide I) that are typical to most tissues because of their common occurrence in biomolecules. This is evident when comparing the spectra measured from the intact VO and RA eyes with the reference retina and lens spectra.

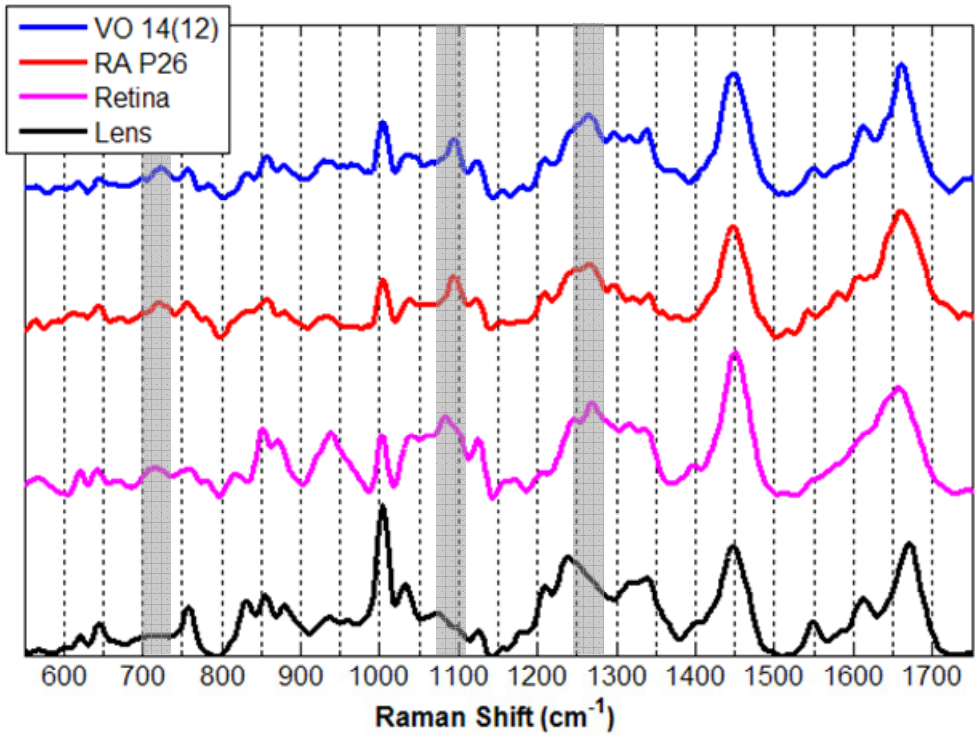

Fig. 4.4 Mean Raman Spectra of VO and RA retinas. The average spectrum of VO 14(12) (blue) and RA P26 (red) measured from intact eyes with RS-OCT. Reference spectra from dissected adult rat retina (purple) and lens (black) are also shown. Spectral features visible in the VO and RA spectra attributable to both retina (i.e. 723, 1094, 1265 cm^{-1}, highlighted) and the lens visible (i.e. 1549 and 1611 cm^{-1}).

The retina is unique in that it consists primarily of neuronal cells and their synapses. Protein signatures present in Raman spectra include those arising from DNA and RNA molecules present in the nuclear layers, the most intense of which occur at 723, 1094 cm^{-1}. Although these features are visible in the spectra collected from the intact eye, there are also features that indicate a contribution from the lens, which is not unlikely due to the strong Raman scattering intensity of the lens. The relative intensity of the 1003 cm^{-1} phenylalanine peak, the 1549 and 1611 cm^{-1} aromatic protein peaks, and the position and shape of the amide III peak near 1230 cm^{-1} are characteristic of β-sheet proteins[1], which exist in abundance in the lens. The amide III peak in α-helix proteins, which predominate in the layers of the retina, is normally shifted towards 1265 cm^{-1},[18] as seen in the reference retina spectrum. In order to reduce the relative contribution of lens signature in our measurements, a scaled subtraction of the reference lens spectrum from the measured spectra was performed. The resulting mean spectra from the VO and RA

retinas are shown in figure 4.5. The spectral features are now much more characteristic of the retina. The relative intensity of the 1003 cm^{-1} peak is more in line with that measured and reported in the literature, and the amide III peak is more distinctly appears at 1265 cm^{-1}, characteristic of α-helix proteins constituent in the retina.

Examination of the differences between the VO and RA lens subtracted retina spectra show a number of bands where differences reside. RA spectral intensity is increased at the 723, 1094, and 1580 cm^{-1} peaks, which are attributed to DNA and RNA nucleotide groups[1]. Increased intensity also is seen in the band from 610 to 670 cm^{-1} as well as the peak at 754 cm^{-1}, which have been attributed to amino acids and proteins[1].The VO spectra exhibit differences in the peaks at 929 cm^{-1}, a C-C peak commonly attributed to protein backbones, and a 965 cm^{-1} peak attributed to collagen molecules. In addition, the triplet of peaks in the band from 1315 to 1385 cm^{-1} shows increased intensity, which has been attributed to cytochrome-c content in the retina[18].

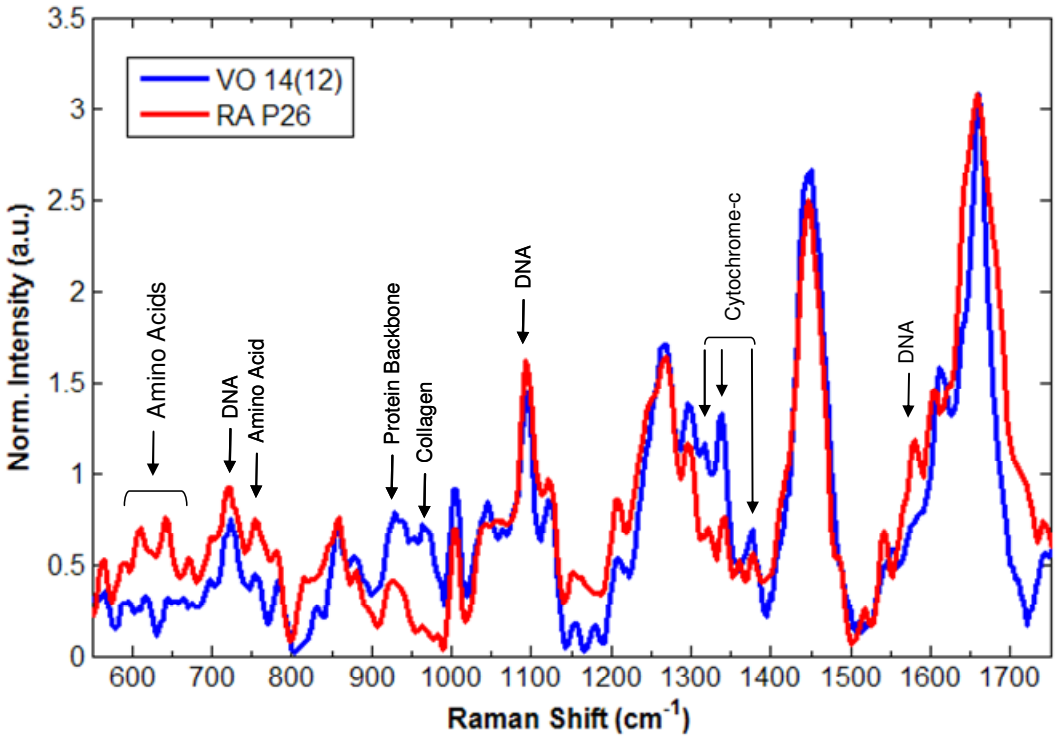

Fig. 4.5 Mean VO and RA spectra after scaled subtraction of lens features. Differences are seen in peaks attributable to proteins and amino acids (610-670 cm^{-1}, 754 cm^{-1}, and 929 cm^{-1}), DNA (723, 1094, and 1580 cm^{-1}), collagen (965 cm^{-1}) and cytochrome-c (1315-1385 cm^{-1}).

Discussion

The common detector RS-OCT instrument was able to both image and collect spectra from the retina. The OCT images depict the structure of the major layers of the retina typically seen in OCT images, while Raman spectra can be collected from the intact eye and processed to isolate signal primarily originating from the retina. The 50/10 VO rodent model for ROP is a well developed model primarily utilized to evaluate pathological development of neovasculature. After the rat pups are reintroduced to room air at 14(0), a strong vascular response is develops and peaks at 14(6), however by 14(12) the pathological vasculature has largely resolved. Although the speed of the vascular regression is one criticism of the model, as a whole pathological features have been shown to persist[17]. A developmental delay is very likely to result from the irregular retinal perfusion from 14(0) to 14(12), and our results seem to indicate that measures of this can be made with RS-OCT. Taken together, the Raman signatures provide information that both builds upon the morphological information seen in the OCT, as well as compliments it. The increased intensity of the DNA and amino acid peaks seems in line with the increased nuclear layer thickness measured by OCT. In humans, advanced ROP can be severe enough to result in retinal detachment with extreme irregularity in vasculature growth patterns or significant increase vascular permeability. In the animals examined here, the speed with which the pathological vasculature re-normalized seem to prevent any detectable detachments with OCT. The inability of the OCT images shown here to clearly distinguish between the photoreceptor layers, retinal pigment epithelium, and choroid likely would have made this task quite difficult in the case of minor detachments.

Spectral changes that do reflect features of in the OCT image can be particularly interesting. The spectral changes observed in the 1315 to 1385 cm^{-1} range imply biochemical differences that between the VO and RA retinas that are not clearly reflected in OCT. A similar triplet of peaks was seen in work utilizing confocal RS to collect spectra from the mitochondria rich photoreceptor inner segments and attributed to cytochrome-c[18], a protein localized in the mitochondria associated with cellular metabolism. In the retina, mitochondria are localized in the photoreceptor layer, where production and turnover of the membrane bound visual pigments takes place. One

possible explanation of the increased cytochrome-c content in the VO rats may be an increased level of rhodopsin generation in the developmentally delayed animals. The collagen feature arising from the 965 cm^{-1} peak may be attributable to collagen fibrils at the vitreo-retinal interface, which are believed to play a role in vitreal traction[20]. In the case of the VO rats, a significant portion of the pathological retinal vasculature develops as tufts into the vitreous. A hypothesis for increased collagen features may be related to their necessity to maintain vitreal traction in the VO rats. The increased spectral intensity associated with C-C backbone at 929 cm^{-1} is more difficult to attribute without further analysis due to its widespread presence among bio-molecules. Although no clear conclusions can be drawn at this stage from any of the biochemical differences seen in the Raman spectra, it is clear that they provide unique information that can be expanded upon to better understand the molecular differences between the retinas of VO 14(12) and RA P26 animals.

Appropriate design of the common-detector RS-OCT instrument required the appropriate selection of light sources suited to the tissue of interest as well as facilitate a common detector. Typically, NIR Raman is performed with sources between 633 - 830nm and Silicon-based detectors. As the excitation wavelength is increased, scattering intensity and detector responsivity fall off, while background tissue autofluorescence tends to decrease. An additional critical factor is the availability of the appropriate filters to reject elastic scatter and attenuate laser background. For OCT imaging, broadband sources with bandwidths amenable to micron scale resolution are typically found at the optical communication bands between 800 to 850 nm, 1310 nm, and 1550 nm. OCT source selection is typically a function of the target tissue of interest. In highly scattering tissues such as the GI tract and skin, longer wavelengths are preferred due to the lower scattering coefficients of tissue facilitating deeper penetration. Imaging the retina, however, requires the light pass through the aqueous and vitreous to arrive at the retina, and thus OCT sources from 800 to 850 nm are preferred due to their proximity to minima in the water absorption spectra. Ultimately, the selection of a 785 nm source for Raman and 850 nm source for OCT allowed both the appropriate overlap for common detection as well as the optimal wavelengths for retinal analysis.

The performance characteristics that result from the spectrometer design are critical in both RS and OCT, however their requirements are not necessarily the same. The appropriate range of spectral coverage for detection of the biological molecules lies in the organic fingerprint region of 500 to 2000 cm^{-1} relative wavenumbers, with spectral resolutions of at least 10 cm^{-1} to detect the sharp features of the Raman signature. In spectral domain OCT, the axial resolution is inversely related to the laser source bandwidth while the maximum un-aliased depth range is inversely related to the spectral resolution. Therefore, a detection system designed with too narrow a spectral range will degrade the axial resolution, while a detection system with too large a spectral range can degrade the spectral resolution and result in an unaliased depth range less than the optical penetration depth in tissue. The ultimate design of the spectrograph allowed a sufficient spectral resolution for both a sufficient un-aliased OCT imaging depth and resolution of the sharp features of tissue Raman spectra, along with sufficient spectral coverage to include the tissue "fingerprint" region as well as achieve the full axial resolution in OCT.

The OCT resolution allows visualization of the retinal layers in the rodent model, however the overall speed and sensitivity of the instrument are sacrificed at the expense of Raman sensitivity. The maximum achievable readout rate for high-sensitivity CCD's is purposefully low in order to minimize the noise associated with higher bandwidth amplifier electronics. Similarly, CCD full well capacity is typically kept at a minimum in order to optimize dark noise performance for the benefit of RS. In OCT, a higher full well capacity is necessary in order to detect large reference DC signal required to generate interference. An increased well capacity would prevent camera saturation at such low power levels, and allow more power delivered to the sample. OCT performance could be slightly improved through selection of a CCD with faster electronics and larger wells, however it would come at the expense of RS quality. Despite the fact that the detection is optimized for Raman sensitivity, the high illumination power and long integration times necessary for RS remain the limitations of the instrument. These parameters would surely need to be reduced for any human application; however they do not preclude feasibility in rodent models.

In conclusion, we have demonstrated the feasibility of a common detector combined RS-OCT instrument for the *ex vivo* characterization of the morphological and

biochemical features of rodent retina. The ability of the instrument to sequentially acquire high resolution images and high quality Raman spectra was demonstrated in a rodent model for ROP. Combined RS-OCT was successful in identifying changes in both of the thickness and biochemistry of the pathological retinas. Future work consists of demonstrating the feasibility of the instrument for characterizing rodent models for retinal pathology *in vivo*.

Acknowledgements

The authors would like to acknowledge the contributions of Ash Jayagopal, Gary McCollum, Susan Yanni, Meghan from the Penn Lab, and E. Duco Jansen.

References

1. A. Mahadevan-Jansen and R. Richards-Kortum, "Raman Spectrscopy for the Detection of Cancers and Precancers," Journal of Biomedical Optics **1**(1), 31-70 (1996).
2. T. J. Romer, J. F. Brennan, 3rd, M. Fitzmaurice, M. L. Feldstein, G. Deinum, J. L. Myles, J. R. Kramer, R. S. Lees, and M. S. Feld, "Histopathology of human coronary atherosclerosis by quantifying its chemical composition with Raman spectroscopy," Circulation **97**(9), 878-885 (1998).
3. P. J. Caspers, G. W. Lucassen, and G. J. Puppels, "Combined in vivo confocal Raman spectroscopy and confocal microscopy of human skin," Biophys J **85**(1), 572-580 (2003).
4. Z. Huang, S. K. Teh, W. Zheng, J. Mo, K. Lin, X. Shao, K. Y. Ho, M. Teh, and K. G. Yeoh, "Integrated Raman spectroscopy and trimodal wide-field imaging techniques for real-time in vivo tissue Raman measurements at endoscopy," Opt Lett **34**(6), 758-760 (2009).
5. C. A. Patil, N. Bosschaart, M. D. Keller, T. G. van Leeuwen, and A. Mahadevan-Jansen, "Combined Raman spectroscopy and optical coherence tomography device for tissue characterization," Optics Letters **33**(10), 1135-1137 (2008).
6. J. W. Evans, R. J. Zawadzki, R. Liu, J. W. Chan, S. M. Lane, and J. S. Werner, "Optical coherence tomography and Raman spectroscopy of the ex-vivo retina," J Biophotonics **2**(6-7), 398-406 (2009).
7. G. Hausler and M. W. Lindner, "``Coherence Radar'' and ``Spectral Radar''---New Tools for Dermatological Diagnosis," Journal of Biomedical Optics **3**(1), 21-31 (1998).
8. J. J. Baraga, M. S. Feld, and R. P. Rava, "Rapid near-Infrared Raman-Spectroscopy of Human Tissue with a Spectrograph and Ccd Detector," Applied Spectroscopy **46**(2), 187-190 (1992).
9. R. Leitgeb, C. K. Hitzenberger, and A. F. Fercher, "Performance of fourier domain vs. time domain optical coherence tomography," Optics Express **11**(8), 889-894 (2003).
10. M. E. van Velthoven, D. J. Faber, F. D. Verbraak, T. G. van Leeuwen, and M. D. de Smet, "Recent developments in optical coherence tomography for imaging the retina," Prog Retin Eye Res **26**(1), 57-77 (2007).
11. M. Ruggeri, G. Tsechpenakis, S. Jiao, M. E. Jockovich, C. Cebulla, E. Hernandez, T. G. Murray, and C. A. Puliafito, "Retinal tumor imaging and volume quantification in mouse model using spectral-domain optical coherence tomography," Opt Express **17**(5), 4074-4083 (2009).
12. K. H. Kim, M. Puoris'haag, G. N. Maguluri, Y. Umino, K. Cusato, R. B. Barlow, and J. F. de Boer, "Monitoring mouse retinal degeneration with high-resolution spectral-domain optical coherence tomography," J Vis **8**(1), 17 11-11 (2008).
13. J. V. Glenn, J. R. Beattie, L. Barrett, N. Frizzell, S. R. Thorpe, M. E. Boulton, J. J. McGarvey, and A. W. Stitt, "Confocal Raman microscopy can quantify advanced glycation end product (AGE) modifications in Bruch's membrane leading to

accurate, nondestructive prediction of ocular aging," Faseb J **21**(13), 3542-3552 (2007).
14. M. Wojtkowski, R. Leitgeb, A. Kowalczyk, T. Bajraszewski, and A. F. Fercher, "In vivo human retinal imaging by Fourier domain optical coherence tomography," Journal of Biomedical Optics **7**(3), 457-463 (2002).
15. C. A. Lieber and A. Mahadevan-Jansen, "Automated method for subtraction of fluorescence from biological Raman spectra," Applied Spectroscopy **57**(11), 1363-1367 (2003).
16. J. S. Penn, B. L. Tolman, and L. A. Lowery, "Variable oxygen exposure causes preretinal neovascularization in the newborn rat," Invest Ophthalmol Vis Sci **34**(3), 576-585 (1993).
17. K. A. Roberto, B. L. Tolman, and J. S. Penn, "Long-term retinal vascular abnormalities in an animal model of retinopathy of prematurity," Curr Eye Res **15**(9), 932-937 (1996).
18. J. R. Beattie, S. Brockbank, J. J. McGarvey, and W. J. Curry, "Effect of excitation wavelength on the Raman spectroscopy of the porcine photoreceptor layer from the area centralis," Mol Vis **11**, 825-832 (2005).
19. J. R. Beattie, S. Brockbank, J. J. McGarvey, and W. J. Curry, "Raman microscopy of porcine inner retinal layers from the area centralis," Mol Vis **13**, 1106-1113 (2007).
20. T. L. Ponsioen, M. J. van Luyn, R. J. van der Worp, J. C. van Meurs, J. M. Hooymans, and L. I. Los, "Collagen distribution in the human vitreoretinal interface," Invest Ophthalmol Vis Sci **49**(9), 4089-4095 (2008).

CHAPTER V

MANUSCRIPT 4

A Clinical Instrument for Combined Raman Spectroscopy-Optical Coherence Tomography of Skin Cancers

Chetan A. Patil[1], Harish Kirshnamoorthi[1], Darrel L. Ellis[2,3], and Anita Mahadevan-Jansen[1]

[1]Department of Biomedical Engineering, Vanderbilt University, Nashville TN, USA
[2]Division of Dermatology, Department of Medicine, Vanderbilt University, Nashville TN
[3]Dermatology Service, Veterans Affairs Tennessee Valley Healthcare System, Nashville, TN, USA

Prepared for Submission to *Optics Express*

Abstract

Skin cancer is the most commonly occurring cancer, with incidence rates rising annually. Realizing favorable outcomes requires early diagnosis, for which the current standard is biopsy followed by histopathology. This process can be invasive, subjective, time consuming, and costly. Optical techniques, including Optical Coherence Tomography (OCT) and Raman Spectroscopy (RS), have been developed to perform non-invasive characterization of skin lesions, however neither is without limitation. Here, we demonstrate a clinical instrument for morphological and biochemical characterization of skin cancers with combined RS-OCT. The portable instrument utilizes independent RS and OCT system backbones, and is integrated in a common clinical probe. The potential of the probe for cancer diagnosis is demonstrated on malignant and non-malignant lesions.

Introduction

Skin cancer is the most commonly occurring of all cancers, accounting for more than a 1.7 million incidences in the United States annually[1]. In addition, the incidence rates for skin cancer are growing, particularly among young Caucasian women aged 15-34 (3.8% annually) and Caucasian men aged over 65 (8.8% annually) [1]. The two most common types of skin cancer, basal cell carcinoma (BCC) and squamous cell carcinoma (SCC), are highly curable if detected at an early stage. The most dangerous skin cancer, malignant melanoma, can have a 5 year survival rate of only 16% at it's most advanced stage, cases detected *in situ* have survival rates of 99%[2]. Early diagnosis and thorough treatment (i.e., complete resection) are the keys to gaining a favorable prognosis; however diagnosis of skin cancers can be difficult. Many benign lesions visually resemble malignancies, and in elderly patients with a large number of irregular skin lesions, it can be easy to overlook disease. While in many cases, preemptive removal may be a simple solution, it can result in unnecessary cost and patient discomfort. Reliable clinical diagnosis typically requires biopsy and subsequent histo-pathological examination. Clinicians are then presented with the challenge of deciding which and how many skin lesions to biopsy, usually relying on visual inspection and palpation. This

protocol for skin lesion diagnosis is accepted as the gold-standard; however it can be subjective, invasive, time-consuming, and costly. These limitations motivate the development of non-invasive techniques capable of direct characterization and monitoring of potentially cancerous skin lesions. Such tools have the potential to assist in biopsy guidance, or possibly even circumvent the need for histology.

Optical techniques have demonstrated the potential to perform non-invasive characterization of skin cancers. Imaging techniques such as confocal microscopy[3] and optical coherence tomography (OCT)[4] are advantageous because they allow non-invasive visualization of tissue micro-structure similar to that currently obtained invasively with histology. However these techniques are typically limited in their ability to characterize the tissues biochemical composition, and therefore lack the specificity necessary for disease classification. Spectroscopic techniques including fluorescence[5] and Raman spectroscopy (RS)[6], have been demonstrated capable of performing highly specific disease classification with automated, statistical algorithms that provide objective correlation of spectra to pathological state. Unfortunately, these spectroscopic techniques typically lack the ability to perform imaging at high resolutions in clinically relevant timeframes.

The appropriate combination of imaging and spectroscopy methods can take advantage of the complimentary nature of the data sets structural and biochemical sensitivity to result in a clinical device that provides more complete information for diagnosis and tracking of skin cancers. The development of multimodal instruments combining imaging and spectroscopy is the most straightforward approach to realize these potential benefits. For instance, combined laser induced fluorescence-OCT demonstrated the advantages of combining imaging with spectroscopy to characterize the cancer in the colon of a rodent model[7]. In the skin, a confocal RS-confocal reflectance microscopy probe demonstrated the ability to acquire images with cellular level resolution along with the micron scale biochemical analyses of tissue structures, *in vivo*[8]. For the specific purpose of clinical screening and diagnosis of skin cancer, however, such approaches are limited.

Although confocal reflectance microscopy can achieve excellent resolution, the limited imaging depth can prevent accurate determination of the depth of tumor cell

invasion for staging, while the limited transverse field of view (FOV) can restrict the area of skin that is observable in a single clinical session. OCT, on the other hand, is able of achieving micron-scale resolution with extended penetration depths and over a larger FOV, which simplifies clinical application. While common implementations of OCT do not achieve sub-cellular resolution, the technique has still been demonstrated capable of visualizing the microstructural features of a wide range of skin cancers[9, 10]. In addition, a recent study demonstrated that dermatologists and pathologists could be trained to identify skin lesions such as BCC and actinic keratosis (AK, a non-malignant skin lesion) with a sensitivity of as high as 96%, indicating that OCT provides an excellent tool for detecting disease[11]. However, these observers had a difficult time determining if the lesion was a BCC or an AK, indicating the limitation of OCT to perform classification based on strictly tissue morphology.

Conversely, RS would seem to be an excellent spectroscopic approach for highly specific classification of disease type. In comparison to autofluorescence spectroscopy, which is sensitive to a limited number of intrinsic fluorophores in the skin, Raman spectroscopy is sensitive to a wide number of molecular moieties in the skin[12]. In a direct comparison with autofluorescence and diffuse reflectance spectroscopy, Raman spectroscopy has been shown to achieve superior classification performance in the context of breast cancer diagnosis. In the skin, Raman spectroscopy has demonstrated the ability to perform direct multi-class classification of skin diseases with overall accuracies of 95% [6, 13]. The combination of RS and OCT would facilitate high-resolution imaging of the microstructural features of skin disease, along with highly specific characterization of the biochemical composition of skin cancers. The potential advantages of combined RS-OCT have previously been reported in a non-portable benchtop configuration[14]. Here, we describe the design and application of a clinical instrument for combined RS-OCT for *in vivo* imaging and spectroscopy of skin cancers.

Materials and Methods

System Instrumentation

The combined RS-OCT system schematic is shown in figure 5.1a. The backbone of the OCT subsystem is a typical high-speed time-domain configuration. A 1310 nm fiber coupled optical amplifier source ($\Delta\lambda_{FWHM}$ = 60 nm, AFC technologies) is coupled to a 2x2 fiber splitter (50:50 coupling ratio). The reference arm consists of a rapid scanning optical delay line that facilitates high speed imaging up to 32 frames/second (data collected here was acquired at 2 frames/second) [15]. The OCT subsystem is fiber coupled to a custom designed RS-OCT probe that directs the light onto the sample. The light returning from the sample probe interferes with the light returning from the sample arm at the fibersplitter. The interference signal is then detected by a balanced detector that collects the interference signal in the detection leg as well as the interference signal circulated back from the source arm for high sensitivity detection (-105 dB) [16]. The electronic signal is then band pass filtered and detected with a multi-function analog input / analog output data acquisition device (National Instruments). The Raman subsystem consists of a wavelength stabilized laser diode source located entirely within the probe and controlled externally by an electronic module (Innovative Photonics Solutions, Inc.). The Raman scatter is collected, fiber coupled, and sent to a high throughput spectrograph (Kaiser Optical Systems) that disperses the light onto back illuminated, deep depletion, thermo-electrically cooled CCD (Andor Technologies) for detection. All the components of the OCT and RS subsystems are housed with in a mobile cart (fig 5.1b) that facilitates transportation to the clinic, and mobility from one exam room to another.

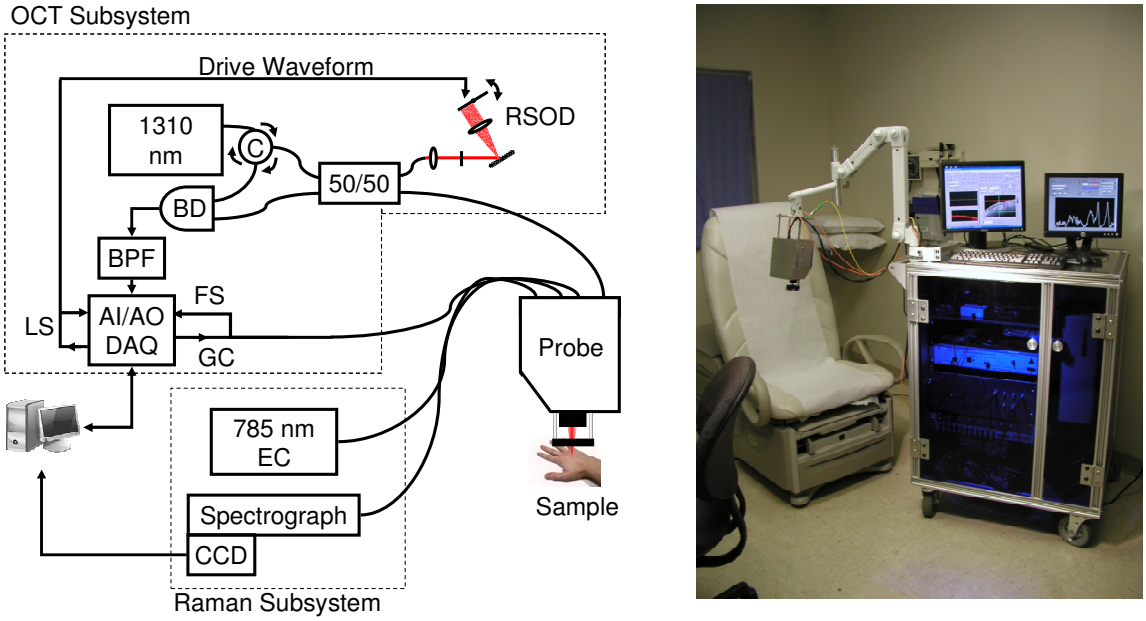

Fig. 5.1 RS-OCT System: Schematic diagram of the clinical RS-OCT system (a). The OCT subsystem consists of a 1310 nm source coupled into a 50/50 fiber splitter. Reference Arm consists of a rapid scanning optical delay (RSOD). A circulator redirects light returning to the source towards a balanced detector (BD). The interference signal is then band-pass filtered (BPF), and detected with an analog input/output data acquisition card (AI/AO DAQ). The DAQ generates galvanometer control (GC) output signals, along with the line sync (LS) and frame sync (FS). The Raman subsystem consists of the laser source's electronic control (EC) module that is tethered to the laser diode which resides within the body of the probe. The Raman scatter is fiber coupled in the probe and detected with a spectrograph and CCD. A photograph of the RS-OCT system (b) shows the cart, mechanical arm, probe, and software interface layout.

Combined RS-OCT Sample Probe

The combined RS-OCT sample probe is depicted in figure 5.2. The Raman source is a 785 nm diode laser device with a 1" x 1" footprint that contains the diode and TEC (Innovative Photonics Solutions). The source outputs a collimated beam that is band pass filtered and co-aligned with the OCT beam at dichroic mirror 1. The objective lens and galvanometer (Cambridge Technologies) are configured to generate a telecentric scan for OCT image generation. The measured axial resolution of OCT is 14 µm. The objective lens focuses the OCT beam to a 25 µm lateral spot ($P_{OCT\ sample}$ = 7 mW). During Raman acquisition, galvanometer scanning is stopped, and the Raman spectrum is acquired from the central optical axis of the objective lens. The Raman beam is focused to a 44 µm lateral spot with a measured confocal parameter of 3.8 mm ($P_{Raman\ sample}$ = 50 mW). The

Raman scatter band from 800 - 950 nm is separated from the Raman excitation and OCT by dichroic mirror 2 (Chroma Technologies, Inc.), long pass filtered (Semrock, Inc. λ_{cutoff} = 808 nm) to further reject elastic scatter, and coupled into a 100 μm low-OH fiber for detection. The overall size of the probe is 4" (H) x 5"(W) x 8"(L). The probe is mounted to a manually manipulated mechanical arm that supports the probe's weight and provides stability during collection of Raman spectra (seen in fig 5.1b). The operator is still required to hold the probe in place during imaging and spectral acquisition.

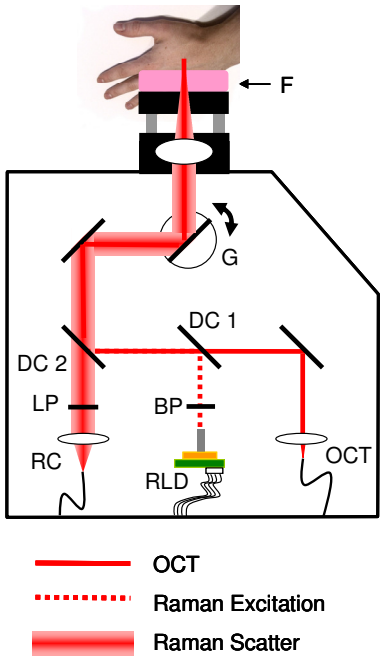

Fig. 5.2 Schematic diagram of the clinical probe. The Raman laser diode (RLD) is band pass filtered (BP) and co-aligned with the OCT beam at dichroic mirror 1 (DC 1). The Raman excitation and OCT beams are directed at the sample via a galvanometer (G) and objective lens (OL) pair that perform a telecentric scan of the OCT beam during imaging. The Raman scatter is separated from the OCT and Raman excitation by dichroic mirror 2 (DC 2), long pass filtered (LP) and detected by the Raman collection (RC) optics. A foam pad (F) is attached to the sample end of the probe for patient comfort.

Data Pre-processing and Software Interface

A custom designed software interface (LabView) performs instrument control, data acquisition, data processing, and image / spectrum display for both the OCT and Raman systems. The software performs demodulation of full interferometric OCT signal, and real-time processing and display of both the OCT image and Raman spectra.

Calibration of the spectral dispersion of the Raman system was performed daily using the atomic emission lines of a neon-argon lamp prior to data collection. Variations in spectral throughput of the system were calibrated using a NIST-certified quartz-tungsten-halogen lamp. Relative Raman wavenumber shift was calibrated with acetaminophen and naphthalene standards. Background spectra are acquired to remove laser-induced fluorescence from the sampling optics. Spectral pre-processing includes binning the data to ½ the spectral resolution and high frequency noise removal with a 2nd order Savitzky-Golay filter with a window size twice the spectral resolution. Finally, background tissue autofluorescence was subtracted with a modified polynomial fitting algorithm[17], and the resulting spectra were area normalized in order to maintain potentially relevant information from all peaks.

Study Protocol

The combined RS-OCT clinical system and probe were used to characterize skin cancers in the Dermatology service of the Veterans Affairs – Tennessee Valley Health Care System (VA-TVHS). All procedures were performed in accordance with a protocol approved by the VA-TVHS institutional review board.

Patients presenting in the clinic for routine resection of lesions previously identified as cancerous via biopsy and pathology were eligible for enrollment. In some instances, the initial biopsy removed the entire lesion, resulting in a lesion that consisted simply of scar tissue, while in other cases significant tumor cells remained. OCT images of the presumed lesion were acquired to provide an overview of its microstructural features. OCT imaging was then suspended and Raman spectra were acquired from the center of the lesion for biochemical characterization. Due to the inherent heterogeneity of skin, spectra and images were then acquired from regions directly adjacent to the lesion that appeared visibly normal (within 3-4 cm's) for comparison. Three (3) spectra from each measurement location were averaged to produce a single spectrum per position. The acquisition time for individual Raman spectral was 30 seconds. After data acquisition, a 2 mm punch biopsy was taken from the center of the lesion near the Raman measurement site for histopathological correlation with the RS-OCT data. In addition, the results in

patient record from histopathology of the entire removed tissue area were also noted to confirm punch biopsy diagnosis. Lesion resection typically includes 1 cm clear margins.

Results

An OCT image of normal skin from the forearm of a 62 year old male is shown in figure 5.3a. The epidermal layer is non-distinct, but can be observed as a slightly darker band indicated by the black arrow on the far left of the image. The OCT image from the corresponding lesion is shown in figure 5.3b. The OCT image displays some clear morphological irregularities indicative of a lesion, however both the 2 mm punch biopsy (fig. 5.3d) and the pathology report in the patient record indicated that the entire area was clear of tumor. The red arrow in the OCT image frame approximates the position at which the lesion Raman spectra were acquired. The mean Raman spectra from the two positions are shown in figure 5.3c. The overall shapes of the spectra show subtle differences in intensity near 630 cm^{-1} and the band from 1250 to 1350 cm^{-1}.

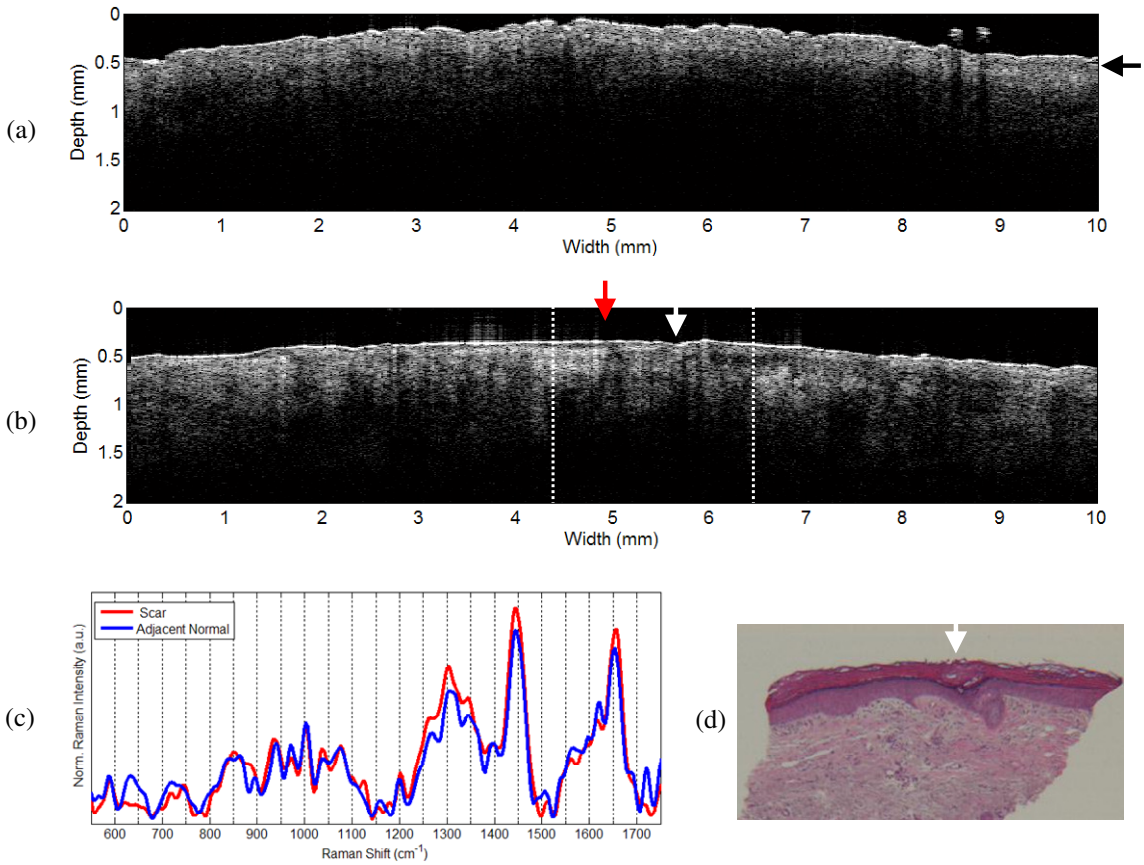

Fig. 5.3: RS-OCT of a forearm scar lesion. (a) OCT of normal skin adjacent to the lesion. Characteristic features include the lack of morphological irregularities and a relatively consistent attenuation of signal through the dermis. (b) OCT of scar. Red arrow approximates location of Raman acquisition. Dashed white lines outline approximate correlation with 2 mm punch biopsy (d). White arrow indicates landmark dip in skin surface. Raman spectra (c) are fairly similar. Scar contains higher content in band from 1250 to 1350 cm^{-1}

Figure 5.4 depicts the RS-OCT data collected from an 83 year old male with a superficial BCC of the zygoma (cheekbone). The OCT image of the adjacent normal skin (fig. 5.4a) shows some signs of structural inconsistency in contrast with the normal skin seen in figure 5.3a. The dark protrusions nearly orthogonal to the surface of the skin may be hair follicles. The OCT of the superficial BCC also shows a number of signs of hypo-reflective sub-dermal irregularities that may be either non-malignant features such as hair follicles and sebaceous glands, or tumor cell nests. The Raman spectra (fig. 5.4c) show distinctly different spectra from the lesion and adjacent normal skin. The most notable difference is in the lineshape and peak ratios of the features in the 1250 to 1350 cm^{-1} band. In addition, the width of the 1666 cm^{-1} peak shoulder is broadened, as seen by increased intensity in the 1625 cm^{-1} wavenumber region. The data from RS-OCT of a

BCC is shown in figure 5.4. Pathology confirmed diagnosis as a BCC, but was cut longitudinally, and therefore not shown.

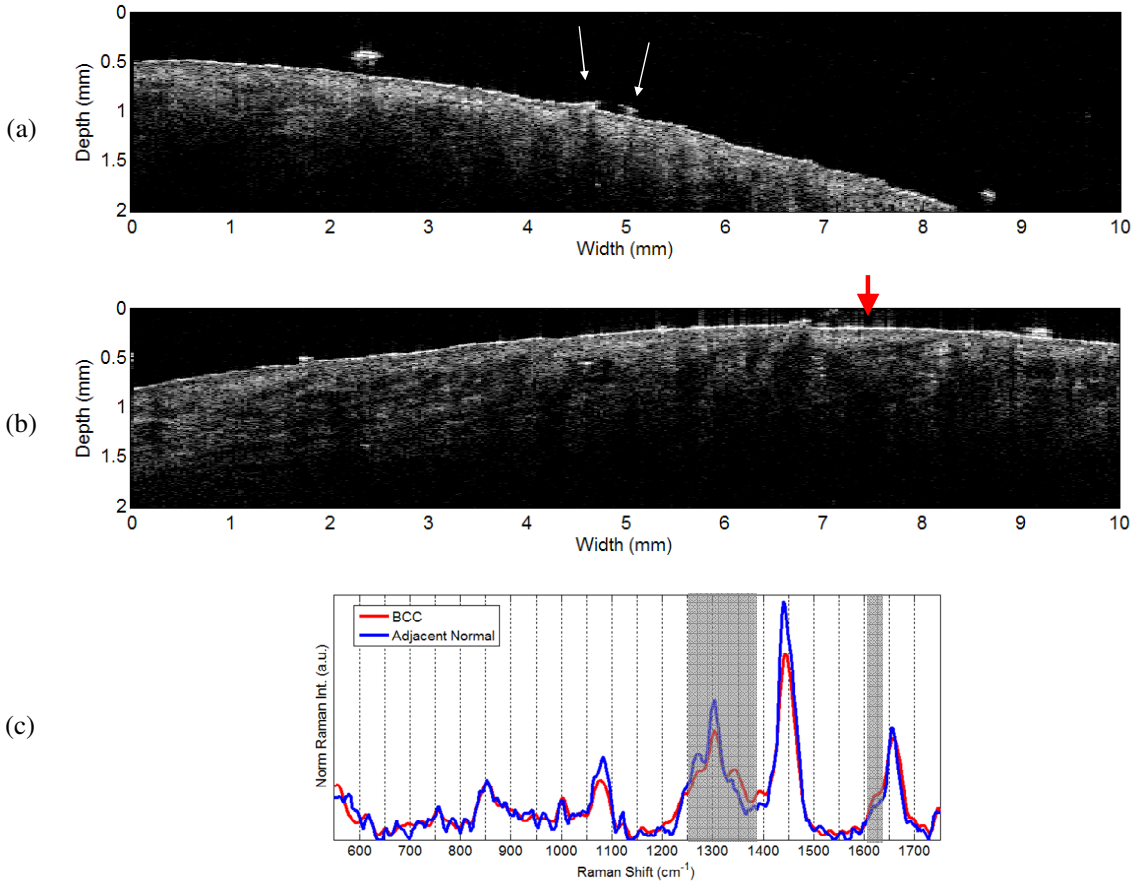

Fig. 5.4: RS-OCT of Basal Cell Carcinoma of Right Zygoma (cheekbone). OCT image of normal skin adjacent to lesion (a) shows some features of sub-surface irregularity that are likely hair follicles. The lesion OCT image shows a number of dermal irregularities with both thin and larger hypo-reflective scattering features. Red arrow approximates position where lesion Raman spectra were acquired. Distinct differences are seen in the Raman spectra (c) acquired from the BCC and normal, particularly in the 1250 to 1350 cm^{-1} band and the region around 1625 cm^{-1} band.

Discussion

The OCT images of the normal skin (figs. 5.3a, 5.4a) demonstrate the characteristic appearance of normal skin. Normal skin on the forearm is quite different from normal skin on the face, which can be seen in the figures. The forearm skin shows fairly consistent signal decay as a function of depth and a general lack of absorptive or scattering irregularities that would result in hyper- or hypo- reflective features. In contrast, the image of normal skin on face contains some more irregularities indicative of tissue heterogeneity. The skin on the face is known to have higher concentrations of

sebaceous glands in comparison to other locations on the body. These structures typically surround hair follicles, and seem to appear as appear as dark, hypo-reflective features[18]. These features have a wide variety of shapes in histopathology, based on the angle of the cut, and therefore should also be heterogenic in the OCT cross sections. If they are imaged at the right angle, they should be visible emerging to the surface of the skin, as is likely the case with the features identified by the white arrows in figure 4a. The features of the skin on the face (fig. 5.4a, 5.4b) also exhibit characteristics indicative of shaving, including a flat surface and a more visible, flattened smooth epidermal layer.

The Raman spectra acquired from both the lesions and their adjacent normal skin sites have features that are typical of the skin[19, 20]. These features include the tyrosine/protein peak near 850 cm^{-1}, phenylalanine ring breathing peak at 1003 cm^{-1}, the PO_2 symmetric stretching peak attributed to lipids as well as the nucleic acid backbone in the 1070-1090 cm^{-1} band, the amide III band centered around 1304 cm^{-1}, the 1440 CH_2 peak, and the 1660 cm^{-1} amide I are all clearly visible, in addition to other less prominent spectral features.

In contrast to the image of the normal forearm skin, that of the forearm scar shows distinct morphological irregularities at both the surface and in the underlying dermis. The process of re-epithelialization of the wound's has been observed with OCT[21], and this image contains the hallmarks of such a process. On the surface, the scar appears distinctly flat and smooth. The newly formed epithelial layer is more distinct, flat, and smooth, underneath which is the bright hypo-reflective scar tissue just to the left of the red arrow. The Raman spectra are fairly similar. Normal skin shows increased signal at 634 cm^{-1}, while the scar/inflammation tissue shows an increased band from 1250 to 1350 cm^{-1}. The spectral lineshape of the 1270, 1304, and 1348 cm^{-1} peaks suggests an increase nuclei and protein contribution comes[22], and may indicate an increased presence of inflammatory cells in the involved area.

The superficial BCC OCT image contains markedly more hypo-reflective structures in the underlying dermis in comparison to its normal counterpart, however it is difficult to assess much more than that due to the generally similar appearance of features. BCC tumor cell nests have been similarly reported to appear and dense hypo-reflective regions in the tissue[9], which is similar to sebaceous glands. The morphology of

both BCC and sebaceous glands cannot necessarily be predicted, and as such it is difficult to assess the features based on their shape. The Raman spectra, however, provide some indication of the biochemical composition of the tissue. The differences in the spectra seem to indicate higher lipid content in the normal skin compared to the cancer. This is based on the different spectral lineshape of 1250-1350 cm^{-1} amide III band, as well as the narrower width of the amide I band at 1667cm^{-1}. The spectral lineshape of the 1270, 1304, and 1348 cm^{-1} peaks suggests the contribution comes predominantly from lipids as opposed to proteins[22]. This may suggest that the hypo-reflective regions are primarily tumor cell nests as opposed to sebaceous glands.

We have demonstrated a clinical system and probe for combined RS-OCT analysis of cancerous skin lesions, *in vivo*. The images and spectra reflect the wealth of additional information that available from both morphological and biochemical characterization of skin lesions with combined RS-OCT. It is clear, however, that the primary challenge now becomes interpreting the data sets, particularly in the context of a complex clinical problem such as skin cancer detection. The inherent variability in the structure of normal skin as a function of body location and gender are readily apparent in the OCT images. Obtaining meaningful information from these images will surely require extensive analysis of many lesions in order to generally understand the biological significance of hypo- or hyper- reflective structures and their morphological features. In addition, development and validation of a functional statistical classification algorithm to realize the full power of molecular analysis with spectroscopy will also require the collection of a large number of spectra. The analysis of these complimentary data sets is likely to improve the clinical utility of beyond that attainable through the use of both techniques independently. Added features to improve the clinical utility of the probe, including video imaging would benefit the clinical ease of implementation as well. Nevertheless, we have demonstrated the potential of combined RS-OCT for the diagnosis of skin cancers through the development of a clinical device capable of *in vivo* morphological and biochemical analysis.

Acknowledgements

The authors acknowledge Dr. Allison Hanlon for her clinical expertise and assistance in patient enrollment, Dr. Mark Mackanos and Dr. Xiaohong Bi for assistance in performing measurements, the Vanderbilt University Physics machine shop, and the Vanderbilt University Skin Disease Research Center (NIH 5P30 AR041943) for histopathology. This research was funded by NIH R21 CA133477 01/02

References

1. "Cancer Reference Information: Skin Cancer" (American Cancer Society, 2006), retrieved http://www.cancer.org/docroot/cri/cri_0.asp.
2. "Cancer Facts and Figures: 2009" (American Cancer Society, 2009), retrieved http://www.cancer.org/downloads/STT/500809web.pdf.
3. M. Rajadhyaksha, G. Menaker, T. Flotte, P. J. Dwyer, and S. Gonzalez, "Confocal examination of nonmelanoma cancers in thick skin excisions to potentially guide mohs micrographic surgery without frozen histopathology," J Invest Dermatol **117**(5), 1137-1143 (2001).
4. M. Mogensen, L. Thrane, T. M. Jorgensen, P. E. Andersen, and G. B. E. Jemec, "OCT imaging of skin cancer and other dermatological diseases," Journal of Biophotonics **2**(6-7), 442-451 (2009).
5. L. Brancaleon, A. J. Durkin, J. H. Tu, G. Menaker, J. D. Fallon, and N. Kollias, "In vivo fluorescence spectroscopy of nonmelanoma skin cancer," Photochemistry and Photobiology **73**(2), 178-183 (2001).
6. C. A. Lieber, S. K. Majumder, D. L. Ellis, D. D. Billheimer, and A. Mahadevan-Jansen, "In vivo nonmelanoma skin cancer diagnosis using Raman microspectroscopy," Lasers in Surgery and Medicine **40**(7), 461-467 (2008).
7. L. P. Hariri, A. R. Tumlinson, D. G. Besselsen, U. Utzinger, E. W. Gerner, and J. K. Barton, "Endoscopic optical coherence tomography and laser-induced fluorescence spectroscopy in a murine colon cancer model," Lasers Surg Med **38**(4), 305-313 (2006).
8. P. J. Caspers, G. W. Lucassen, and G. J. Puppels, "Combined in vivo confocal Raman spectroscopy and confocal microscopy of human skin," Biophys J **85**(1), 572-580 (2003).
9. T. Gambichler, A. Orlikov, R. Vasa, G. Moussa, K. Hoffmann, M. Stucker, P. Altmeyer, and F. G. Bechara, "In vivo optical coherence tomography of basal cell carcinoma," J Dermatol Sci **45**(3), 167-173 (2007).
10. T. Gambichler, P. Regeniter, F. G. Bechara, A. Orlikov, R. Vasa, G. Moussa, M. Stucker, P. Altmeyer, and K. Hoffmann, "Characterization of benign and malignant melanocytic skin lesions using optical coherence tomography in vivo," J Am Acad Dermatol **57**(4), 629-637 (2007).
11. M. Mogensen, T. M. Joergensen, B. M. Nurnberg, H. A. Morsy, J. B. Thomsen, L. Thrane, and G. B. Jemec, "Assessment of optical coherence tomography imaging in the diagnosis of non-melanoma skin cancer and benign lesions versus normal skin: observer-blinded evaluation by dermatologists and pathologists," Dermatol Surg **35**(6), 965-972 (2009).
12. N. Stone, C. Kendall, N. Shepherd, P. Crow, and H. Barr, "Near-infrared Raman spectroscopy for the classification of epithelial pre-cancers and cancers," Journal of Raman Spectroscopy **33**(7), 564-573 (2002).
13. S. Sigurdsson, P. A. Philipsen, L. K. Hansen, J. Larsen, M. Gniadecka, and H. C. Wulf, "Detection of skin cancer by classification of Raman spectra," IEEE Trans Biomed Eng **51**(10), 1784-1793 (2004).

14. C. A. Patil, N. Bosschaart, M. D. Keller, T. G. van Leeuwen, and A. Mahadevan-Jansen, "Combined Raman spectroscopy and optical coherence tomography device for tissue characterization," Optics Letters **33**(10), 1135-1137 (2008).
15. A. M. Rollins, M. D. Kulkarni, S. Yazdanfar, R. Ung-arunyawee, and J. A. Izatt, "In vivo video rate optical coherence tomography," Optics Express **3**(6), 219-229 (1998).
16. A. M. Rollins and J. A. Izatt, "Optimal interferometer designs for optical coherence tomography," Optics Letters **24**(21), 1484-1486 (1999).
17. C. A. Lieber and A. Mahadevan-Jansen, "Automated method for subtraction of fluorescence from biological Raman spectra," Applied Spectroscopy **57**(11), 1363-1367 (2003).
18. J. Welzel, "Optical coherence tomography in dermatology: a review," Skin Res Technol **7**(1), 1-9 (2001).
19. A. Nijssen, T. C. B. Schut, F. Heule, P. J. Caspers, D. P. Hayes, M. H. A. Neumann, and G. J. Puppels, "Discriminating basal cell carcinoma from its surrounding tissue by Raman spectroscopy," Journal of Investigative Dermatology **119**(1), 64-69 (2002).
20. P. J. Caspers, G. W. Lucassen, R. Wolthuis, H. A. Bruining, and G. J. Puppels, "In vitro and in vivo Raman spectroscopy of human skin," Biospectroscopy **4**(5 Suppl), S31-39 (1998).
21. A. J. Singer, Z. Wang, S. A. McClain, and Y. Pan, "Optical Coherence Tomography: A Noninvasive Method to Assess Wound Reepithelialization," Academic Emergency Medicine **14**(5), 387-391 (2007).
22. A. Mahadevan-Jansen and R. Richards-Kortum, "Raman Spectrscopy for the Detection of Cancers and Precancers," Journal of Biomedical Optics **1**(1), 31-70 (1996).

CHAPTER VI

CONCLUSIONS

Summary

The goal of this dissertation was to develop the technique of combined Raman spectroscopy – Optical Coherence Tomography (RS-OCT) and construct a clinical system for the *in vivo* measurement of questionable skin lesions. Previous work in the field of Raman Spectroscopy (RS) for skin cancer diagnosis[1, 2] had identified the potential benefit of combined high-resolution imaging with RS. In addition questions had arisen as to the necessity of a confocal collection geometry to accurately classify skin cancers *in vivo*.

In order to address the necessity of confocal collection for *in vivo* classification of skin cancers with RS, the first aim of this work was to perform a pilot study to assess the ability of fiber optic probe based RS to classify skin cancers *in vivo*. Spectra of 34 lesions from cancerous and non-cancerous tissue, along with matched spectra from similar normal skin, were measured with fiber optic probe based RS. Difference (lesion – matched normal) spectra were calculated to account for inherent variations in the skin. Difference spectra were classified using Sparse Multinomial Logistic Regression (SMLR). Spectra were classified with an overall accuracy of 85%. The sensitivity and specificity were 78% and 94% respectively. These results suggest the potential utility of non-confocal RS for accurate classification of skin cancers, however a more extensive research is necessary.

The second aim of this dissertation was to develop a benchtop combined RS-OCT system utilizing separate OCT and Raman system backbones. A dual-modal device capable of sequential acquisition of Raman Spectroscopy (RS) and optical coherence tomography (OCT) along a common optical axis was constructed. The system performance was characterized, and capability of the device to identify structurally ambiguous features within an OCT image with RS in a scattering phantom, guide acquisition of RS from a localized malignancy in *ex vivo* breast tissue, and perform *in*

vivo tissue analysis of a scab. The device enhances application of both RS and OCT by precisely guiding RS acquisition with OCT images while also compensating for the lack of molecular specificity in OCT with the biochemical specificity of RS. The results indicate the potential capability of RS-OCT for *in-vivo* morphological and biochemical analysis of the skin. This work was published in Optics Letters in 2008.

The third aim of this dissertation was to develop a benchtop combined RS-OCT using a common detection arm. Previous implementations of RS-OCT have employed separate system backbones for OCT and RS. Here, we present the design and application of a common detector combined RS-OCT instrument for evaluating the morphological and biochemical differences in tissue. The instrument is applied to evaluating a rat model for oxygen induced retinopathy. Rat pups that have undergone a variable oxygen treatment are compared to rats raised in room air. Images and spectra collected at an age of 26 days postnatal demonstrate differences in the thickness of the inner and outer nuclear layers, with OCT as well differences in the Raman spectral bands attributed to DNA and RNA nucleotides, amino acids, and proteins. The results from this study demonstrate the first implementation of common detector RS-OCT, however they suggest that the independent detection of the RS and OCT signals is the optimal approach for *in vivo* analysis of skin lesions.

The final aim of this dissertation is to develop a clinical system for combined RS-OCT for analysis of the morphological and biochemical features of skin cancer. The portable instrument utilizes independent RS and OCT system backbones, and is integrated in a common clinical probe. The potential of the probe for cancer the detection of the morphological and biochemical features of malignant and non-malignant lesions is demonstrated. The results from this aim indicate the potential of RS-OCT for evaluating skin cancers, and warrant more extensive work.

Future Directions

The work done is this dissertation has demonstrated the feasibility of combined RS-OCT in a clinical setting, and has laid the basic foundation for performing a full assessment of the performance of RS-OCT for skin cancer screening, diagnosis, and

staging. In order to make a proper assessment of this approach, however, more clinical work is necessary.

Raman spectroscopy for skin cancer diagnosis

The fiber-optic probe based clinical study should continue, and more patients ought to be enrolled. Although the classification performance achieved in the fiber optic probe study did not match that of previous *in vivo* confocal studies, the result can easily be attribute to sample size limitations. Previous *in vivo* work consisted of a study which enrolled just 21 patients, in comparison to the 34 used for the fiber probe study. Neither of these studies is sufficiently powered to draw any real conclusions as to the superiority of one technique over another. The best course of action for accurately determining the relative performance of the two collection geometries is to conduct side-by-side analysis of fiber-probe based RS with confocal RS on the same lesions, with the probes both placed over identical spots within the lesion. Obviously, the appropriate sample size estimation needs to be made based on the study design and statistical classification algorithm pursued. Ultimately, this number will likely be quite large, because simple two-class differentiation of cancer from normal is only the intermediate goal. The biochemical specificity of Raman suggests, and has been demonstrated capable of, direct multi-class differentiation of skin cancers[3]. The long term goal of RS in the skin should be directed towards multi-class differentiation of normal skin, the set of benign skin lesions that commonly mistaken for skin cancer, BCC, SCC, and melanoma.

Subsequent to the development of SMLR, a few alternative statistical pattern recognition and machine learning algorithms have been proposed for classification of Raman spectra. These include the combination of maximum representation and discrimination feature in combination with SMLR (MRDF-SMLR)[4] and Generalized Linear Models (glmnet)[5]. MRDF-SMLR performs a set of arbitrary non-linear operations on the input data to tease out higher order correlations in the data prior to applying SMLR machine learning for classification, however development of this algorithm requires a set of subjective, non-optimizable decisions be made as to the initial non-linear operations. This results in the generation of classification frameworks that are difficult to reproduce. In addition, the nature of the algorithm make it impossible to determine which spectral features are being relied upon for classification, which detracts from the potential

advantage of RS for specific biochemical characterization of the features of pathology. The machine learning framework of glmnet is currently being evaluated by our group in collaboration with the Vanderbilt Biostatistics department. The advantages of glmnet include a superior set of machine learning heuristics that promote easier generalization of the model and are less susceptible to over-learning the training data. Pursuing the appropriate application of these methods will be critical to realizing the full diagnostic potential of RS.

Despite the fact that no clear statistical determination can be made as to the performance of the fiber optic probe for skin cancer classification, there are two reasons that suggest switching to a different probe design may be appropriate. Considering the fact that skin cancers present primarily in the dermis, a non beam-steered approach may be advantageous to biasing the collection more towards the underlying tissues and less towards the epidermis. The second, more pragmatic reason, is that the beam-steered probe used in this study is a proprietary technology from the now-defunct Visonex, Inc. , no longer available. Further effort to demonstrate the capability of this probe would serve limited practical purpose. A more suitable probe would simply have flat-polished collection fiber surrounding the illumination fiber. The collection geometry of such a probe would be less biased to surface tissues and have greater contributions from underlying regions.

Combined RS-OCT

Aims #2 and #3 of this dissertation provided proof-of-principle demonstrations of the feasibility of RS-OCT with independent and common detection arms. Broadly, this work demonstrated the ability of RS-OCT to perform both morphological and biochemical analysis of tissues in the breast and retina (*ex vivo),* and the skin (*in vivo).* The advantage of the approach is that it overcomes the direct limitations of the lack of biochemical sensitivity in OCT and the lack of morphological information in RS.

From the instrumentation perspective, the integration of RS and OCT is a challenge. The laser source requirements for the two systems are opposite; RS requires a narrow band, wavelength stabilized laser while OCT requires either a broadband source or a rapidly swept narrow band source. The relative intensity of elastic scattering (the

source of signal in OCT) vs. in-elastic scattering (the source of contrast in RS) affects both the source and detection parameters of both systems. In order to detect high quality signal from tissues, RS requires both a fairly high power at the sample (minimum 20 mW) and extremely sensitive detection electronics, while OCT can make due with much lower powers (μW in the cast of SD-OCT) and less sensitive detection electronics. In this context, there is no middle ground for integration of either source or detection hardware. That suitable for RS must be utilized at the expense of OCT. Regardless, CCD detector technology continues to improve, and it is entirely possible that with redesign of the detectors to increase the potential speed (wider bandwidth internal electronic amplification schemes and the use of a frame transfer array), an common detector RS-OCT similar to that demonstrated in aim #3 could be constructed with real-time (> 32 frames/sec) imaging speeds. The issue of improving the OCT sensitivity would be slightly more challenging. In OCT, optimal sensitivity is achieved with an interferometer splitting ratio of 50:50. Alternative ratios can be used, but they come at the expense of optical heterodyne gain. From here, increasing the power to the sample improves the signal to noise. This necessitates detecting an increased DC reference signal, which will eventually lead to camera saturation. Thus the camera saturation level is directly related to the optimal sensitivity achievable in OCT. The full well capacity of shift register limits the maximum signal that could illuminate a CCD array before saturation, and is typically a function of the physical size of the array elements. Thus, in order to increase the sensitivity of OCT, the pixel heights would have to be increased. In contrast to designing custom electronics to pair with a CCD chip to improve imaging speed, obtaining CCD chips with custom architectures and pixel sizes is exceedingly difficult. However, if such a chip could be obtained, it would be better suited for RS-OCT with a common detector arm.

A third approach to combined RS-OCT would be to attempt to integrate the source and detection arms of the system. An alternative approach to dispersing the detected OCT light with a spectrometer to detect the spectral interference is to perform swept-source OCT (SS-OCT). In SS-OCT, a narrow band laser is rapidly swept across a broad spectral band. The interference signal is then detected with a photodiode triggered to the scanning of the source to achieve detection of interference as a function of k. Since

the Raman spectrum of a sample is typically independent of the excitation wavelength, a similar approach could theoretically be used to build up a Raman spectrum. Such an approach would require three hardware features; 1.) The combination of laser power and detection sensitivity necessary to detect the weakly scattered Raman light. This may be possible with high gain avalanche photodiodes (APD) and swept lasers with narrow-band peak powers on the order of 20 mW in the near-infrared (i.e. 785 nm), 2.) A narrow-band tunable filter in the Raman detection path synched to the laser sweep, and 3.) A laser sweep range that generated a Raman spectrum that corresponded to the fingerprint region. This approach would surely be a technical challenge, and would require seeking out industrial collaboration with those in the tunable filter and swept-source sectors. Creating a tunable filter can rapidly scan, and also be locked with the mode stability necessary for RS is a fundamental technical challenge that would have to be met. In addition, although it is theoretically feasibly, it is unknown whether high gain APD's have the sensitivity necessary to detect Raman scattered light.

Approaching the challenge of combining RS and OCT from the instrumentation perspective is certainly intriguing; however the utility of RS and OCT together is derived from their strengths operating at their potential. If the technical arrangement compromises either modalities performance, the utility of the combined device is diminished. More importantly, the target application's needs should be considered paramount when designing any instrument. In this context, the excitation wavelength selection for both modalities is critical. Both Raman and OCT use some form of scattering for their signal source. Scattering intensity is known to fall of as a function of λ^{-4}. In OCT, this can be advantageous, because imaging depth is not limited by instrumentation sensitivity, but by the physical penetration depth of light in tissue. Thus, a decrease in scattering can result in an increased penetration depth in the near-infrared (< 2.0 μm). In RS, on the other hand, decreasing scattering intensity results in the reduction of an already weak signal. The potential benefit, however, is that tissue autofluorescence falls off significantly in the near-infrared, particular past 1.0 μm. The downside is that detection electronics in that band have not yet demonstrated the sensitivity necessary to perform high quality RS at that wavelength range.

Ultimately, these factors drove the demonstration of common detector RS-OCT away from the skin and towards the retina. OCT imaging performance in the skin at 850 nm is simply insufficient for visualizing the morphological extent of subsurface lesions. In addition, hardware limitations prevented image acquisition in a clinically relevant timeframe.

Potential Applications of RS-OCT

Based upon existing work demonstrating the potential strengths and limitations of RS[6] and OCT[7] in characterizing breast tissue, The RS-OCT approach could be beneficial for both evaluating tumor resection margins *in vivo* for the presence of residual tumor cells, as well as for evaluating removed breast tumor samples for clear margins *ex vivo*. Such work could be performed with systems similar that described in aim #2 (for *ex vivo* analysis) and aim #4 (for *in vivo* analysis).

In addition to the breast, another possible location for clinical application of RS-OCT is the gastrointestinal tract. Both OCT[8] and RS[9] have been demonstrated in these tissues with promising results, but similar limitations to those previously mentioned. The primary challenge of combined RS-OCT in the GI tract would be probe design. The fiber optic cables that carry OCT signal are typically single-mode fiber with core diameters on the order of 9 μm or less. Raman spectroscopy, on the other hand, requires multi-mode fiber optics with core diameters on the order of 100's of μm's, which makes illumination and collection with the same fiber optics impossible. A straightforward approach, however, would be to use individual RS and OCT fiber probes with a precision designed tip that allowed for co-registration of the data sets. The GI tract is extremely heterogenous in nature – even more so than the skin – with a number of benign and malignant lesions. Similar to the skin, these spectral signatures would have to be recorded and classification algorithms would need developed to realize the full potential of a combined approach.

Combined RS-OCT for directing skin cancer therapy

The primary motivation for combining RS and OCT was to create a versatile clinical instrument that is capable of meeting all the needs for disease detection and the direction of treatment. This includes screening, diagnosis, and staging of disease. RS-

OCT has the ability to perform all of these tasks, and the work shown in aim #4 provides an initial clinical demonstration of the instrument's potential. In order to further demonstrate the utility of the technique, a small pilot study should be conducted to demonstrate the instruments ability to screen large areas, diagnose disease with high accuracy, and identify tumor margins for direction of treatment. This could all be accomplished with a small pilot study that enrolled approximately 15 patients with BCC. Further studies could demonstrate the devices ability in a wider range of disease classes and larger sample size study.

The limitations of the current clinical system, however, warrant the development of a 2nd generation system, which is already underway. The current state-of-the-art OCT imaging systems at 1310 nm using spectral domain detection are capable of acquiring images at > 50 of frames/sec at resolutions of < 10 μm. We have acquired a line scan camera that is capable of scanning 46x faster than the current system, and a laser source with 1/3 broader bandwidth in order to fabricate such an OCT system backbone. The ideal approach for RS-OCT the context of skin cancer detection remains to use separate system backbones so as not to compromise the performance of either system individually.

The mechanical arm mounting and support interface could also use improvement. Movement in the joints of the arm is due to tension springs, which require a minimum of 17 lbs of load at the end to keep the arm from rising up to the ceiling. This problem was overcome by incorporating an extension rod to the end of the arm to increase the moment arm, and also by constructing the probe out of heavy ½" stainless steel instead of ¼" aluminum. In addition, the mechanics of the arm at each joint provide only one degree of freedom. Although the probe can be positioned in any orientation, it often requires a great deal of maneuvering to position the probe joints appropriately. Improving the arm to employ ball and socket joints with variable amounts of tightness would likely be a better approach.

The probe interface could also be improved. Aligning the probe with the lesion to be measured is difficult, because once the probe is in place, the user cannot visually see the lesion, they must rely on the OCT image for guidance. Ideally, the user would be able to localize the OCT with a visual image, and the RS with the OCT. A second generation

probe should be constructed in order to allow incorporate a miniature CCD to visual orientation.

Beyond these basic improvements, rethinking the physical approach to collecting the Raman signal is also warranted. Despite the fact that it is possible to collect RS through this configuration, realizing an acquisition time less than 30 seconds would enhance the clinical utility of the device. The approach that would minimize the collection time the most significantly would be to perform RS with a contact fiber probe. The probe could be designed such that the Raman fiber probe would be located out of the optical path of the OCT and video imaging. A user controlled mechanical mechanism would lower the fibers into place on the lesion. The position of the probe with respect to the imaging frame would have to be carefully calibrated, but is possible. Such an approach, in combination with the 2nd generation OCT system backbone, would greatly improve the speed of the instrument.

Furthermore, a bringing collection fibers in contact with the lesion would open the possibility collecting from various source-detector offsets and performing Spatially Offset RS (SORS)[10]. The basic concept of SORS is that light detector with larger spatial offsets originates from deeper levels of the tissue. The specifics are based on the optical properties of the tissue modulating the transport of Raman scattered light. The potential of utilizing a SORS detection scheme is that it allows simultaneous collection of Raman scattered light from multiple depths. The disadvantage is that it has nowhere near the spatial resolution of confocal RS. The depths probed by the various spatial offsets are a function of tissue optical properties, while the achievable spatial resolution is determined by a combination of tissue optical properties and the incremental differences in spatial offset that the fibers can be set at. The SORS approach was previously only demonstrated in detecting calcified tissues under soft tissues, however recent work demonstrated the potential of the technique for differentiating layers of soft tissue as well[11]. If contact fibers were used to collect the Raman scattered light in a future RS-OCT clinical probe, segmenting the fibers for SORS analysis could provide useful information on tissue composition as a function of depth.

Significance

The tabletop demonstration of combined RS-OCT represented the first work reporting the feasibility of a dual-modal device that combined spontaneous RS with OCT. Furthermore, it was the first demonstration that such a technique has utility for the analysis of malignant breast tissues and in the skin. The skin images and spectra served as the first demonstration of the feasibility of RS-OCT analysis *in vivo*. Overall the manuscript provided the initial identification and demonstration of the potential advantages of RS-OCT.

The common detector RS-OCT manuscript will signify the first demonstration of RS and OCT with a common detector. The application to the retina represented the first demonstration of RS of the retina through an intact eye. Despite the fact that the power delivered to the retina is far in excess of safe exposure standards in the human, the differences between the pathological and normal tissues indicate that should an alternative method for acquiring Raman signal from the retina allow for safe exposure, valuable data could be obtained. The implications of the common detector instrument include studies of the morphological and biochemical progression of pathology in animal models of retinal disease.

The clinical instrument for performing RS-OCT of skin cancers was, however, the primary end product this dissertation sought out. It is the first demonstration of a dual modal optical tool designed to meet the current clinical challenges associated with the direction of skin cancer treatment – screening, diagnosis, and staging. This is in contrast many previous studies, which were reported by those who simply sought to report the utility of a specific optical instrument's application to a wide variety of clinical problems, of which skin cancer was only one. These reports often took shape similar to the 3rd manuscript, common detector RS-OCT and it's application to the retina. They were demonstrations of novel instruments that sought an appropriate application. The well motivated selection of specific optical techniques for dual- and multi- modal devices is becoming a more widely embodied approach to solving specific clinical problems amongst those in the biomedical optics community. This shift in mindset certainly would not be possible without the wealth of literature describing the application of novel optical techniques to a slew of clinical problems. It is important that the biomedical optics

community continues to receive contributions from both types of researchers; those with hammers running around looking for nails to hit, and those devoted to single problem, collecting the best tools to handle it. This dissertation represents a little bit of both approaches. While there was significant energy expended on steadily addressing the clinical challenges associated with skin cancer, there were also many months spent overcoming the obstacles associated with developing a novel instrument and identifying an appropriate application.

References

1. C. A. Lieber, S. K. Majumder, D. Billheimer, D. L. Ellis, and A. Mahadevan-Jansen, "Raman microspectroscopy for skin cancer detection in vitro," J Biomed Opt **13**(2), 024013 (2008).
2. C. A. Lieber, S. K. Majumder, D. L. Ellis, D. D. Billheimer, and A. Mahadevan-Jansen, "In vivo nonmelanoma skin cancer diagnosis using Raman microspectroscopy," Lasers in Surgery and Medicine **40**(7), 461-467 (2008).
3. S. Sigurdsson, P. A. Philipsen, L. K. Hansen, J. Larsen, M. Gniadecka, and H. C. Wulf, "Detection of skin cancer by classification of Raman spectra," IEEE Trans Biomed Eng **51**(10), 1784-1793 (2004).
4. S. K. Majumder, M. D. Keller, M. C. Kelley, F. I. Boulos, and A. Mahadevan-Jansen, "Comparison of autofluorescence, diffuse reflectance, and Raman spectroscopy for breast tissue discrimination," Journal of Biomedical Optics (in press)(2008).
5. J. Friedman, T. Hastie, H. Hofling, and R. Tibshirani, "Pathwise Coordinate Optimization," Annals of Applied Statistics **1**(2), 302-332 (2007).
6. A. S. Haka, K. E. Shafer-Peltier, M. Fitzmaurice, J. Crowe, R. R. Dasari, and M. S. Feld, "Diagnosing breast cancer by using Raman spectroscopy," Proc Natl Acad Sci U S A **102**(35), 12371-12376 (2005).
7. S. A. Boppart, W. Luo, D. L. Marks, and K. W. Singletary, "Optical coherence tomography: feasibility for basic research and image-guided surgery of breast cancer," Breast Cancer Res Treat **84**(2), 85-97 (2004).
8. M. V. Sivak, K. Kobayashi, J. A. Izatt, A. M. Rollins, R. Ung-runyawee, A. Chak, R. C. K. Wong, G. A. Isenberg, and J. Willis, "High-resolution endoscopic imaging of the GI tract using optical coherence tomography," Gastrointestinal Endoscopy **51**(4), 474-479 (2000).
9. M. G. Shim, L. M. Song, N. E. Marcon, and B. C. Wilson, "In vivo near-infrared Raman spectroscopy: demonstration of feasibility during clinical gastrointestinal endoscopy," Photochem Photobiol **72**(1), 146-150 (2000).
10. P. Matousek, I. P. Clark, E. R. Draper, M. D. Morris, A. E. Goodship, N. Everall, M. Towrie, W. F. Finney, and A. W. Parker, "Subsurface probing in diffusely scattering media using spatially offset Raman spectroscopy," Appl Spectrosc **59**(4), 393-400 (2005).
11. M. D. Keller, S. K. Majumder, and A. Mahadevan-Jansen, "Spatially offset Raman spectroscopy of layered soft tissues," Opt Lett **34**(7), 926-928 (2009).

APPENDIX

The protocol under which the *in vivo* combined Raman Spectroscopy – Optical Coherence Tomography (RS-OCT) data collected in this dissertation was approved by the Vanderbilt University and Veteran's Affairs Tennessee Valley HealthCare System Institutional Review Boards (IRB's). IRB approval of protocols ensures ethical experimental design and patient safety in human experiments. For proof-of-principle and pilot studies that are only designed to evaluate the feasibility of novel instruments, it is the responsibility of protocol authors to ensure the safe operation of the devices and report any adverse affects to the IRB. Ultimately, the widespread clinical application of instruments employing Raman spectroscopy (RS) for skin cancer diagnosis will require review and approval by the Food and Drug Administration (FDA) for safety and efficacy. With respect to laser safety, the primary guidelines considered by the FDA are taken from a report published by the American National Standards Institutes (ANSI) for the safe use of lasers[1]. This report details the maximum permissible exposure (MPE) levels for skin, which are defined fairly arbitrarily as 10% of the laser exposure that results in the earliest sign of histological laser damage in 50% of samples. For the most part, these exposure levels were determined in the late 1960's and early 1970's, with narrowly defined models and then extrapolated to cover a wide-range of wavelengths and illumination geometries. In addition, the levels were determined prior to the development of modern methods in cellular and molecular biology that probe more sensitive indicators of cellular stress, damage, and viability. Most importantly, the application of laser-based techniques for detection of potentially lethal diseases such as cancer warrants

consideration of the potential benefits *as well as* the risks, similar to the risk/benefit assessments typically conducted for novel pharmaceuticals. The lack of context and conservative nature of the MPE's is acknowledged within the FDA, and there exists some desire to refine the MPE's accordingly. As the application of RS for skin cancer diagnostics moves forward, however, a large part of the responsibility for demonstrating the relative safety of RS for the non-invasive diagnosis of disease will be placed on the shoulders of those within the RS community itself.

The photobiological effects of laser irradiation that can result in tissue damage can be separated into three mechanistic categories, 1) photomechanical, 2) photothermal, and 3)photochemical. Photomechanical effects are the result of rapid heating and expansion of the tissue by pulsed laser sources. The expansion of the tissue produces a pressure wave that can disrupt the physical organization of the tissue and result in tissue ablation. The pulse durations that typically produce photomechanical effects are typically on the order of 10^{-6} seconds or less, and thus are not a concern for the exposure durations used in RS. Photochemical effects result from the activation of chemical reactions (i.e. oxidative processes) originating from the absorption of light by specific molecules. Absorption by molecules intrinsic to the skin is not known to result in any photochemical reactions that result in tissue damage. Photothermal mechanisms are the most likely sources of tissue damage induced by RS. On the molecular and cellular level, the temperatures at which the denaturation of proteins, hylanization of collagen, de-activation of enzymes, cell shrinkage, membrane rupture, and cell death have previously been reported[2]. Measurement of the skin surface temperatures during RS can therefore act as a surrogate marker for the effect of the Raman laser beam on the skin.

This appendix will describe preliminary experiments designed to evaluate the effect that Raman laser exposure levels of combined RS-OCT have on skin by measuring the surface temperature of the skin during RS measurement with a thermal camera. The results suggest that these effects are minimal, despite the fact that the exposure levels used are well in excess of those defined by the ANSI standards.

Materials and Methods

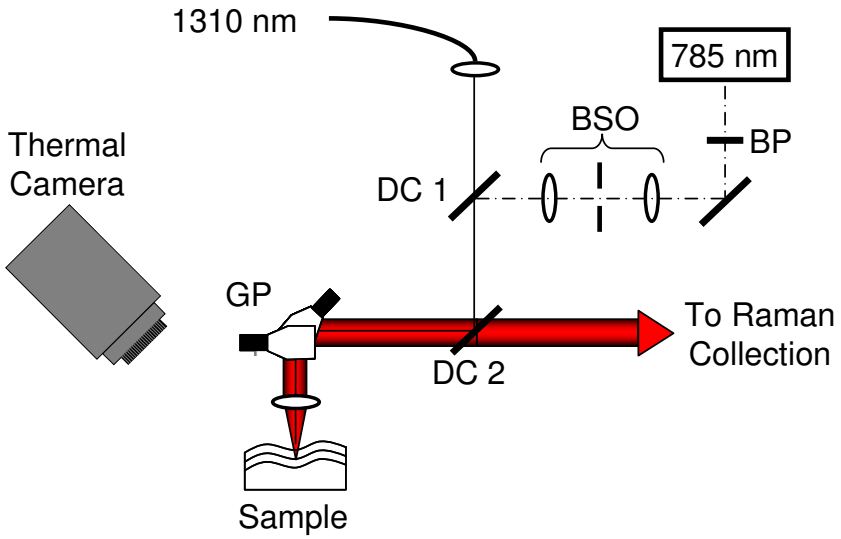

Fig. A.1. Sample arm of the benchtop combined RS-OCT. The Raman illumination is a 785 nm source, and the OCT illumination is a 1310 nm source. BP – 785 nm band pass filter, BSO – beam shaping optics, DC1 – dichroic mirror 1, DC2 – dichroic mirror 2, GP – galvanometer pair. Thermal imaging is performed by the thermal camera.

The experimental setup is shown in figure A.1. Raman illumination and detection are identical to the combined RS-OCT system described in chapter 3[3]. A 785 nm external cavity diode laser (Sacher GmBH) is focused at the sample to a 75 µm spot with a confocal parameter of 770 µm. The power at the sample is 40 mW. During RS-OCT measurements, the sample is additionally illuminated by a 1310 nm source with 7 mW of power at the sample. The typical exposure time necessary to acquire Raman spectra is 30

seconds. Measurements of the skin surface temperature were made with a thermal camera (FLIR systems) for a duration beyond the RS acquisition time, beginning just prior to illumination. Both beams were blocked prior to the initiation of Raman spectral acquisition and temperature measurements. In order to localize the area where the RS-OCT probe beam irradiated the tissue, a region of interest (ROI) within the image corresponding to the position of the Raman illumination beam was identified (fig A.2), and the maximum temperature within this area was tracked as a function of time.

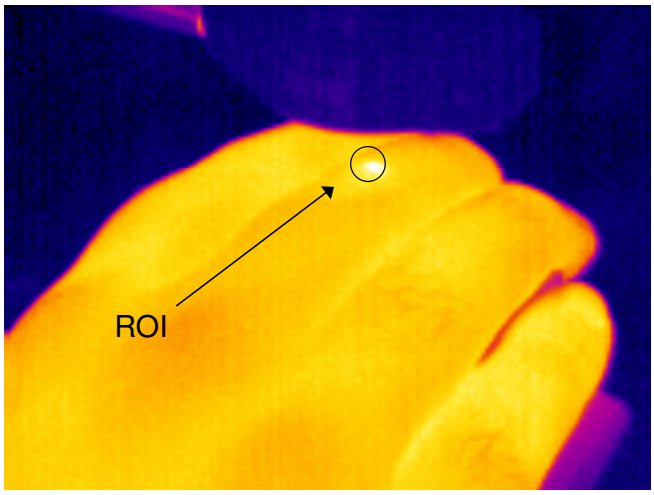

Fig. A.2. Example Thermal Camera Image and Region of Interest (ROI) Positioning.

In order to assess the effect of a typical the Raman illumination beam, surface temperature traces were recorded over the course of three illumination trials. Measurements were made over a duration of 60 seconds with the Raman probe beam at 40 mW and the OCT probe beam at 7 mW on the back of the hand A second, slightly different measurement was performed near the nail-bed on the back of the finger with the Raman probe beam power increased to 50 mW and the temperature measurement duration extended to 2 minutes.

Results

The skin surface temperature traces for the first experiment are shown in figure A.3. The skin surface temperature was varied at the beginning of the trails between 35˚ and 36˚ C, and rapidly increased approximately 3˚ C in the first 20 seconds. The second and third trials show the skin surface temperature stabilizing after the initial 20 second period.

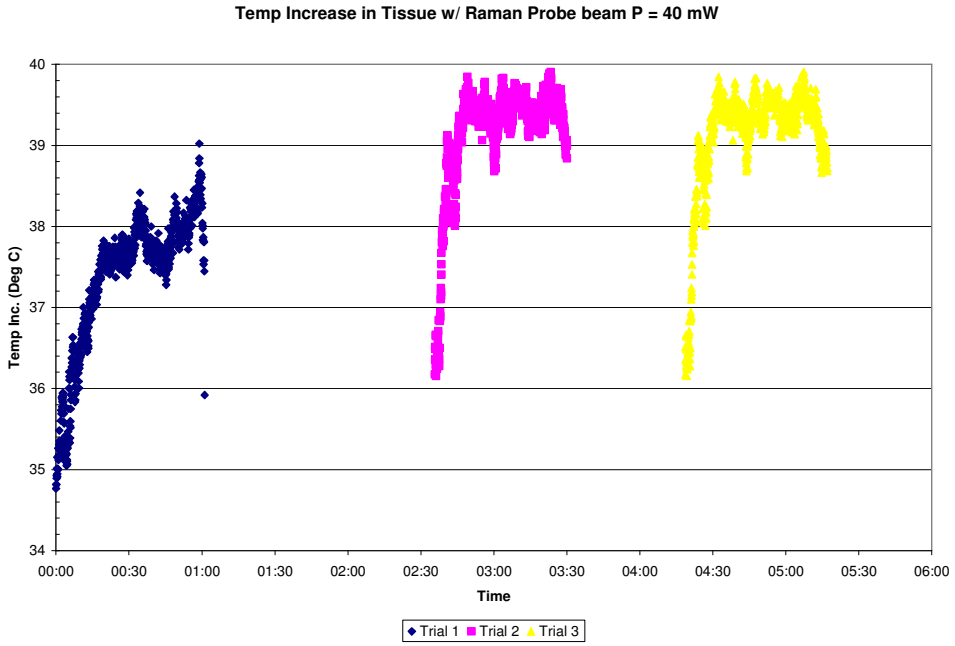

Fig. A.3. Temperature Traces for P_{Raman} = 40 mW, P_{OCT}= 7mW illumination on the back of the hand.

Figure A.4 depicts the temperature trace of the second experiment, a single trial conducted at the nail bed over a duration of 2 minutes with the Raman laser power increased to 50 mW. Again, there was a rapid initial increase (12˚ C) lasting the initial 45 seconds, after which the temperature seemed to stabilize at 42˚ C.

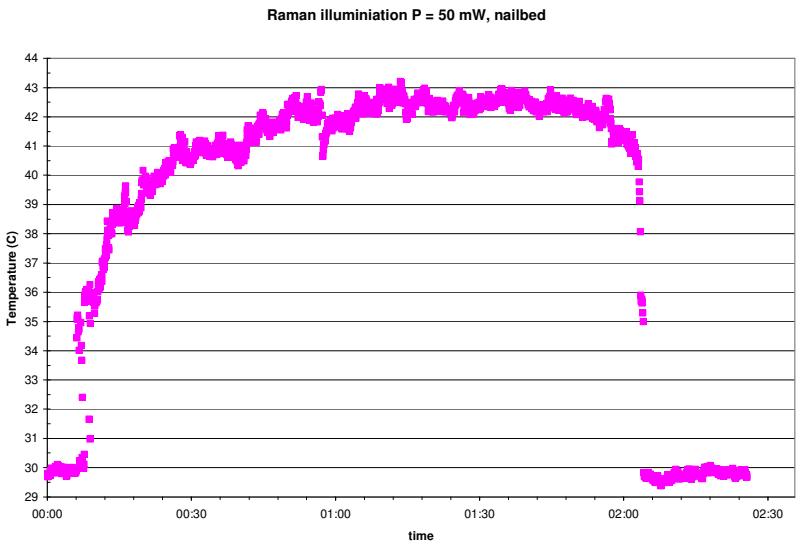

Fig. A.4. Temperature Traces for P_{Raman} = 50 mW, P_{OCT}= 7mW illumination on the nail bed.

Discussion

Taken together, figures A.2 and A.3 indicate that the laser exposure levels used in RS-OCT result in a moderate increase of 3˚ C to 12˚ C in temperature that stabilizes after some time. These steady-state temperatures range from 39.5˚ C to 43˚ C. Previous studies evaluating the effects of photothermal effects of laser irradiation on tissue are summarized in figure A.5[2, 4]. Over the time course of typical Raman Measurements, a cell temperature in excess of 52˚ C has been reported necessary to result in cell death. The regime current Raman measurements operate within is shown here to be at most 43˚ C, which is much lower. The implication is that current laser exposure parameters for RS do not result in irreversible cellular damage or cell death.

The question of whether or not these laser irradiation parameters affect the skin, however is still not answered by these preliminary experiments. Reversible damage to the tissue, such as minor burning and localized inflammation, fills the space between no

effect and irreversible damage. It is quite likely that the photothermal effects of RS on the skin include initiation of the cellular mechanisms involved in the response to thermal injury, such as the up regulation of heat shock protein 70[4]. Measures such as these would indicate the severity of reversible cellular stresses, which vary in their severity. Evaluating both the short term and long term impact of these stresses in the context of the benefits of non-invasive diagnosis of skin cancer on tissue is critical to determining safe laser exposure levels.

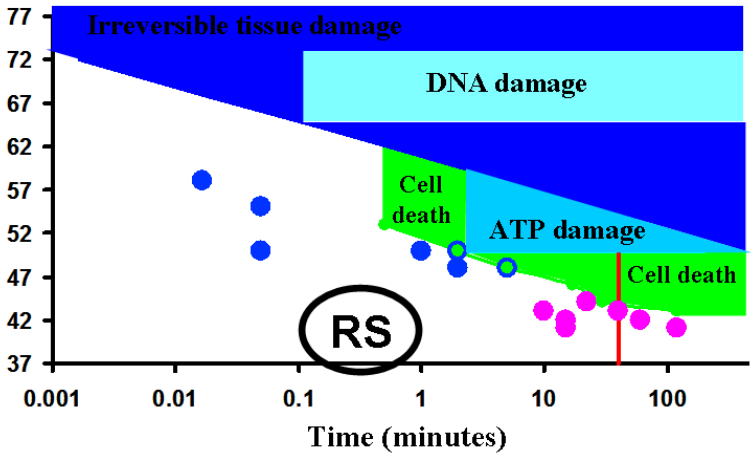

Fig. A.5. Photothermal effects of Raman Spectroscopy (RS) in the context of previous reports of laser irradiation of cells. Dots represent maximum heat-shock protein 70 expression[4].

The ANSI defined MPE's were not framed in the context of laser induced temperature increases or the relative benefit of disease diagnosis, but in the context of a fraction of the levels necessary for acute laser damage. In order to calculate the ANSI defined MPE for continuous wave laser exposure of the skin, section 8.4 of ANSI Standards for Safe Use of Lasers[1] was referenced. Calculations of the MPE for the three instrument configurations developed in the Vanderbilt University Biomedical Optics lab

the actual exposures used are shown in table A.1, along with the degree to which the exposure levels used exceed the ANSI limits.

Table A.1: Laser Exposure for Raman Spectroscopy Devices

	Exposure (J/cm^2)	MPE (J/cm^2)	Fold above MPE (x)
Fiber-Optic Raman Probe[5]	191	2.14	90
Handheld Confocal Raman Microscope[6]	$7.5 \cdot 10^6$	0.36	$21 \cdot 10^6$
Benchtop Combined RS-OCT[3]	31,000	0.296	105,000

The fiber-optic Raman probe used in a majority of the work characterizing the cervix and cervical dysplasia[5], along with the cancerous skin lesions in chapter II, utilizes a 785 nm source with a 400 μm illumination fiber. The laser power at the sample was 80 mW and is placed directly in contact with the skin for 3 seconds during acquisition. The handheld confocal Raman microscope[7] used for the *in vivo* pilot study used an 830 nm source focused to a 1.2 μm spot. The laser power at the sample was 40 mW, and the spectral acquisition time was 30 seconds. The benchtop combined RS-OCT instrument utilizes a 785 nm source for RS focused to a 35 μm spot. The corresponding laser exposures for all these instruments are well in excess of the ANSI MPE's. For the combined RS-OCT insturment, the exposure levels are more than 100,000 times that of ANSI MPE. Despite what appears to be alarming high levels of laser exposure with all the instruments, none of the volunteers whose skin or skin lesions were characterized reported any pain associated with RS. Here, we have additionally demonstrated that the exposure levels used in RS-OCT do not even result in the necessary temperature levels to induce irreversible tissue damage.

Conclusion

These preliminary experiments serve as a starting point for future work to identify the effect of the laser exposure parameters used for RS. The results indicate that the exposure levels used in this study result in skin surface temperatures below the threshold for irreversible cell damage, despite the fact that they greatly exceed the ANSI limits. In order to define reasonable exposure levels that are well placed in the context of patient safety/discomfort and the potential benefit non-invasive diagnosis of disease may provide, more work is certainly necessary. This work should include the rigorous evaluation of a wider range of laser exposure parameters including alternative illumination geometries such as those used in the fiber-optic probe or confocal RS. Analysis of the impact on tissue should be performed at both the cellular and tissue levels. Direct measures of cellular modulation, such as the up regulation of proteins associated with the healing response to thermal injury, should be assessed. Tissue level damage should be evaluated by a pathologist trained in discerning the features of laser damage. Such work would be well suited to direct the appropriate laser exposure levels for RS.

1. "American National Standard for Safe Use of Lasers," ANSI Z136.1 (American National Standards Institutes, 2000).
2. S. Thomsen, "Pathologic analysis of photothermal and photomechanical effects of laser-tissue interactions," Photochem Photobiol **53**(6), 825-835 (1991).
3. C. A. Patil, N. Bosschaart, M. D. Keller, T. G. van Leeuwen, and A. Mahadevan-Jansen, "Combined Raman spectroscopy and optical coherence tomography device for tissue characterization," Optics Letters **33**(10), 1135-1137 (2008).
4. G. J. Wilmink, T. Carter, J. M. Davidson, and E. D. Jansen, "Laser thermal preconditioning enhances dermal wound repair," presented at the Photonic Therapeutics and Diagnostics IV, 2008.

5. A. Mahadevan-Jansen, M. F. Mitchell, N. Ramanujam, U. Utzinger, and R. Richards-Kortum, "Development of a fiber optic probe to measure NIR Raman spectra of cervical tissue in vivo," Photochem Photobiol **68**(3), 427-431 (1998).
6. C. A. Lieber, S. K. Majumder, D. L. Ellis, D. D. Billheimer, and A. Mahadevan-Jansen, "In vivo nonmelanoma skin cancer diagnosis using Raman microspectroscopy," Lasers in Surgery and Medicine **40**(7), 461-467 (2008).
7. C. A. Lieber and A. Mahadevan-Jansen, "Development of a handheld Raman microspectrometer for clinical dermatologic applications," Optics Express **15**(19), 11874-11882 (2007).